M 2023

U.PORTO
FEUP FACULDADE DE ENGENHARIA
UNIVERSIDADE DO PORTO

PHOTO-THERMOCATALYTIC HYDROGENATION OF CO_2 INTO METHANE DRIVEN BY SUNLIGHT

RUI DANIEL GONÇALVES MATIAS

MASTER THESIS IN CHEMICAL ENGINEERING
PRESENTED TO THE FACULTY OF ENGINEERING
OF THE UNIVERSITY OF PORTO

Master in Chemical Engineering

Photo-thermocatalytic hydrogenation of CO_2 into methane driven by sunlight

Master dissertation

of

Rui Daniel Gonçalves Matias

Developed within the course of dissertation

held in

LSRE – LCM – Laboratory of Separation and Reaction Engineering – Laboratory of Catalysis and Materials, part of ALiCE- Associate Laboratory in Chemical Engineering

Supervisor at FEUP: **Dr. Tânia Silva**

Joint supervisors at FEUP: **Prof. Dr. Alexandre Ferreira**

Dr. Vítor Vilar

July 2023

Acknowledgment

First of all, I would like to express how the elaboration of this thesis has changed my perspective of an academic career for the better. I feel that I have learned so much, acquired so many skills, and even improved others that will be useful in my future from a general point of view and not only at work. All the *triumphs and disasters* that accompanied me throughout this thesis have taught me to *treat those two impostors just the same*. All those times when I felt lost and directionless have fuelled my determination to keep going and find a solution, and all those moments when I felt overwhelmed with work have given me the strength to persevere.

Hence, there are many people whom I would like to thank. To begin with, I express my gratitude to my supervisors, Tânia Silva, Alexandre Ferreira, Vítor Vilar, and Rui Boaventura for all the collaboration. Without their support, none of this work would have been possible. I am eternally grateful for the opportunity to work on this innovative project and their assistance throughout the process. They guided me when needed, pushed me out of my comfort zone, and granted me the freedom to shape my work. I would also like to extend a special thanks to Raquel Rocha and Salomé Soares. Although they were not official supervisors, they supported me as if they were, helping me overcome numerous obstacles. Their knowledge and willingness to assist were fundamental in achieving such positive results. Without them, I would not have gained such a wealth of knowledge from this thesis.

A special thank you to my parents, that have made everything that has been to their disposable in order for me to be where I am today, supporting me in every single decision I made. Thank you to my dearest brother, who always has the most pondered think to say in every situation. Lastly, thank my grandmother for keeping the happiness and joy every day.

Finally, I would like to give a big thank you to all my friends from FEUP (Guilherme, Amaral, Gonçalo, João, Carlos, Cati, Diana, Moisés, and Bruno) and my other friends from different parts of my life (Hugo, Bruno, João, Dani, Afonso, Pedro, Mariana, Manuel, António and João). Thank you for being here for me, for pulling me to the ground when I got too much over my head, for pushing me to the limit when you believed I could go further, for all your support, and, most importantly, for making me who I am today.

This work was financially supported by: LA/P/0045/2020 (ALiCE), UIDB/50020/2020 and UIDP/50020/2020 (LSRE-LCM), funded by national funds through FCT/MCTES (PIDDAC); project HyGreen&LowEmissions (NORTE-01-0145-FEDER-000077), supported by Norte Portugal Regional Operational Programme (NORTE 2020), under the PORTUGAL 2020 Partnership Agreement, through the European Regional Development Fund (ERDF); and project CO2-to-CH4 (2022.01176.PTDC), supported by national funds through the FCT/MCTES (PIDDAC

Abstract

Excessive reliance on fossil fuels substantially increased atmospheric carbon dioxide levels, leading to unsustainable global warming and severe weather events worldwide. This presents the most pressing challenge of the 21st century, demanding urgent attention. Artificial photosynthesis is one of the most promising methods to mitigate the energy crisis and global warming simultaneously. However, CO_2 is an extremely stable molecule, and high energy input is needed to break down the molecule. One emerging solution to diminish the energy requirements is using photo-thermal catalysis for CO_2 hydrogenation. By harvesting solar energy and utilizing photocatalysts, CO_2 can be converted into valuable chemical products, such as methane, offering a sustainable energy source. The use of external heating can enhance this phenomenon.

This research aims to develop a highly active and selective catalyst for CO_2 photo-thermal methanation. The investigation explores the use of ruthenium or nickel as plasmonic materials, the impact of different titanium dioxide forms on catalytic performance, several preparation methods, and the influence of the mass fraction of plasmonic metal on the catalyst's performance. The synthesized catalysts were evaluated in a photo-thermal reaction system. Moreover, comprehensive characterization techniques, including N_2 adsorption isotherms at -196 °C, H_2 temperature-programmed reduction, UV-Vis spectroscopy, and X-ray photoelectron spectroscopy, are employed to gain insights into the catalysts' properties.

The findings of this study demonstrate the successful development of a highly active and methane-selective photo-thermal catalyst using the solvothermal impregnation method with PC500 titanium dioxide. The 7.5 wt% Ru/TiO_2 catalyst exhibits outstanding performance, achieving a remarkable CO_2 conversion of 73 % into CH_4 within a short reaction time of 15 min at a moderate temperature of 160 °C. This achievement is accompanied by an impressive maximum yield rate for CH_4 generation, reaching 23.44 $mmol \cdot g^{-1} \cdot h^{-1}$. These results highlight the significant potential of the developed catalyst in the field of CO_2 utilization and sustainable energy production.

Keywords: **Photo-thermal catalysis, CO_2 methanation, catalyst synthesis, plasmonic materials**

Resumo

A dependência excessiva dos combustíveis fósseis para suprir as necessidades energéticas da humanidade resultou num aumento substancial dos níveis de dióxido de carbono na atmosfera, conduzindo ao aumento insustentável da temperatura média e da frequência e potência dos fenómenos climáticos extremos em todo o mundo. O combate às alterações climáticas representa o maior desafio do século XXI, exigindo uma atenção urgente. A fotossíntese artificial é um dos métodos mais promissores para mitigar a crise energética e o aquecimento global em simultâneo. No entanto, o CO_2 é uma molécula extremamente estável e é necessário um elevado consumo de energia para quebrar as suas ligações. Uma solução promissora para diminuir as necessidades energéticas é a utilização da catálise foto-térmica para a hidrogenação do CO_2. Através do aproveitamento da energia solar e da utilização de fotocatalisadores, o CO_2 pode ser convertido em produtos químicos valiosos, como o metano, oferecendo uma fonte de energia sustentável. Este fenómeno pode ser potenciado pela utilização de aquecimento externo.

Este projeto tem como objetivo desenvolver um catalisador altamente ativo e seletivo para a metanação fototérmica do CO_2. A investigação explora a utilização de ruténio e níquel como metais plasmónicos, o impacto de diferentes formas de TiO_2 no desempenho catalítico, a aplicação de vários métodos de preparação e a influência da fração mássica do metal plasmónico no desempenho do catalisador. Os catalisadores sintetizados são avaliados num sistema de reação foto-térmico. Além disso, são utilizadas técnicas de caraterização abrangentes, incluindo adsorção de N_2 a -196 ºC, redução por H_2 com temperatura programada, espetroscopia UV-Vis e espetroscopia de fotoelectrões de raios X para obter informações sobre as propriedades dos catalisadores.

Os resultados deste estudo demonstram a sintetização bem-sucedido de um catalisador fototérmico altamente ativo e seletivo para o metano, utilizando o método de impregnação solvotérmica com dióxido de titânio PC500. O catalisador 7,5 wt% Ru/TiO_2 apresenta um desempenho excecional, alcançando uma conversão notável de 73 % de CO_2 em CH_4 num curto período de reação de 15 min a uma temperatura moderada de 160 ºC. Este resultado é acompanhado por uma impressionante taxa de rendimento máximo para a produção de CH_4 de 23,44 $mmol \cdot g^{-1} \cdot h^{-1}$. Estes resultados realçam o potencial significativo do catalisador desenvolvido no domínio da hidrogenação do CO_2 e da produção de energia sustentável.

Palavras-chave: **catálise foto-térmica, metanação do CO_2, síntese de catalisadores, materiais plasmónicos**

Declaration

I hereby declare, under word of honour, that this work is original and that all non-original contributions is indicated, and due reference is given to the author and source.

Rui Daniel Gonçalves Matias, 3rd of July of 2023

Index

List of Figures

List of Tables

Notation and Glossary

E_g	Bandgap Energy	eV
h	Planck constant	$m^2 \cdot kg \cdot s^{-1}$
k	Pseudo-first order kinetic constant	s^{-1}
m_{cat}	Mass of catalyst	g
n_0	Number of initial moles	mmol
n_{CH4}	Number of moles of CH_4	mmol
n_{CO2}	Number of moles of CO_2	mmol
S_{BET}	Specific surface area	$m^2 \cdot g^{-1}$
t	Time	s
$Y_{r,CH4}$	Yield rate for CH_4 generation	$mmol \cdot g^{-1} \cdot s^{-1}$

Greek Letters

ν	Radiation frequency	Hz
φ_{SB}	Schottky barrier	J

Indexes

i	index of time

List of Acronyms and abbreviations

Anat	Anatase TiO_2
CB	Conduction Band
CCU	Carbon Capture and Utilisation
DRS	UV-Vis Diffuse Reflectance Spectra
EF	Fermy Energy Level
FID	Flame Ionization Detector
ICP-OES	Inductively Coupled Plasma Optical Emission Spectroscopy
Inc	Incipient wetness impregnation
LDH	Layered Double Hydroxide
LSPR	Localised Surface Plasmon Resonance
LUMO	Lowest Unoccupied Molecular Orbital
MNP	Metallic Nanoparticle
MOF	Metallic Organic Framework
NIR	Near Infrared
Rfx	Reflux impregnation
ST	Solvothermal impregnation
TPR	Temperature Programmed Reduction
UV	Ultraviolet
Vis	Visible
Wet	Wet impregnation
XPS	X-Ray Photoelectron Spectroscopy
µTCD	Micro Thermal Conductivity Detector

1 Introduction

1.1 Framing and presentation of the work

The extensive dependence on fossil fuels has caused a dramatic increase in atmospheric carbon dioxide levels over the past few decades. This, in turn, has triggered the onset of global warming and climate change, resulting in a heightened frequency of severe weather events across the globe. This is, undoubtedly, XXI's century biggest problem for humanity that requires an urgent response. One emerging solution to reduce anthropogenic CO_2 emissions is methanation, as a way to capture CO_2 and use it as feedstock to produce a valuable energy vector, methane.

Solar-driven hydrogenation of CO_2 into value-added chemical products is one of the most promising strategies for reducing anthropogenic CO_2. Using solar energy, green hydrogen (H_2), and photocatalysts, CO_2 can be converted into carbon-containing fuels like methane (CH_4) by heterogenous photocatalysis. This approach addresses CO_2 methanation limitations associated with traditional methods, such as high-temperature requirements, improving the sustainability of the process. This approach reduces the energy consumption of conventional catalysis processes by harvesting renewable energy from solar radiation and minimizing the use of external heating, typically derived from fossil fuels. However, despite its potential, the technology still faces challenges in achieving high solar-to-fuel energy conversion efficiency. By combining plasmonic nanostructures and semiconductors to create heterojunctions, the activity of photocatalysts can be significantly enhanced, leading to improved solar-to-fuel energy conversion at moderate operating conditions. Additionally, integrating external heating with photocatalytic systems can improve conversion rates while still minimizing energy requirements compared to traditional catalytic routes.

The overall aim of this project is to synthesise, test, and characterize a highly active photo-thermal catalyst for CO_2 hydrogenation. This comprises studying the application of different plasmonic metals and wide band gap semiconductors, as well as developing a suitable material preparation method.

This was a risky, ambitious, and crucial task as it was part of an FCT exploratory project, but a successful completion will have a significant impact on the scientific community. The proposed research will significantly contribute to going beyond the state-of-the-art in the photo-thermocatalytic CO_2 methanation field. Despite the difficulties faced, the main goal was fully achieved.

1.2 Contribution of the author to the work

The work began with developing a gas chromatography method and its calibration, enabling the analysis of the composition of the reaction medium during catalyst activity assessment experiments. Following that, an existing experimental setup was adapted to enhance its longevity. This involved redesigning the existing installation by replacing components to eliminate leaks and simplifying the setup. Additionally, the author was responsible for developing a LabView program to collect and record data on the reaction medium's temperature. Furthermore, the author undertook the preparation and selection of necessary equipment for future experiments in a continuous-flow reactor. The author carried out the synthesis of all catalysts, the different characterization techniques, and the evaluation of catalysts' activity toward photo-thermal methanation reaction. XPS analysis was performed by CEMUP and interpreted by the author. The author undertook the analysis of the results. The dissertation was written by the author, which used artificial intelligence software to revise and improve the quality of the writing. In summary, the author's contribution was to carry out all the presented work under the guidance of its supervisors.

1.3 Organization of the dissertation

Chapter 1: Introduction. The first chapter, entitled Introduction, is devoted to presenting the addressed problem and the work carried out.

Chapter 2: State-of-the-art. This chapter provides a concise overview of the background concerning photo and photo-thermal catalysis, plasmon-enhanced catalysis, the current state of the art in CO_2 methanation, and crucial photo-thermal catalyst design concepts.

Chapter 3: Materials and Methods. In this chapter, detailed information is provided regarding the reactants used in catalyst preparation, along with an explanation of the experimental protocols developed to synthesize the materials using different preparation methods. Additionally, the chapter describes the experimental setup used to evaluate the catalysts' performance and outlines the procedure for characterizing the synthesized materials.

Chapter 4: Results and Discussion. The results are presented with exhaustive explanation and discussion.

Chapter 5: Conclusion. The main highlights of this work are assessed.

Chapter 6: Assessment of work done. A reflection of the work carried out is made. This chapter also includes prospects for future work.

Chapter 7: References. The last chapter includes the References, where all the bibliography used is present.

2 Context and State-of-the-art

The United Nations has declared that climate change, primarily caused by the increasing levels of anthropogenic greenhouse gas emissions like CO_2[1, 2], is the defining issue of our era[3]. In its most recent report, the Intergovernmental Panel on Climate Change confirmed this and predicted that absent fast actions to reduce CO_2 emissions, the global surface temperature will surpass the 2 °C warming threshold agreed upon in the Paris Agreement in the following decades[4].

As the world's energy demand continues to rise, finding ways to reduce, capture, and valorise CO_2 emissions is essential. In recent times, there has been a growing global emphasis on the Carbon Capture and Utilization (CCU) concept. CCU involves the capture and separation of carbon dioxide from emission gases, followed by its conversion into valuable products. Among the various pathways for CCU, catalytic CO_2 fixation methods have gained significant attention due to their ability to artificially convert CO_2 into reusable fuel or commodity chemicals, offering a broader avenue for CO_2 utilization[5, 6]. One catalytic reaction of particular importance in CO_2 utilization is its hydrogenation into CH_4, commonly referred to as the methanation reaction. This technique is well-suited for large-scale CO_2 fixation, as it enables the conversion of depleted CO_2 into synthetic natural gas, specifically CH_4. The resulting CH_4 can be recycled as a fuel or chemical, thereby contributing significantly to the reduction of CO_2 emissions[7-9].

The utilization of solar energy to convert carbon dioxide into carbon-containing fuels, such as carbon monoxide, formic acid, methanol, and methane, emerges as a possible solution to tackle some limitations associated with the traditional methods, like the requirement of high temperatures, enhancing the sustainability of the process[10-12].

Solar energy is one of the most abundant renewable energy resources available. The so-called solar heterogeneous photocatalysis, which combines sunlight with photocatalysts to start catalytic reactions, is an emerging trend[13]. This approach allows for the utilization of a renewable energy source and reduces the use of external heating, typically derived from burning fossil fuels[14, 15], inherent to conventional heterogeneous catalysis processes[16, 17]. Despite its potential, this technology remains impractical on a large scale due to significant limitations leading to low solar-to-fuel energy conversion efficiency[18, 19].

Historically, thermal and photo-excitation strategies have been viewed as distinct methods for surmounting activation energy barriers. Photocatalysis presents a novel approach to producing the same end products under onset ambient conditions employing a different transition state with reduced potential energy, thereby reducing the energy requirements of the process[20]. The creation of heterojunctions through the combination of plasmonic nanostructures and

semiconductors has been demonstrated to significantly boost the photocatalysts' activity and enhance the solar-to-fuel energy conversion while operating under moderate conditions[21-23]. Such an improvement is ascribed to the synergetic effect of photochemical and thermal reactions over the plasmonic structures. Furthermore, external heating can be effectively integrated with photocatalytic systems, leading to substantial conversion rate uprises while minimizing energy requirements compared to traditional systems.

2.1 Photocatalysis mechanism

Photocatalysis is a relatively new discipline that has yet to reach its full potential. Besides, its ability to drive thermodynamically uphill reactions and produce valuable products is undeniable. This intricate process involves the illumination of a solid semiconductor, typically in nanopowder form, utilizing light from a lamp or solar source in a liquid or gaseous medium. During this process, photons possessing energy equivalent to or surpassing the semiconductor's bandgap (predominantly within the ultraviolet wavelength range) are absorbed, contributing to the photoexcitation phenomenon. Consequently, an electron is elevated from the uppermost position of the valence band to the conduction band, creating a photo-generated hole.

Depending on the extent of absorption within the bulk material, a subset of these photogenerated charges may migrate towards the surface, instigating surface redox reactions. Electrons originating from the conduction band reduce adsorbed electron acceptor molecules, whereas holes stemming from the valence band oxidize electron donor molecules[20, 24].

Despite the promise of photocatalysis as an alternative to traditional thermal methods, the current state of photocatalytic technology is limited by several key challenges, including insufficient light absorption, inadequate charge separation efficiency, and high rates of charge recombination[25-28]. Combining plasmonic materials with semiconductors has emerged as a way to minimize some of these limitations.

2.2 Plasmon-enhanced catalysis, localised surface plasmon resonance, and the photo-thermal effect

Recently, plasmon-mediated processes have garnered significant attention due to their potential for charge separation upon light excitation and their ability to broaden the optical absorption range of semiconductors[25].

Some metallic nanoparticles (MNPs) possess a distinct feature called Localised Surface Plasmon Resonance (LSPR), characterized by a broad and intense absorption band across the ultraviolet-visible-near-infrared (UV-Vis-NIR) region of the electromagnetic spectrum. The LSPR effect enables external incident irradiation to guide the movement of free electrons within MNPs.

However, this motion is hindered by inelastic electron collisions and the restoring force resulting from the accumulation of surface charges. When resonant conditions occur, aligning the incident electromagnetic wave with the resonant frequency of conduction electrons leads to the amplification of the electric field in specific regions referred to as "hot spots" on the surface of plasmonic MNPs[29].

Besides the augmented electric field, the LSPR also gives rise to other properties associated with various relaxation mechanisms within plasmonic structures. Following excitation, the energy stored in surface plasmons can decay through two pathways: radiative pathways, involving the emission of photons, and non-radiative pathways, involving excitations of electron-hole pairs and electron-electron collisions[30]. These non-radiative processes can lead to local heating as the kinetic energy of electrons transfers to the lattice phonons of the metal[31], resulting in an increase in temperature at the catalytically active sites[32, 33]. Additionally, energy dissipation within MNPs can generate energetic hot charge carriers within the plasmonic structure[29], possessing higher energies than those induced by direct photoexcitation[34-36].

One of the factors contributing to plasmon dephasing is electron collisions with the surface of the plasmonic structure, known as surface scattering or “Landau damping”. This quantum mechanical process occurs within femtoseconds, where a plasmon quantum transfers its energy into a single electron-hole pair excitation. These hot carriers can leave the plasmonic MNPs, triggering subsequent chemical reactions[29].

As a result, plasmon-enhanced catalysis is derived from the synergistic combination of three properties arising from LSPR: i) optical near-field enhancement, ii) hot carrier generation, and iii) local heating effect, as seen in Figure 1. When plasmonic materials are added to a semiconductor, they serve two primary purposes. Firstly, they act as an antenna, absorbing a wider range of radiation compared to the semiconductor leading to the emission of energetic electrons to the semiconductor. Secondly, the presence of plasmonic materials promotes heat generation inside the catalyst particle through electron-electron (e^--e^-) and electron-phonon (e^--ph) scattering.

Both hot carriers and the thermal effect contribute to the enhanced overall reaction rate to varying degrees, depending on the operating system. This phenomenon is typical, but not exclusive, from group VIII elements as it can also appear in elements from group IB, IIB, and other *p*-block metals[37].

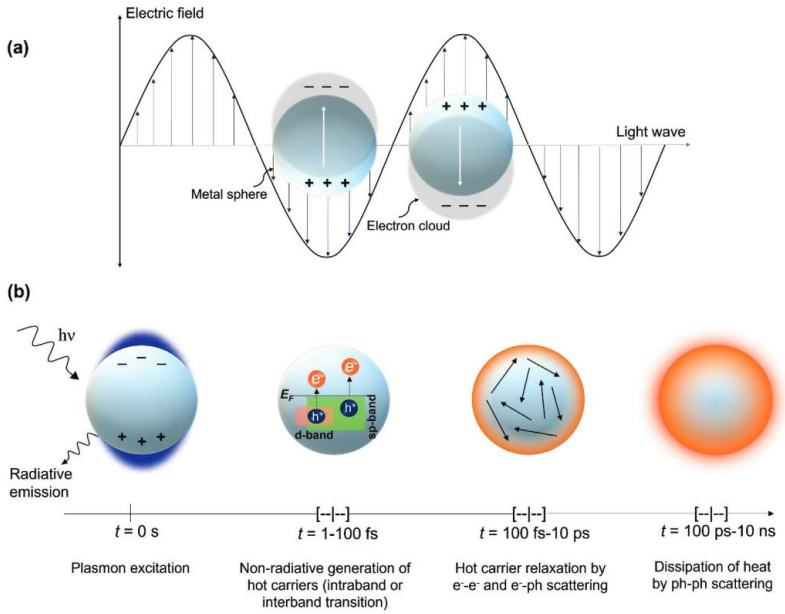

Figure 1: a) Plasmon excitation phenomena and b) associated processes. Reprinted with permission from [38].

2.3 Photo-thermal Catalysis

As previously stated, the photo-thermal effect is a consequence of the collaboration between the thermal and photochemical contributions of non-radiative plasmon decay, in which both the thermal effect, hot carriers, and optical near-field enhancement contribute to augmenting the overall reaction rate. In addition, the application of external heating exhibits the potential to significantly enhance conversion rates and bolster the feasibility of this technology.

2.3.1 Photochemical Enhancement in Plasmonic Structures

As previously mentioned, the excitation of plasmonic MNPs can generate hot carriers, including electrons and holes, through non-radiative processes such as Landau damping during electronic intraband and/or interband transitions[39]. When these MNPs absorb photons with energy *hv*, hot electrons are produced with energies surpassing the Fermi level (EF + *hv*). Subsequently, these energetic electrons can be injected into species with electron-accepting orbitals near the MNPs[39, 40]. Through kinetic energy transfer, these hot electrons activate adsorbates by inducing vibrational or electronic transitions. Notably, promoting high-energy electrons to antibonding orbitals of adsorbed molecules can lead to bond cleavage and subsequent chemical transformations.

In the context of catalytic applications, these hot electrons can be employed through four primary pathways, depending on the utilization of single-component or heterostructure plasmonic photocatalysts. The first two pathways involve the interaction of hot electrons from individual plasmonic MNPs with adsorbates, either through indirect or direct electron transfer.

The remaining two pathways involve the interaction of supported plasmonic MNPs with semiconductors, either through indirect injection to an acceptor or through the direct promotion of the carrier into the conduction band (CB)[41-43].

Indirect hot electron transfer into the adsorbate: The concept of indirect electron transfer suggests that the excitation of plasmons in a metal nanoparticle induces the generation of hot electrons, which subsequently migrate to the lowest unoccupied molecular orbital (LUMO) of an adsorbed species on the metal surface. This process involves the transfer of electrons to the adsorbate after the formation of hot carriers and is limited by energy losses resulting from electron-electron scattering. However, it has been observed that higher incident photon energies yield a greater number of electrons with sufficient energy to be injected into the LUMO of adsorbates, establishing a positive correlation between the efficiency of indirect hot electron transfer and incident photon energy[30, 44, 45].

This mechanism has been experimentally demonstrated in the plasmon-induced activation of small molecules, including molecular hydrogen (H_2)[46, 47]. The generation of hot electrons on plasmonic nanoparticles enables their indirect transfer to the antibonding orbital of adsorbed molecular H_2, forming a negatively charged $H_2^{\delta-}$ species. Subsequently, the electrons are transferred back to the MNPs, while H_2 returns to its electronic ground state with accumulated vibrational energy that surpasses the activation energy barrier, thereby facilitating the dissociation of H_2[46].

Direct hot electron transfer into the adsorbate: The LSPR excitation can also lead to the direct transfer of hot electrons from metal nanoparticles into adsorbates[39, 45, 48]. This process, known as plasmon dephasing, is associated with chemical interface damping, arising from the coupling between unoccupied states of the adsorbate and excited surface plasmons[43]. In the direct transfer mechanism, hot electrons are directly transferred to the hybridized states between the MNPs and the adsorbed molecules, bypassing energy losses resulting from electron-electron scattering[49, 50]. This direct transfer occurs concurrently with the dephasing of the plasmon excitation and is anticipated to exhibit a higher efficiency in electron transfer. However, it necessitates a strong interaction between the adsorbate and the metal surface for surface orbital hybridization, which is not commonly observed in plasmonic photocatalysts. Consequently, the direct electron transfer mechanism is less likely to occur[41, 43, 51].

Indirect hot electron transfer into the semiconductor: In recent years, using supported plasmonic nanoparticles as efficient light absorbers in photocatalytic systems has gained considerable attention. These MNPs exhibit LSPR bands in the visible and infrared regions, enabling the absorption of low-energy photons that are typically unable to generate electron-hole pairs in UV-active semiconductor photocatalysts. This unique feature allows for the

exploitation of a broader range of the solar spectrum, resulting in enhanced light harvesting capabilities compared to traditional wide-band gap semiconductors[52].

A key advantage of integrating plasmonic metal-semiconductor structures is promoting spatial separation of photoinduced electron-hole pairs, effectively reducing charge carrier recombination within the metal and extending their lifetime[50, 53, 54]. This is achieved by the generation of hot carriers within the plasmonic nanoparticles, followed by the transfer of electrons across the metal/semiconductor interface[43].

The formation of a junction between a metal nanoparticle and a semiconductor leads to the alignment of Fermi levels, facilitating the redistribution of charge and achieving system equilibrium[55]. Consequently, the bending of the semiconductor valence and conduction bands occurs, resulting in the formation of a Schottky barrier at the interface. The energy of this barrier, denoted as φ_{SB}, represents the difference between the Fermi level of the metal and the bent interfacial conduction band edge[44, 56]. Notably, the height of the Schottky barrier in heterostructures is typically smaller than the band gap of many semiconductors, enabling the extraction of excited electrons without requiring energy higher than the semiconductor band gap[46].

The injection of hot electrons into the conduction band and their availability for subsequent electron-induced reactions on the semiconductor surface depend on their energy surpassing the energy threshold set by the Schottky barrier. A lower Schottky barrier height allows a greater number of carriers with sufficiently high energies to overcome the barrier, facilitating their participation in chemical reactions. However, it is crucial to strike a balance, as an excessively low Schottky barrier can lead to the back-transfer of electrons to the MNPs, hindering the spatial separation of electron-hole pairs and reducing the average lifetime of charge carriers. Hence, in the design of metal/semiconductor heterojunctions, achieving an optimal balance between these effects is essential[50].

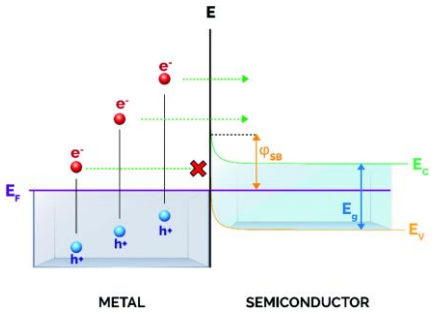

Figure 2*:* Scheme of the metal/semiconductor Schottky barrier. Reprinted from [29].

Direct hot electron transfer into the semiconductor: Direct hot electron transfer into the semiconductor offers a significantly faster and more efficient electron transfer process than the indirect pathway. It occurs within the timescale of hundreds of femtoseconds[44, 57], providing

a higher quantum yield by avoiding energy losses associated with e^--e^- and e^--phonon scattering within the plasmonic nanoparticle[58, 59]. This direct transfer mechanism requires a strong orbital hybridization between the plasmonic and the semiconductor, inducing a single-step transfer of hot electrons to acceptor orbitals in the semiconductor. This occurs simultaneously as plasmon dephasing in metal/semiconductor heterojunctions, ensuring the effective utilization of hot carriers for catalytic processes[60].

2.3.2 Thermal Enhancement in Plasmonic Structures

After the first 100 femtoseconds, when electron-hole recombination occurs upon plasmon decay, hot carriers start decaying via non-radiative pathways, producing heat through inelastic e^--e^- scattering. In parallel, electrons without enough energy to participate in the photochemical mechanism couple with phonons through electron-lattice collisions, increasing the temperature of the metal. This heat is then spread from the metal lattice where it is generated to the surroundings through phonon-phonon scattering. This way, the generated heat can be transferred from the MNPs to the adsorbate, promoting chemical reactions[48, 61, 62].

It is possible to establish that, in a spherical particle, the temperature increase is proportional to the square of the particle radius[63] and, therefore, conclude that the thermal contribution to the photocatalytic rate increases along with the particle size. However, it has been demonstrated that the thermal contribution plays a minor role in the overall photo-thermal catalytic rate when a small amount of MNPs is present[40, 63]. However, this effect can be significantly amplified in the presence of a large number of MNPs due to collective effects[64, 65]. With the proper material engineering, achieving enough plasmon-mediated heating to promote reactions is possible[66, 67]. Nevertheless, integrating external heating and photocatalysis typically results in notably higher reaction rates compared to those attained without such a combination.

Figure 3 shows the most important processes associated with the use of plasmonic materials for heterogeneous photo-thermal catalysis.

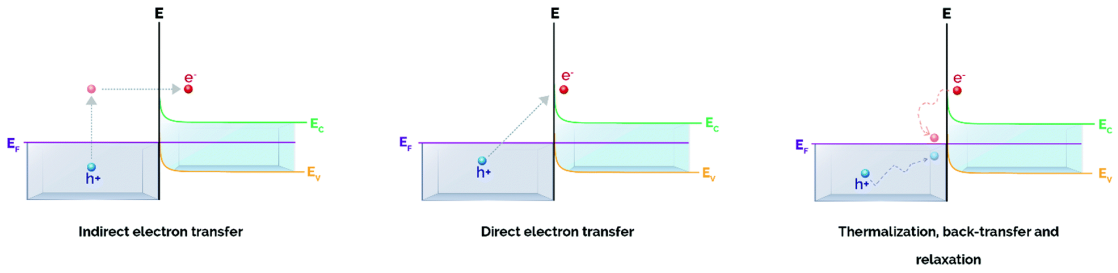

Figure 3: Hot carrier generation transfer/back-transfer processes in metal/semiconductor heterostructures. Reprinted from [29].

2.4 CO_2 Methanation

The hydrogenation of CO_2 to methane is an exothermic reaction that exhibits thermodynamic favourability at lower reaction temperatures. However, achieving adequate reaction rates at these temperatures is challenging due to the inherent stability of CO_2 as a molecule. Therefore, using an appropriate catalyst and higher temperatures becomes necessary to activate CO_2 and attain desirable reaction rates. Due to these facts, CO_2 hydrogenation typically occurs between 300-600 ºC, as higher temperatures can lead to reduced CH_4 selectivity and CO_2 conversion (Figure 4)[68-70]. Under these reaction conditions, alongside the desired CO_2 methanation reaction (Equation 1), other side reactions may arise, including carbon formation (Equation 2) and reverse-water-gas-shift (Equation 3)[71]. The prominence of these side reactions becomes more significant at elevated pressures and temperatures and depends on the employed catalyst[72].

$$CO_2 + 4H_2 \rightleftharpoons CH_4 + 2H_2O \qquad (\Delta H_{298K} = -165\ kJ{\cdot}mol^{-1}) \qquad \text{(Eq. 1)}$$

$$CO_2 + 2H_2 \rightleftharpoons C + 2H_2O \qquad (\Delta H_{298K} = -90.1\ kJ{\cdot}mol^{-1}) \qquad \text{(Eq. 2)}$$

$$CO_2 + H_2 \rightleftharpoons CO + H_2O \qquad (\Delta H_{298K} = 41.2\ kJ{\cdot}mol^{-1}) \qquad \text{(Eq. 3)}$$

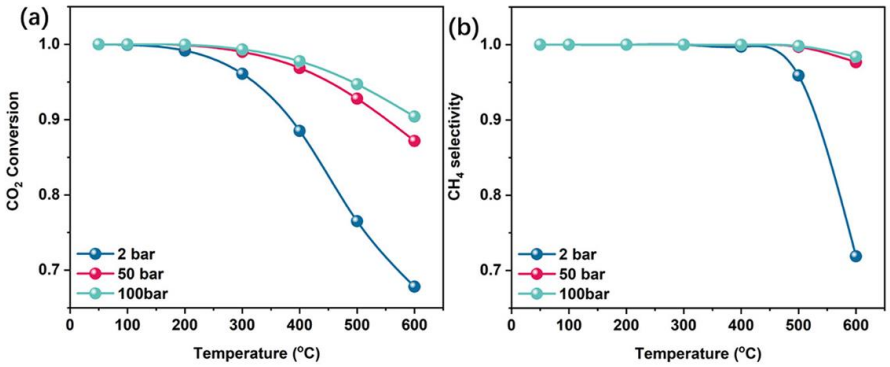

Figure 4: (a) CO_2 conversion and (b) CH_4 selectivity as a function of temperature at 2, 50, and 100 bar, for an $H_2/CO_2 = 4$, determined with a RGibbs model in Aspen Plus. Adapted from [72].

2.5 Design strategies for photo-thermal catalysis

In order to effectively utilize the photo-thermal effect in catalytic processes, photocatalysts must fulfil several criteria, including strong light absorption throughout the solar spectrum, efficient generation of charge carriers, and a high capability for heat production and/or heat transfer. Therefore, material engineering is crucial to develop the best photo-thermal catalyst. To achieve the best possible catalyst, various factors need to be optimized, including, but not limited to, the plasmonic material and semiconductor employed, the composition of the materials, the size and shape of the nanoparticles, and the inclusion of support materials.

2.5.1 Composition

The impregnation of plasmonic materials on the semiconductor structure represents a highly promising approach for developing high-performance catalysts. While the localized surface plasmon resonance phenomenon is commonly associated with group VIII, IB, IIB, and other *p*-block metals, it is not limited to these specific elements[68]. In the realm of CO_2 hydrogenation, ruthenium, rhodium, palladium, and nickel emerge as the most frequently employed metals in catalytic applications[73].

Even at low metal loading and operating temperatures, ruthenium exhibits exceptional catalytic activity and selectivity towards methanation reaction. Its reduced state enables efficient dissociation of hydrogen, which then reacts with adsorbed CO_2 on the catalyst surface. However, the conversion of CO_2 and the yield of CH_4 over Ru-based catalysts depend on crucial factors such as metal loading, particle size and dispersion, support material properties, and the interaction between the active metallic species and the support. Various oxide materials, including CeO_2, ZrO_2, TiO_2, Al_2O_3, and SiO_2, have been utilized as supports for Ru catalysts, with Ru/TiO_2 being widely recognized as the most effective and selective photo-thermal catalyst for CO_2 methanation[74].

In the existing literature, Ni-based catalysts have emerged as the predominant choice for CO_2 methanation, primarily due to their satisfactory catalytic performance, accessibility, and cost-effectiveness. Nonetheless, it is worth noting that Ni-based catalysts typically require higher operating temperatures compared to noble metal-based catalysts. Consequently, the elevated temperatures, combined with the exothermic nature of the methanation reaction, increase the susceptibility of Ni particles to agglomeration and sintering. These undesirable effects ultimately result in catalyst deactivation and a subsequent decline in catalytic activity[71].

In addition to the aforementioned significant nanomaterial types, other materials exhibit noteworthy characteristics and can be used as an alternative or complement to these materials. Among them are carbon nanotubes, graphene, zeolites, metal-organic frameworks (MOFs), perovskites, or layered double hydroxides (LDHs) that particularly deserve attention in this regard[29, 68].

2.5.2 Morphology

The size and shape of plasmonic materials play a significant role in their ability to facilitate the formation of hot charge carriers and induce the photo-thermal effect, as they can impact the LSPR phenomenon. Specifically, these factors can influence the photon absorption to scattering effect ratio and the position of the LSPR peak. By tuning the plasmonic material, it is possible to align the LSPR band with the solar spectrum, thus enhancing the catalytic performance[75, 76].

Increasing the size of the plasmonic MNPs promotes the generation of more hot carriers. However, these particles have relatively low energies, close to the Fermi level, and, therefore, most of the absorbed energy is dissipated in the form of heating after e^--h^+ recombination and e^--e^- scattering[34]. In contrast, smaller particles produce less hot charge carriers but with higher energies and a low lifetime (in the order of femtoseconds)[77]. As previously stated, the higher the energy, the higher the possibility of the e^- to be part of photo-induced reactions since it is more probable for them to overcome the Schottky Barriers and be transferred to the accepter. However, small particles can also present inefficient charge carrier separations[78]. Bigger particles have also shown a shift to the red on their resonant frequency, allowing more efficient harvesting of the light[79, 80]. This way, a good balance in the particle size is mandatory to achieve the best catalyst.

2.6 Photo-thermal CO_2 methanation

Despite being a rapidly growing field, photo-thermal CO_2 methanation still faces challenges due to its recent emergence, particularly the lack of standardised testing protocols. This lack of standardisation poses difficulties in comparing results as experimental conditions and measured outputs vary significantly among studies. To provide a comprehensive overview, Table 1 presents a small compilation of results obtained from various photo-thermal systems operating at relatively mild temperature conditions for CO_2 hydrogenation to methane.

Table 1: Brief overview of recent literature regarding photo-thermal CO_2 methanation.

Catalyst	Light Source	Temperature (°C)	CH_4 production rate ($mmol \cdot h^{-1} \cdot g^{-1}$)	Reference
$RuO_{2(0.4\,\%)}/SrTiO_3$	Xe lamp (1321 W/m^2)	150	14.6	[81]
$Ru_{(2.5\,\%)}/TiO_2$	Xe lamp	325	21.6	[74]
Ru/Al_2O_3	Xe lamp	300[a]	18.16	[73]
2.1 wt% Ni/Al_2O_3	Xe lamp	300[a]	2.30	[73]
Ru/SiNW	Xe lamp (10 suns)	150	1.0	[82]
1 wt% Ru/TiO_2	Xe lamp (14.5 sun)	300	69.49	[83]
1 wt% Ru/TiO_2	Xe lamp (1 sun)	150	1.72	[83]
$Ru/HxMoO_3$-y	Vis-NIR radiation (750 W/m^2)	140	20.8	[84]
$RuO_{2(6.4\,\%)}$:$TiO_{2(16.9\,\%)}$/SBA-15	Xe lamp (250 W/m^2)	150	17.2	[85]

[a] – self-heating.

Mateo *et al.* investigated the formation of CH_4 at 150 °C under irradiation (1321 W/m^2) for three different samples with varying Ru loadings. The inset in the study demonstrated the evolution of CO_2 and CH_4 using 50 mg of $RuO_{2(0.4\ \%)}/SrTiO_3$ at 150 °C, illuminated by a 300 W xenon lamp and 1.05 bar of H_2 and 0.25 bar of CO_2. These conditions resulted in a maximum yield rate of CH_4 ($Y_{r,CH4}$) of 14.6 mmol·g^{-1}·h^{-1}. The lamp was positioned close to the reactor to facilitate effective irradiation[81].

In the study by Chai *et al.*, the $Ru_{(2.5\ \%)}/TiO_2$ catalyst's activity was assessed in a continuous flow fixed bed reactor. The reaction temperature was measured within the catalyst bed using a thermocouple placed in a quartz capillary well. A 200 mg catalyst sample was placed in a 6 mm quartz tube reactor. The reaction was conducted at atmospheric pressure, ranging from 150 °C to 400 °C with a heating rate of 10 °C·min^{-1}. The feed gases consisted of a mixture of 10 % CO_2, 40 % H_2, and 50 % N_2 at a flow rate of 20 mL·min^{-1}. Notably, Ru nanoparticles supported by TiO_2 (001) exhibited superior CO_2 conversion compared to TiO_2 (101), achieving a maximum CH_4 formation rate of 21.6 mmol·h^{-1}·g^{-1} at 325 ºC[74].

Meng *et al.* studied different plasmonic materials for the photothermal CO_2 conversion in a batch-type reaction system with a total volume of 330 ml. The reaction system was initially purged, followed by the injection of 2-2.05 mmol of CO_2 and 8.2-8.5 mmol of H_2, with the molar ratio of H_2 to CO_2 slightly exceeding 4:1. To drive the photothermal CO_2 conversion, a 300 W Xe lamp was used as the irradiation source. Each experiment utilized 100 mg of the catalyst sample, which was spread onto a round-shaped, air-permeable quartz fibre filter with an area of 7 cm^2. The quartz fibre filter film was fixed onto a stage inside the reactor, while the thermometer tip maintained intimate contact with the catalyst sample (with a powder thickness of about 1-2 mm). The lamp was positioned close to the reactor to ensure efficient irradiation. Achieving a maximum CH_4 formation rate of 18.16 and 2.30 mmol·h^{-1}·g^{-1} for the 2.4 wt% Ru/Al_2O_3 and 2.1 wt% Ni/Al_2O_3, respectively. These reactions were performed at approximately 300 ºC induced by the generated heat of the material[73].

In the study conducted by O'Brien *et al.*, gas-phase photocatalytic rate measurements were performed using a custom-built 1.5 mL stainless steel batch reactor equipped with a fused silica glass. The reactor was heated to a temperature of 150 °C and purged with H_2 gas for 10 minutes before feeding a mixture of CO_2 and H_2 at an H_2:CO_2 ratio of 4:1. The photocatalytic reactions were carried out under an illumination intensity of 10 suns. The Ru/SiNW material employed exhibited a CH_4 production rate of 1 mmol·h^{-1}·g^{-1} [82].

In their study, Wang *et al.* achieved an efficient thermo-photo catalytic reduction of CO_2 using 15 mg of a 1 wt% Ru/TiO_2 catalyst in a fixed bed reactor. At 150 °C and 1 atm, $Y_{r,CH4}$ of 1.72 mmol·h^{-1}·g^{-1} was obtained under weak sunlight irradiation (1 sun), whereas no CH_4 was detected

without light. The CH_4 yield increased to 69.49 $mmol \cdot h^{-1} \cdot g^{-1}$ at 300 °C and 14.5 sun irradiation, three times larger than the non-illuminated condition. The photocatalytic reaction was conducted in a quartz reactor with Ru/TiO_2 catalysts on a SiO_2 substrate, using an H_2/CO_2 (in a 3:1 ratio) mixed gas. The lamp was placed near the reactor to provide the necessary light irradiation[83].

Ge *et al.* synthesized a plasmonic hybrid catalyst ($Ru/HxMoO_{3-y}$) using H-spillover, demonstrating excellent photothermal catalytic CO_2 methanation activity under irradiation of 750 W/m^2 and 140 ºC. The catalyst (150 mg) was placed in a stainless-steel flow reactor with a top quartz window. After pre-reduction with H_2, the CO_2 methanation reaction was initiated using a H_2:CO_2 (1:1 ratio) mixture. Illumination was provided by a Xe lamp through the quartz window with a 450 nm cut-off filter. The highest activity was observed with $Ru/HxMoO_{3-y}$ (4 wt% Ru loading), yielding 20.8 $mmol \cdot h^{-1} \cdot g^{-1}$ of CH_4 under light and 4.4 $mmol \cdot h^{-1} \cdot g^{-1}$ under dark conditions[84].

To evaluate the impact of employing black TiO_2 instead of pristine TiO_2, Jin *et al.* conducted CO_2 hydrogenation experiments in a stainless-steel reactor with a sapphire window on the top at 150 ºC with irradiation of 1000 W/m^2 (approximately 13 suns). Initially, 20 mg of 5 wt% Ru/black TiO_2 were uniformly dispersed on a quartz fibre paper, which was then positioned at the bottom of the reactor. The reactor was subsequently sealed, and the remaining air was purged using a gas mixture (CO_2:H_2:N_2 = 1:5:4) for three cycles. Subsequently, the reactor was charged with the mixture gas to a pressure of 4 bar. The experimental results in a CH_4 yield of 93.8 % within 2 hours. The authors also demonstrated a 2.1-fold conversion using black TiO_2 instead of pristine TiO_2[86].

There is a substantial variation in experimental conditions among different studies, making it challenging to compare the results effectively. In addition to the differences in experimental conditions, the varying methodologies employed for result evaluation and the lack of information regarding calculation procedures and important parameters like the distance from the lamp or the utilized irradiance further complicate result comparisons. These factors collectively contribute to the difficulty in drawing meaningful conclusions from the available literature. Addressing these issues by establishing standardized protocols, providing comprehensive details, and ensuring transparency in reporting would greatly facilitate result comparisons and enhance the reliability of research findings.

3 Materials and Methods

3.1 Materials

P25 titanium dioxide (CAS 13463-67-7) manufactured by Degussa (TiO_2-P25), titanium (IV) dioxide 99.8 % in the form of anatase (CAS 1317-70-0) from Sigma-Aldrich (TiO_2-Anat), and CristalACTiV™ PC-500 titanium dioxide (TiO_2-PC500) were employed as semiconductors for the synthesis of catalysts. Ruthenium (III) chloride hydrate (CAS 14898-67-0) from Sigma-Aldrich and Emsure and Nickel (II) nitrate hexahydrate (CAS 13478-00-7) from Sigma-Aldrich were used as precursors for the impregnation of the semiconductor. To prepare black TiO_2, sodium borohydride from Riedel-deHaen was used to reduce the titanium dioxide chemically. Ethylene glycol from Sigma-Aldrich was utilised as a solvent to reduce the ruthenium (III) chloride hydrate. The catalytic reaction test utilised Hydrogen (99.999 %) and CO_2 (99.999 %) obtained from Airliquid as the feedstock. Gas chromatography analysis was performed using Helium (99.999 %) and synthetic air (N_2 + O_2) (99.999 %) from Airliquid, in addition to the aforementioned hydrogen.

3.2 Methods

3.2.1 Catalysts Synthesis

In order to develop a suitable catalyst for photo-thermal CO_2 hydrogenation, various materials were synthesised. This involved investigating the application of different plasmonic metals, like ruthenium and nickel, forms of titanium dioxide and preparation methods. Appendix A provides comprehensive data on the mass-weighted quantities and yields achieved throughout all synthesis processes.

Preparation of Black TiO_2

Extensive research has been conducted on using black TiO_2 (TiO_2-blk) in the photocatalysis field. The specific synthesis process employed in this study has been well-documented in the existing literature[87]. The preparation involved grinding 1 g of P25 or PC500 TiO_2 with 0.375 g of sodium borohydride for 30 min at room temperature with a vibration rate of 10 vibrations·min^{-1} on ball milling equipment (Retsch MM 2000). Then, the resulting mixture was reduced in a tubular furnace under a 100 cm^3·min^{-1} N_2 atmosphere for 3 h at 400 °C, using a heating ramp of 10 °C·min^{-1}. Upon natural cooling to room temperature, the resulting black TiO_2 sample was washed with 200 mL of deionised water and 50 mL of ethanol to remove any unreacted $NaBH_4$ and dried at 100°C overnight.

Incipient wetness impregnation

Incipient wetness impregnation (Inc) was used to prepare three Ni/TiO_2 and three Ru/TiO_2 catalysts with varying nickel and ruthenium contents of 10, 7.5, and 5 wt%. First, 0.5 g of TiO_2 was subjected to ultrasonic treatment for 30 min to enhance particle dispersion. Next, different amounts of ruthenium (III) chloride hydrate or nickel (II) nitrate hexahydrate were added to 0.25 mL of ultrapure water, produced by a Millipore Direct-Q® system (resistivity of 18.2 $M\Omega \cdot cm^{-1}$ at 25 °C). The resulting solution was then dripped onto the TiO_2 in an ultrasonic bath, ensuring complete coverage of the TiO_2 surface with the solution. This procedure was repeated after introducing 0.35 mL of UPW to the flask containing a residual amount of the solution. Following this, the samples were left in the ultrasonic bath for 90 min.

Subsequently, the samples were dried at 100°C to eliminate any remaining water and placed in a tube furnace. For the Ni/TiO_2 samples, a heating ramp of 10 °C·min^{-1} up to 400 °C under a 100 $cm^3 \cdot min^{-1}$ N_2 atmosphere was employed, and this temperature was sustained for 3 hours with an H_2 flow rate of 100 $cm^3 \cdot min^{-1}$. Afterwards, the samples were allowed to cool naturally under the same N_2 flow rate. For the Ru/TiO_2 samples, a heating ramp of 10 °C·min^{-1} up to 250 °C under a 100 $cm^3 \cdot min^{-1}$ N_2 atmosphere was used, and this temperature was maintained for 3 hours with an H_2 flow rate of 100 $cm^3 \cdot min^{-1}$. After this, the samples were left to cool naturally under the same N_2 flow rate.

Similarly, a 10 wt% Ni/TiO_2 catalyst was prepared using incipient wetness impregnation with the black P25 TiO_2. Figure 5 presents a schematic representation of the process.

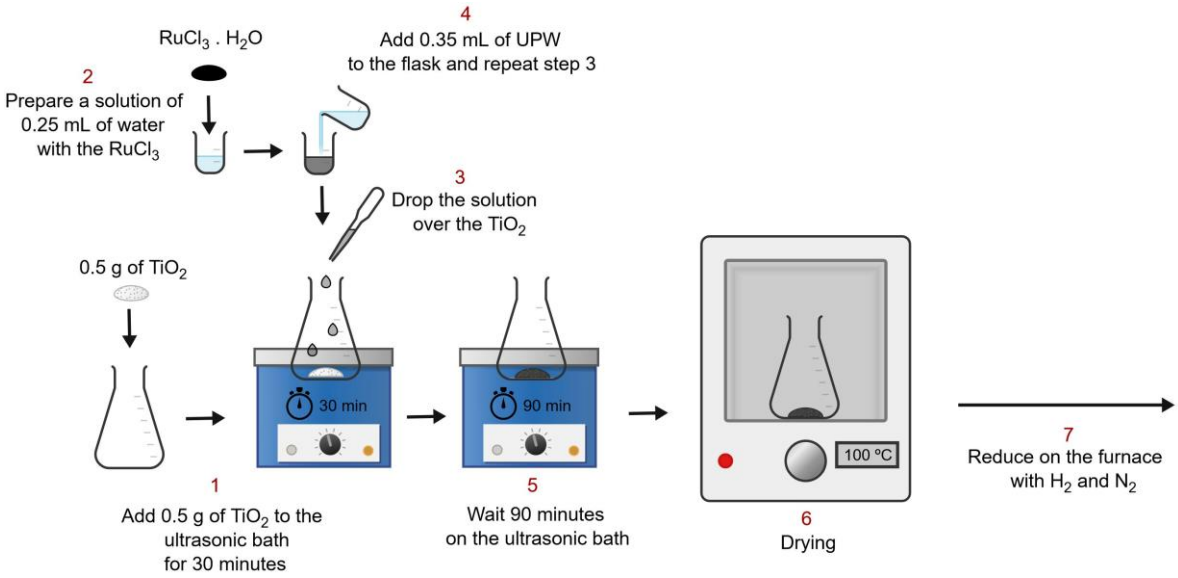

Figure 5: Sequential preparation methodology of the Ru/TiO_2 catalyst using the incipient wetness impregnation method.

Wet impregnation

Wet impregnation, a very common approach to preparing catalysts, was also applied to prepare a 10 wt% Ni/TiO_2 catalyst by sonicating (Hielscher UP400S) 0.5 g of PC500 TiO_2 in the presence of 40 mL of water for 30 min, under the conditions of 80 % amplitude and a complete cycle. Subsequently, 0.275 g of nickel (II) nitrate hexahydrate were added to the solution, and the sonication process was continued for an additional 30 min under the same conditions.

Following the sonication step, two distinct approaches were examined. In the first approach, the solution was mixed for further 17 h at 200 rpm and, subsequently, dried overnight. In contrast, the second approach involved immediate solution drying following the sonication process. The outcomes of these two approaches were evaluated and compared to determine their respective efficacies.

The next step involved drying the samples at 100°C to eliminate any remaining water, followed by their reduction in a tube furnace. This reduction occurred using a gradual heating rate of 10 °C·min^{-1} under a 100 cm^3·min^{-1} N_2 atmosphere until reaching a temperature of 400°C. This temperature was maintained for 3 h while exposing the samples to an H_2 flow rate of 100 cm^3·min^{-1}. Subsequently, the samples were allowed to cool naturally under an N_2 continuous flow of 100 cm^3·min^{-1}, as presented in Figure 6.

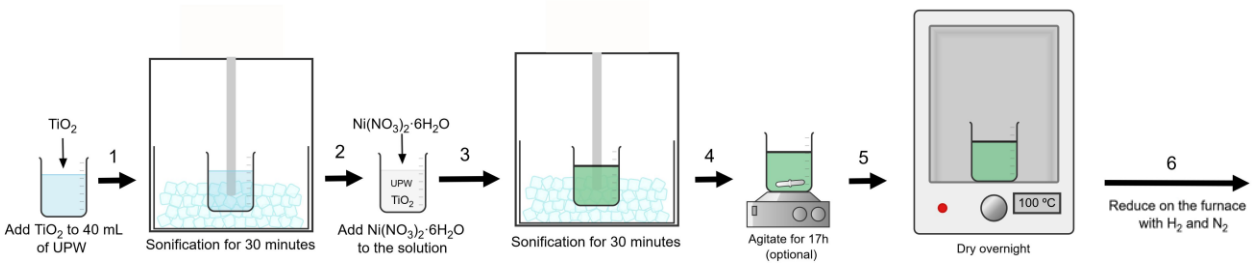

Figure 6: Sequential preparation methodology of the Ni/TiO_2 catalyst using the wet impregnation method.

Reflux method

The reflux method (Rfx) was used to prepare a 10 wt% Ru/TiO_2 catalyst and a 10 wt% Ni/TiO_2 catalyst. Initially, 0.5 g of PC500 TiO_2 were sonicated for 30 min (Hielscher UP400S) in 100 mL of ethylene glycol (80 % amplitude, complete pulse). Next, ruthenium (III) chloride hydrate or nickel (II) nitrate hexahydrate was added to this solution, which was again sonicated for 30 min under the same conditions. Then, the resulting mixture was refluxed for 5 h at 100 °C with constant stirring at 500 rpm. After this step, the reflux was maintained for another 8 h at 180 ºC and continuous stirring of 500 rpm. The resulting solution was mixed with 200 mL of

deionised water and 50 mL of acetone and centrifugated (VWR Mega Star 1.6) for 20 min under 4500 rpm. Afterwards, the liquid phase was separated from the solids, and the previous step was repeated. Lastly, the solids were dried at 100ºC for 2 h and calcinated at 350°C (Nabertherm Furnace) for 3 h to oxidise the material.

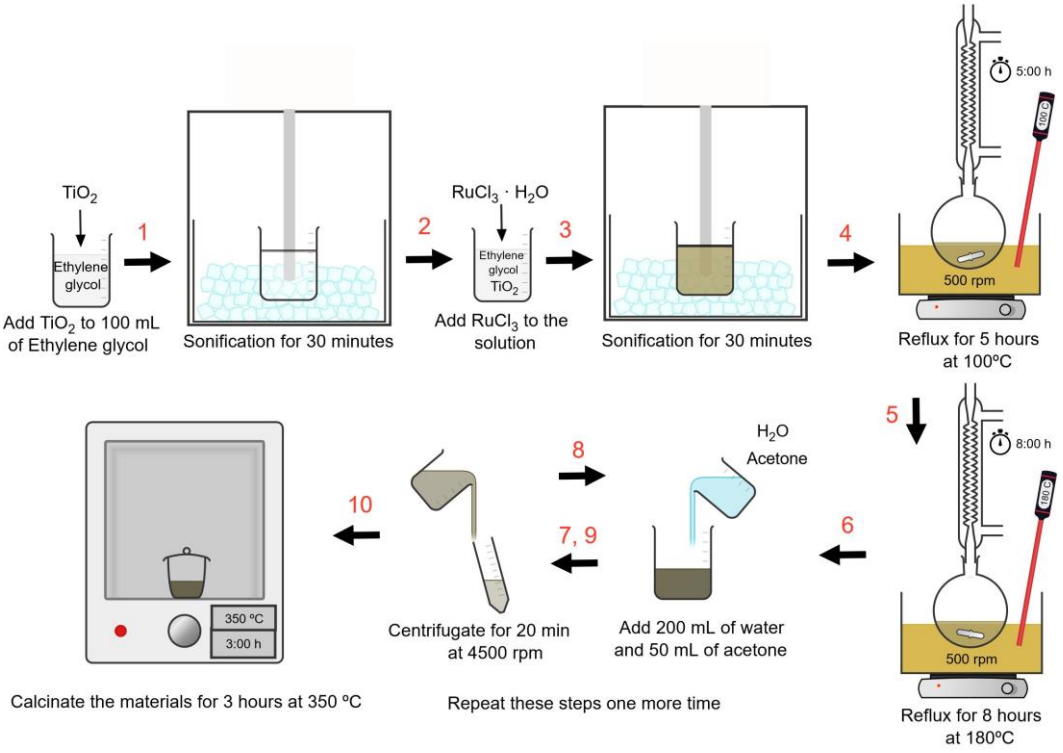

Figure 7: Sequential preparation methodology of the Ru/TiO_2 catalyst using the reflux method.

Solvothermal synthesis

Solvothermal synthesis (ST) was used as an alternative to the reflux method to prepare Ru/TiO_2 and Ni/TiO_2 catalysts with different metal loads. Initially, 0.5 g of TiO_2 were sonicated for 30 min (Hielscher UP400S) in 100 mL of ethylene glycol (80 % amplitude, complete pulse). Next, different amounts of ruthenium (III) chloride hydrate or nickel (II) nitrate hexahydrate were added to this solution that was, again, sonicated for more 30 min under the same conditions. The resulting mixture was added to an autoclave reactor, using a Teflon container, for 15 h at 180 ºC. The reduced solution was mixed with 200 mL of deionised water and 50 mL of acetone and centrifugated (VWR Mega Star 1.6) for 20 min under 4500 rpm. The liquid phase was separated from the solids, and the previous step was repeated. The solids were then dried at 100 ºC for 2 hours and calcinated at 350°C (Nabertherm Furnace) for 3 h to oxidise the material.

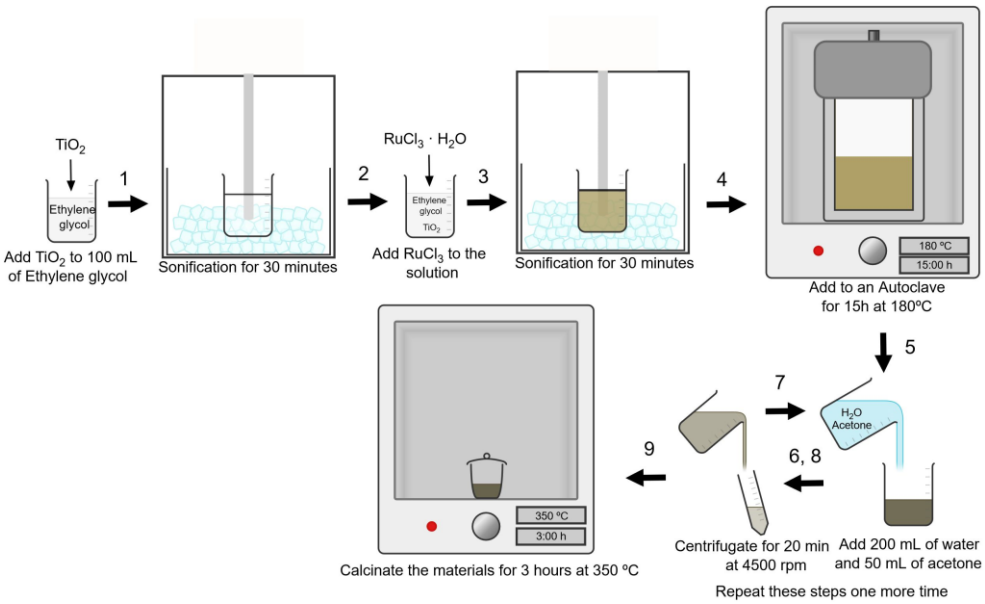

Figure 8: Sequential preparation methodology of the Ru/TiO_2 catalyst using the solvothermal synthesis method.

3.2.2 Catalysts Characterisation

In order to gain insights into the characteristics and behaviour of certain catalysts, additional characterisation techniques were employed. Specifically, UV-Vis diffuse reflectance spectroscopy (DRS), N_2 adsorption-desorption at -196 ºC, temperature-programmed reduction (TPR), and X-ray photoelectron spectroscopy (XPS).

The catalysts' reactivities were evaluated through the analysis of TPR data. The data was acquired using the fully automated AMI-200 Catalyst Characterisation apparatus (Altamira Instruments), which was equipped with a thermal conductivity detector (TCD). The TCD was used to measure the amount of hydrogen consumed during the reduction process. In each experimental trial, a sample weighing 0.030 g was placed in a U-shaped quartz tube within an electric furnace. Then, the sample was heated from room temperature to 800 °C at a rate of 10 °C·min^{-1}. A mixture of 5 vol% H_2/Ar was continuously flowed through the tube at a rate of 29 cm^3·min^{-1}. After each analysis, a hydrogen calibration was conducted at 50 °C.

The materials' textural properties were determined by N_2 adsorption–desorption at -196 ºC on a Quantachrome Autosorb-iQ2 apparatus. Before analysis, each sample (100 mg) was outgassed under a high vacuum at 150 ºC for 12 h. The textural properties of the 10 wt% Ru/TiO_2-Anat were determined on a Quantachrome NOVA 4200e. Each sample (100 mg) was outgassed under a high vacuum at 150 ºC for 3 hours before analysis.

UV–Vis absorption spectrophotometer Jasco V-560 from PG Instruments Ltd. was employed to measure the absorption spectra of different catalysts in the wavelength range of 220-800 nm.

The XPS analyses were performed to evaluate the superficial metal load using a Kratos AXIS Ultra HSA, with VISION software for data acquisition and CASAXPS software for data analysis. The analysis was carried out with a monochromatic Al Ka X-ray source (1486.7 eV), operating at 15 kV (90 W), in FAT (Fixed Analyser Transmission) mode, with a pass energy of 40 eV for regions of interest (ROI) and 160 eV for the survey.

3.2.3 Photo-thermocatalytic CO_2 methanation tests

To assess the performance of the prepared catalysts, a series of batch experiments were performed within a 40 mL cylindrical transparent quartz glass reactor inside an Atlas Suntest XLS^+ solar simulator that facilitated photo-induced catalysis by simulating sun irradiation, equipped with a 1700 W xenon lamp (emitting irradiances between 250 and 750 W/m^2 within the wavelength interval from 280 to 3000 nm). The Suntest chamber was also equipped with a blue-coated light filter that was removed in some experiments to evaluate the influence of adding NIR radiation to the system. In all experimental trials, the glass reactor was consistently positioned at 25 cm from the lamp. Additionally, an external heating tape controlled by an RC-114M on-off controller was applied to the reactor to raise the temperature, thus promoting thermal catalysis. The information about the temperature inside the reactor was acquired using a LabView program connected to a K-type thermocouple inside the reactor.

In order to allow online detection/quantification of the reactants and products at the same time, the GC analytical system is composed of: (i) a Carbon Plot column (30 m × 0.32 mm × 3.0 µm, Agilent Technologies, California, USA), (ii) two detectors, (1) a micro-thermal conductivity detector (µTCD), with the sensitivity of 400 $pg \cdot mL^{-1}$, for H_2 quantification, followed by (2) a flame ionisation detector (FID), with sensitivity 1.5 $pg_{carbon} \cdot sec^{-1}$ for CO_2, CH_4, and ethane (C_2H_6) quantification; and (iii) one methaniser, placed between the µTCD and FID, to convert CO_2 into CH_4. The molar composition of the gas mixture inside the photoreactor was estimated by area normalisation with response factors.

The thermo-photocatalytic methanation experiments proceeded as follows: (i) firstly, the catalyst was added to the quartz reactor (approx. 100 mg) followed by 10 min purge with H_2 flux; (ii) then, the mixture of H_2 and CO_2 were fed to the reactor ($[CO_2]$:$[H_2]$ molar ratio of approximately 1:4) by pressure control (PCO_2:PH_2 (bar/bar) of 0.5:2.0); (iii) before starting the reaction, the first sample was taken at ambient temperature after leaks checking until the pressure inside the reaction achieves 1.6 bar; iv) subsequently, the heating system was activated and set to the desired temperature (100, 130 or 160 ºC). After a brief period, once the temperature reached the predetermined setpoint, the radiation source was activated. Upon completion of the desired reaction time, the lamp was deactivated (500 W/m^2), and a sample was collected, ensuring sufficient gas flowed through the tube to purge any residual sample from the previous analysis.

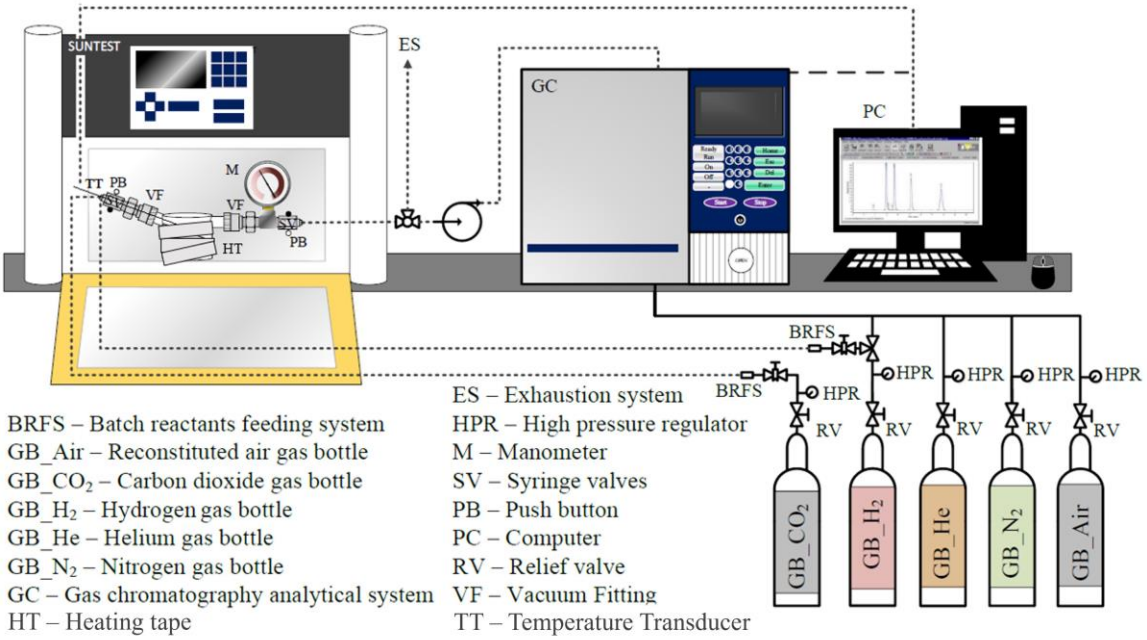

Figure 9: Scheme of the experimental photo-thermocatalytic CO_2 methanation system set up, comprising the quartz reactor, the Suntest chamber and the data acquisition system.

The diverse experimental conditions employed in each catalytic test, as well as the corresponding results, are comprehensively summarised in Table B.1, present in Appendix B.

The initial set of experiments was undertaken to assess the effects of employing diverse plasmonic metals, varied metal loads, distinct forms of titanium dioxide, and different preparation methodologies. To evaluate these factors, batch experiments were conducted under identical conditions for all materials, with subsequent measurements of CO_2 conversion following a predetermined duration. After identifying optimal preparation parameters, multiple experiments were performed to examine the influence of temperature on the system, the impact of NIR radiation, and the assessment of synergistic effects resulting from photo and thermal catalysis. Lastly, the maximum $Y_{r,CH4}$ was determined for the most promising catalysts and experimental conditions to facilitate comparing the outcomes with those presented in the existing literature.

4 Results and Discussion

The work presented in this study is divided into two main parts. The first part focuses on exploring various parameters to develop an optimal catalyst, including: i) selecting a suitable plasmonic material; ii) investigating the effects of using different forms of the TiO_2 semiconductor; iii) employing diverse preparation methods, and iv) determining the optimal catalyst composition. Reaction tests were conducted under the conditions outlined in Table B.1 (Appendix B) to evaluate the CO_2 photo-thermal conversion achieved with each catalyst material. Additionally, to gain further insights into the underlying phenomena, selected materials were characterised by XPS, N_2 adsorption-desorption analysis, H_2-TPR, and UV-Vis spectroscopy.

In the second part, using the best catalyst obtained from the first part, the focus shifts to examining the influence of NIR radiation, the impact of temperature, and the synergistic effects between photo and thermal catalysis. In the end, the reaction rate constant and the $Y_{r,CH4}$ were determined to compare the obtained results with the existing literature. By assessing these parameters, a comprehensive understanding of the catalyst´s performance towards photo-thermal CO_2 methanation reaction and its comparability to previous studies was achieved.

4.1 Influence of the catalytic material

4.1.1 Plasmonic metal

Ruthenium emerged as the predominant plasmonic material for integration into the TiO_2 framework to enhance photo-thermal catalysis. Nevertheless, nickel exploration as a viable alternative has gained considerable attention due to its cost-effectiveness, plasmonic capabilities, and potential for facilitating thermal catalysis, given its widespread utilisation as a catalyst in common methanation processes[73, 88]. This way, an evaluation was conducted to test the performance of nickel catalysts, aiming to comprehend the feasibility of employing this material instead of ruthenium.

Using incipient wetness impregnation, six distinct catalysts containing 10, 7.5, and 5 wt% of ruthenium or nickel were synthesised utilising TiO_2 in the anatase crystalline phase (TiO_2-Anat).

The findings, presented in Figure 10, indicate that, under these conditions and with this preparation method, nickel catalysts perform significantly better than ruthenium catalysts, achieving a maximum conversion of 2.48 % compared to a maximum conversion of 0.09 % observed for ruthenium catalysts.

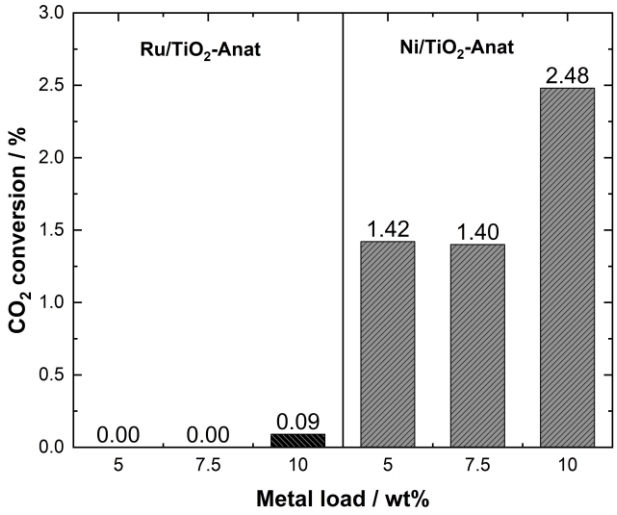

Figure 10: CO_2 conversions after 2-hour irradiation at 130 ºC as a function of the plasmonic metal (Ru or Ni) load on the TiO_2-Anat-based catalyst, prepared by incipient wetness impregnation.

The results also reveal that an increase in the mass fraction of the plasmonic material led to a boost in the catalyst's performance, resulting in a higher CO_2 conversion. Nonetheless, since the study investigated a maximum mass fraction of 10 %, further investigations are necessary to identify the optimal mass fraction to use.

However, the very low conversions observed after a 2-hour reaction and the unexpected difference in performance between nickel and ruthenium catalysts implied that either the form of TiO_2 or the preparation method employed were not suitable for developing high-performance photo-thermal catalysts for this process.

Given the inconclusive outcomes of the aforementioned tests, additional tests were conducted utilising nickel and ruthenium. This approach was adopted to obtain more substantial conclusions and insights.

4.1.2 TiO_2 semiconductor form

As previously discussed, one possible explanation for the low CO_2 conversions observed with the catalysts mentioned in the previous subsection is attributed to the TiO_2 form. Therefore, to investigate its influence on the catalytic performance, the preparation method and material composition were kept constant while varying the TiO_2 form. Three 10 wt% Ni/TiO_2 catalysts were synthesised through incipient wetness impregnation using anatase from Sigma-Aldrich, PC500, and black TiO_2 prepared from P25 TiO_2. Along with that, two 10 wt% Ru/TiO_2 catalysts were synthesised through incipient wetness impregnation using anatase from Sigma-Aldrich or PC500. The conversions achieved under the same operating conditions with these catalysts are displayed in Figure 11.

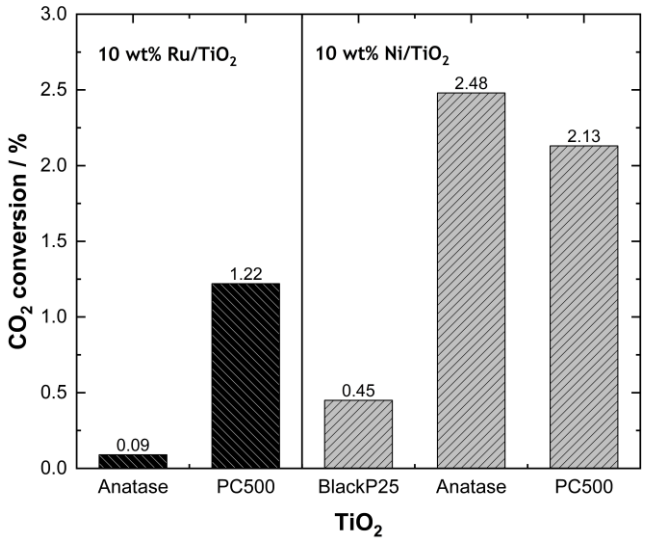

Figure 11: CO_2 conversions after 2-hour irradiation at 130 ºC as a function of the TiO_2 form using 10 wt% Ru/TiO_2 and Ni/TiO_2 prepared by incipient wetness impregnation.

The chemical reduction process employed to generate black TiO_2 from PC500 TiO_2 yielded unsatisfactory outcomes. Unlike the anatase form, the reduction of PC500 failed to produce a homogeneous black-coloured TiO_2, resulting in a mixture of black and white TiO_2 powder. Consequently, the black PC500 TiO_2 sample was excluded from subsequent experimental investigations.

Anatase TiO_2 showed similar activity as PC500 for the Ni/TiO_2 catalyst. However, black P25 showed a 5.5-fold decrease in CO_2 conversion compared to other TiO_2 forms. Such results are concordant with previous conclusions achieved in the existing literature regarding the use of P25 TiO_2 for gas-phase photocatalysis. TiO_2-P25, which consists of approximately 80 % rutile and 20 % anatase, was developed to enhance the overall photocatalytic activity of TiO_2. Nevertheless, the anticipated improvement resulting from the synergistic effect of both phases did not materialise. In the context of gas-phase photocatalytic reactions, the effectiveness of the interaction between the two phases of P25 may be limited, thereby hindering the manifestation of synergistic effects. Insufficient band bending can impede the interaction between the two phases, resulting in compromised separation of charge carriers and consequent reduction in the photo efficiency of mixed-phase TiO_2[89]. Consequently, black TiO_2 derived from TiO_2-P25 and TiO_2-P25 itself were excluded from subsequent analysis. Pristine P25 TiO_2 was not utilized in this study due to literature reports suggesting that black TiO_2 prepared with P25 enhances the photo-thermal CO_2 hydrogenation process when compared to the non-reduced form[86, 87].

CristalACTiV™ PC-500 is a high surface area and high purity ultrafine TiO_2 powder dedicated to photocatalytic applications. Similar to anatase TiO_2 from Sigma-Aldrich, PC500 predominantly comprises the anatase phase, accounting for approximately 99 % of its weight. Nonetheless,

notable distinctions arise when comparing PC500 with anatase TiO_2 sourced from Sigma-Aldrich. The latter exhibits a surface area ranging from 45-55 $m^2 \cdot g^{-1}$, whereas pristine PC500 TiO_2 boasts a surface area exceeding 300 $m^2 \cdot g^{-1}$. This might explain the 13.6-fold increase in CO_2 conversion when PC500 is employed instead of anatase for the 10 wt% Ru/TiO_2 catalyst. TPR and N_2 adsorption tests were conducted to assess the impact of employing anatase from Sigma-Aldrich or PC500 TiO_2 on the reactivity and surface area of the 10 wt% Ru/TiO_2 catalyst prepared using incipient wetness impregnation. The experimental findings are presented in Figure 12.

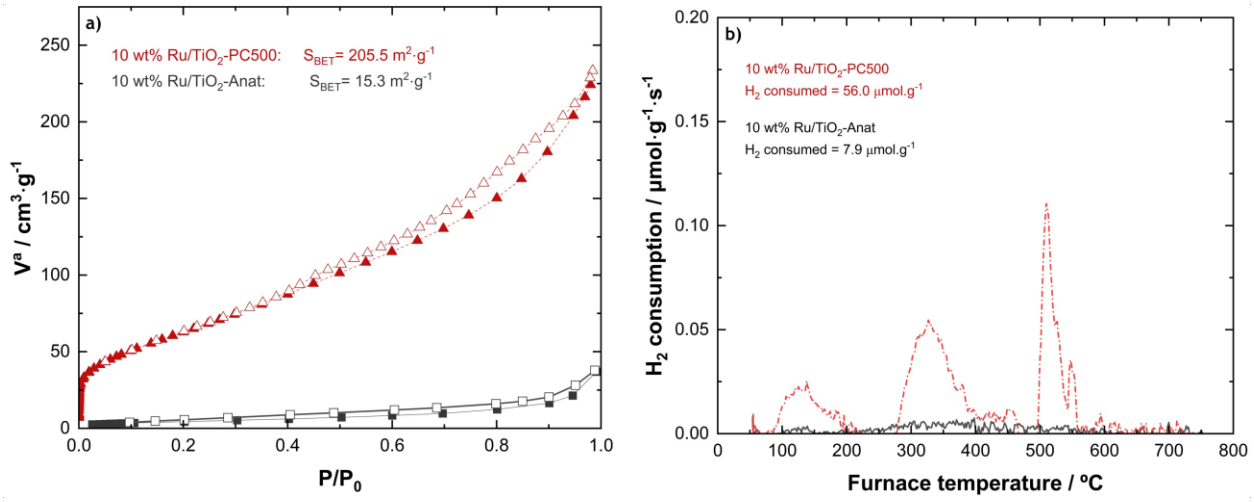

Figure 12: a) N_2 adsorption-desorption (solid-open symbols) isotherms, along with surface area (S_{BET}) values and b) H_2-TPR profiles, along with H_2 consumed values, for the 10 wt% Ru/TiO_2 catalyst prepared with anatase (■, □, solid dark-grey lines) or PC500 (△, ▲, red dashed-dot lines) TiO_2 through incipient wetness impregnation.

The obtained results indicate a significant disparity in surface area between the catalyst produced with PC500 and the one prepared with anatase. Specifically, the catalyst utilising PC500 exhibited a notably larger surface area, approximately 13.4 times greater, compared to the catalyst employing anatase. This substantial difference was expected, considering the inherent characteristics of the TiO_2 before impregnation. The increased surface area observed with the PC500 catalyst can support the enhanced reactivity, as evidenced by the improved CO_2 conversion and the notable increase in H_2 consumption during the TPR test. The augmented surface area likely facilitates the dispersion of impregnated ruthenium, leading to the formation of smaller ruthenium particles and more active sites.

Impregnation of Ru results in a significant reduction in the surface area of TiO_2 compared to its pristine forms. This reduction can be primarily attributed to the deposition of the metal onto the semiconductor surface. This effect is particularly evident in TiO_2-Anat, where the surface area is reduced by approximately 70 %, contrary to TiO_2-PC500, which experiences a loss of approximately 35 % when compared to the respective pristine forms of TiO_2.

Considering that using PC500 exhibited superior performance compared to anatase in the Ru/TiO_2 catalyst, likely attributed to its significantly higher surface area, PC500 was chosen as the preferred TiO_2 for subsequent catalyst synthesis.

4.1.3 Catalyst preparation method

Given the low CO_2 conversions achieved for the previous catalysts, the effect of several methodologies was investigated to establish an effective approach for synthesising the optimal catalyst. In this sense, four distinct methods were addressed to fabricate 10 wt% Ru/TiO_2 and 10 wt% Ni/TiO_2 catalysts with PC500 TiO_2: incipient wetness impregnation, wet impregnation, reflux impregnation, and solvothermal synthesis. Figure 13 compiles the CO_2 conversions obtained with the catalysts synthesised by different preparation methods, keeping all other operating conditions constant, along with the yield achieved for each synthesis process.

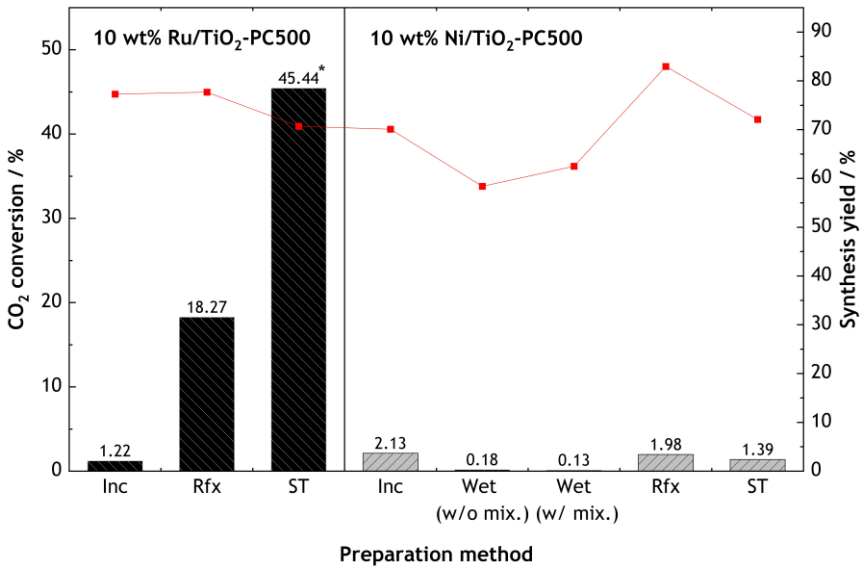

Figure 13: CO_2 conversion (bars) achieved after 2-hour solar irradiation at 130 ºC for 10 wt% Ni/TiO_2-PC500 and 10 wt% Ru/TiO_2-PC500 catalysts prepared by different methodologies and material synthesis yield (■) of each preparation method. * - This reaction was performed in just 1 hour due to experimental limitations.

When looking for the material's synthesis yields, no significant difference is found, except for the wet impregnation methods that present a considerable increase in the material loss, compared to the other methods.

The synthesis method appears to have a significant impact on the performance of the catalyst, as can be confirmed by the results achieved with Ru/TiO_2. When using Ni/TiO_2 catalysts, low conversions are consistently observed regardless of the method employed.

Among the various preparation methods explored for synthesising Ru/TiO_2 catalysts, it was found that incipient wetness impregnation produced the least active catalysts. On the other

hand, solvothermal synthesis emerges as a favourable approach for generating highly active catalysts, exhibiting, under the defined experimental conditions, a CO_2 conversion 2.5 times higher than that achieved through the reflux method, previously investigated within the research group, in just half of the time. This enhanced performance can be attributed to the more efficient reduction of the catalyst in ethylene glycol medium, as evidenced by the distinct coloration of the solution obtained after the reduction step in each method (see Figure 14). These findings underscore the potential benefits of solvothermal synthesis in preparing improved catalyst activity by enhancing the reduction and dissolution process through increased pressure and temperature conditions.

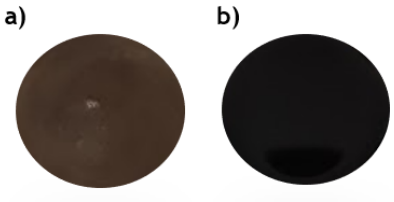

Figure 14: Colour of the resultant solution following the reduction step of ruthenium and TiO_2 using ethylene glycol via a) the reflux method and b) the solvothermal method.

TPR and N_2 adsorption analysis were performed to evaluate how the preparation method affects the reactivity and surface area of the 10 wt% Ru/TiO_2-PC500 catalyst. Additionally, XPS analyses were conducted to gain insights into the impact of the preparation method on the surface mass fraction of ruthenium. Figure 15 compiles all the results regarding the characterisation of the 10 wt% Ru/TiO_2 catalysts synthesised by different methodologies.

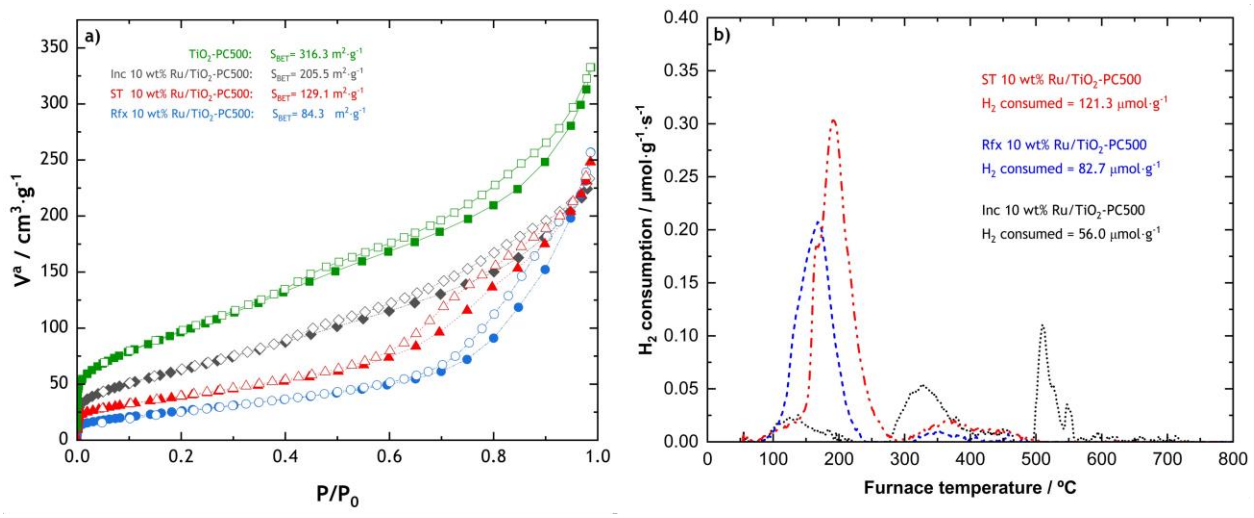

Figure 15: a) N_2 adsorption-desorption (solid-open symbols) isotherms, along with surface area (S_{BET}) values and b) H_2-TPR profiles, along with H_2 consumed values, for the 10 wt% Ru/TiO_2-PC500 catalyst prepared by solvothermal (▲, △, red dash-dot-dot lines), reflux (●,○, blue dash lines) or incipient wetness (◆,◇, dark grey dot lines) impregnation.

Compared to solvothermal synthesis, the reflux method resulted in a slight increase in ruthenium superficial mass fraction (from 6.22 % to 8.45 %, determined with XPS data), which could, theoretically, lead to an improvement in the photo-thermal catalytic activity. However, this method also caused a significant reduction in the catalyst's surface area. The catalyst prepared by reflux also exhibited lower H_2 consumption, although the slightly shifted maximum peak to lower temperatures (from 190 ºC to 170 ºC). On the other hand, solvothermal synthesis, despite lower ruthenium impregnation efficiency compared to reflux, maintained a considerably higher surface area of the PC500 TiO_2 (experimentally determined to be 316.2 $m^2 \cdot g^{-1}$), increasing it by about 65 % when compared to the material prepared by the reflux method. This variation in the surface area can be attributed to the preparation method or the ruthenium content, as previously discussed. These factors, along with the aforementioned differences evaluated after the preparation of the materials, explain the increased reactivity observed in the material during TPR and photo-thermal catalytic testing (Figure 13). Although incipient wetness impregnation showed superior surface area maintenance and potentially higher ruthenium impregnation efficiency, it did not yield a reactive catalyst, as evidenced by the TPR data.

The light absorption spectra of 10 wt% Ru/TiO_2 catalysts synthesised by different preparation methods were analysed using UV-Vis spectroscopy, whose results are disclosed in Figure 16a). It can be observed that reflux and solvothermal synthesis yield materials with comparable results and behaviour across the spectrum, although the reflux method exhibits a slight increase in absorbance for visible and near-infrared radiation compared to the material prepared via solvothermal synthesis. However, the most significant difference arises from the incipient wetness impregnation method, which leads to significantly lower absorbances for wavelengths above 550 nm. This discrepancy may help explain the reduced CO2 conversion observed compared to the other synthesis methods (Figure 13) since distinct material properties may arise from this synthesis method. Nonetheless, incipient wetness impregnation allows the catalyst to capture more photons between 350 and 550 nm. This different behaviour of the material helps prove that, unlike reflux and solvothermal impregnation that produce similar materials, incipient wetness impregnation produces catalysts with considerable disparities, resulting in lower CO_2 conversions.

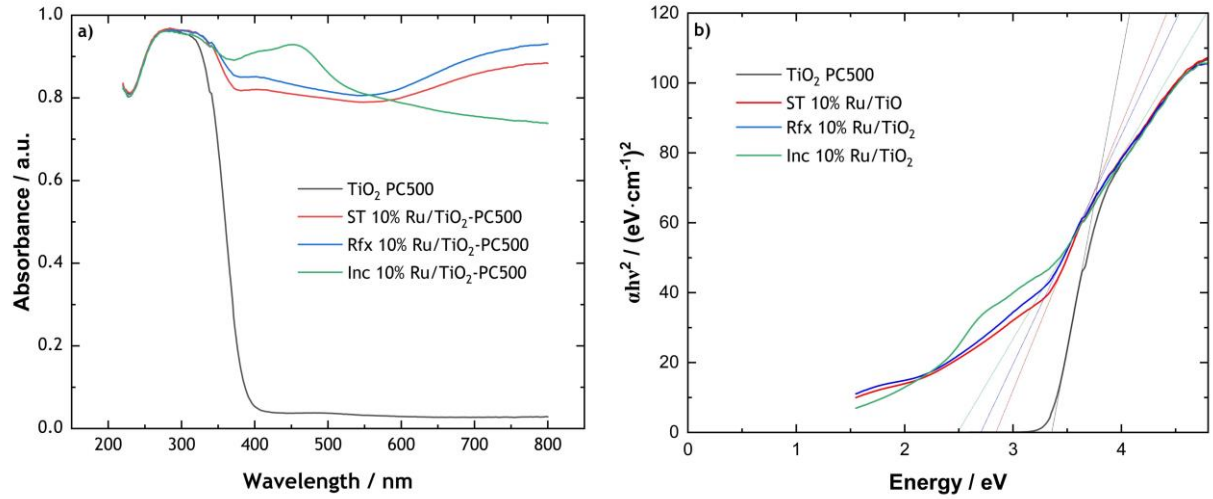

Figure 16: (a) UV-visible absorption spectra of PC500 TiO_2 and 10 wt% Ru/TiO_2-PC500 and (b) Tauc plot of PC500 TiO_2 and 10 wt% Ru/TiO_2-PC500 prepared with different synthesis methods.

The continuous strong absorption of the Ru/TiO_2 catalysts across all the UV-Vis-NIR ranges is conducive to the full sunlight spectrum utilisation, enhancing the overall solar-to-fuel conversion efficiency.

The Tauc plot analysis, as shown in Figure 16b), enables the assessment of the synthesis method's impact on the catalyst bandgap. The optical bandgap energy (E_g) values obtained are 3.29 eV for TiO_2 and 2.82, 2.66, and 2.43 eV for 10 wt% Ru/TiO_2-PC500 prepared by the solvothermal, reflux, and incipient wetness impregnation methods, respectively. These values are concordant with the ones present in the literature[83]. Typically, lower bandgap energy indicates higher photoactivity in the catalyst, as it facilitates the promotion of electrons to the conduction band with less energy[90]. It should be noted, however, that factors such as metal dispersion and particle size also influence the overall photoactivity of the catalyst. The disparity in bandgap energy observed among the catalysts prepared using different methods can be attributed to the variation in the ruthenium content within each material. The incipient wetness impregnation method, which is expected to yield the highest ruthenium content, resulted in a catalyst with the smallest bandgap energy. On the other hand, the solvothermal synthesis method, which produced the catalyst with the lowest mass fraction of ruthenium, exhibited the highest bandgap energy. This correlation suggests that the bandgap energy of the catalyst is influenced by the amount of ruthenium present in the material. The impact of ruthenium on the bandgap energy will be further discussed in the following sub-section.

The catalysts impregnated with ruthenium exhibit significantly higher conversions than those impregnated with nickel. However, the notable disparity observed in the performance of ruthenium catalysts under different preparation methods, coupled with the results reported in the literature for nickel catalysts, suggests that the preparation method plays a crucial role in

the catalyst performance. Thus, it is essential to further identify a more suitable method for preparing Ni/TiO_2 catalysts.

Nevertheless, ruthenium consistently demonstrated superior performance compared to nickel, establishing it as the preferred choice for producing highly active catalysts for the CO_2 photo-thermal methanation. Solvothermal impregnation is the most viable option to synthesise highly active Ru/TiO_2 catalysts for the photo-thermal CO_2 hydrogenation. Despite presenting the smallest quantity and efficiency on impregnation ruthenium, the catalyst prepared by solvothermal synthesis demonstrated high superficial area and notable reactivity improvements compared to the one synthesised by the reflux method. This way, this method was selected for further tests.

4.1.4 Ruthenium content

As observed before, the impregnation of Ru onto PC500 TiO_2 through the solvothermal method appears to be the optimal approach for developing high-performance catalysts towards CO_2 photo-thermal hydrogenation. Building upon this observation, a series of Ru/TiO_2 catalysts with varying Ru contents were prepared using solvothermal synthesis: 5, 7.5, 10, 12.5, and 20 wt%. By maintaining consistent experimental conditions, the performance of these catalysts was assessed by analysing the CO_2 conversion, which can be compared in Figure 17.

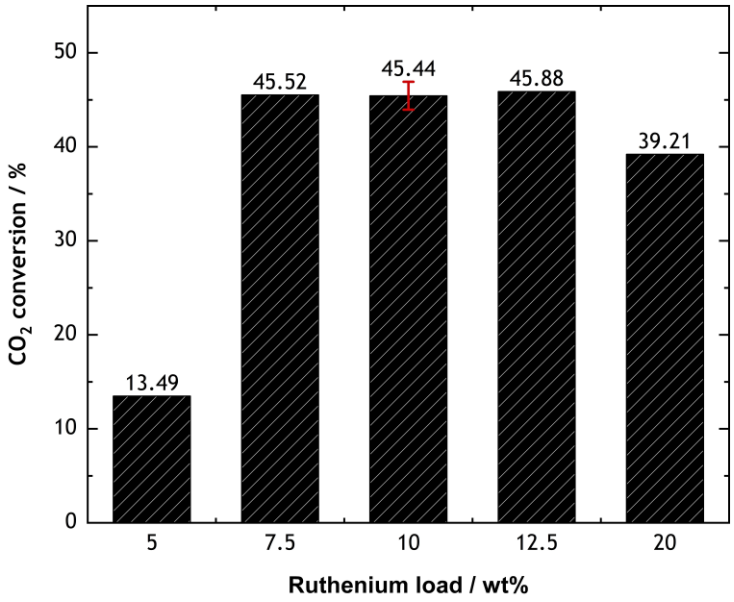

Figure 17: CO_2 conversions achieved after 1-hour solar irradiation at 130 ºC as a function of Ru content in the Ru/TiO_2-PC500 catalyst prepared via solvothermal synthesis.

As observed, the mass fraction of ruthenium is a critical parameter that requires optimisation as it significantly influences the catalyst's efficiency. A slight increase in Ru content from 5 wt% to 7.5 wt% can result in a 3.4-fold increase in CO_2 conversion. This parameter is particularly important since altering the impregnated Ru amount also affects its dispersion. Increasing the

Ru content may lead to poorer dispersions and larger particle sizes, consequently diminishing the catalyst's activity. While larger particles generate more hot charge carriers, their energy levels are lower than those of smaller particles, ultimately reducing the photocatalytic activity since these particles cannot overcome the Schottky barriers and be transferred to the accepter[78]. This observation could elucidate the inhibitory effect observed when increasing the Ru mass fraction from 12.5 % to 20 %, which reduced the obtained CO_2 conversion by 6.7 %.

It is also evident that, while increasing the Ru mass fraction appears to be beneficial within the range of 5 to 7.5 % and detrimental beyond 12.5 %, no discernible influence, either positive or negative, is observed when incrementing the Ru load from 7.5 to 10 or 12.5 wt%.

It is worth mentioning that the synthesis of 20 wt% Ru/TiO_2 resulted in the formation of solid agglomerated particles upon removal from the autoclave, unlike any other catalyst synthesised using the solvothermal method, that produced homogeneous solutions. This observation could be attributed to either an insufficient volume of ethylene glycol to impregnate all the added ruthenium or the saturation of titanium dioxide.

H_2-TPR tests were performed to evaluate how the Ru amount affects the reactivity of the Ru/TiO_2 catalysts. Figure 18 compiles the main results.

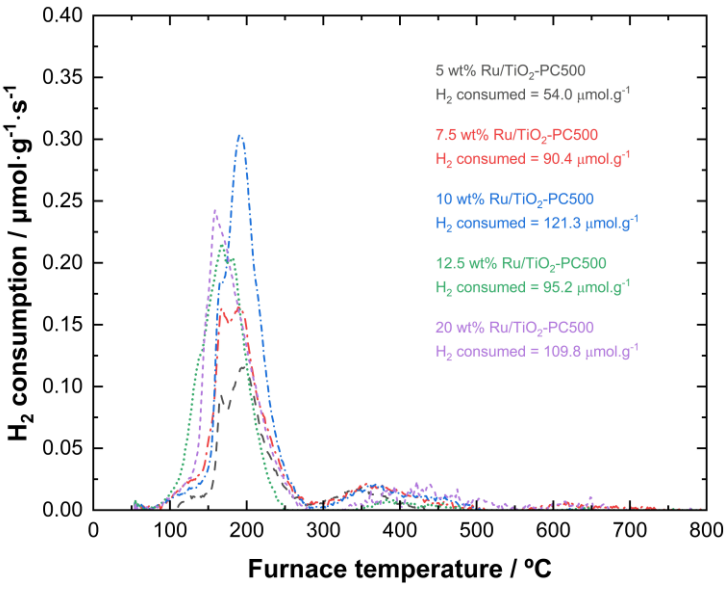

Figure 18: H_2-TPR profiles for Ru/TiO_2-PC500 catalysts with different Ru loads: 5 (dark grey dots), 7.5 (red dash-dot line), 10 (blue dash-dot line),12.5 (green dots-line) and 20 (violet dash-line) wt%, prepared by solvothermal impregnation.

The introduction of Ru enhances the overall catalyst reactivity (about 67 % from 5 to 7.5 wt%). However, when the Ru mass fraction exceeds 7.5 wt%, its impact on reactivity becomes less pronounced (about 34 % from 7.5 to 10 wt%), as evidenced by the relative stabilisation of H_2 consumption for further mass fractions. This finding aligns with the earlier results of CO_2

conversion (Figure 17). It is noteworthy that catalysts with 12.5 % and 20 % mass fractions exhibited a slight leftward shift in the maximum H_2 consumption, indicating potentially higher reactivity at slightly lower temperatures. Ru/TiO_2 catalysts with mass fractions below 12.5 % exhibit a maximum H_2 consumption peak at 190 ºC, along with a smaller peak at 165 ºC. In contrast, catalysts containing 12.5 and 20 wt% Ru/TiO_2 demonstrate a maximum peak at 160 ºC. Nevertheless, this observation did not significantly affect the catalyst's performance in CO_2 photo-thermal hydrogenation at 130 ºC.

The light absorption spectrum of Ru/TiO_2 prepared with different Ru mass fractions, synthesised using the solvothermal method, was analysed using UV-Vis spectroscopy, as represented in Figure 19a). Figure 19b) represents the Tauc plot for the same materials to determine the catalysts' optical bandgap energy.

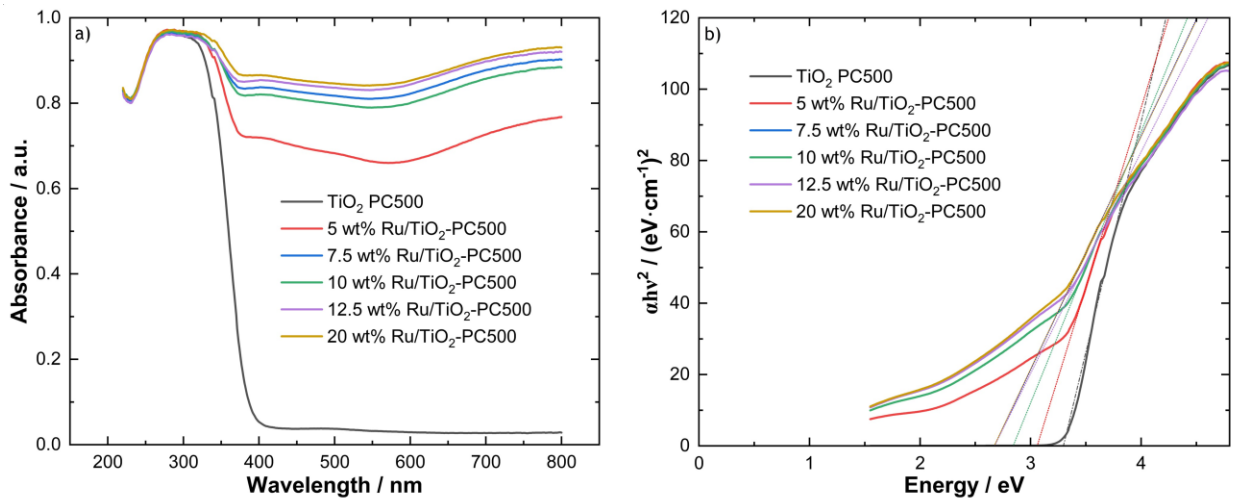

Figure 19: (a) UV-visible absorption spectra and b) Tauc plot for pristine TiO_2-PC500 and Ru/TiO_2-PC500 catalysts composed of different Ru contents: 5, 7.5, 10, 12.5 and 20 wt%, prepared by solvothermal impregnation.

The Ru addition to TiO_2 exhibits a noticeable impact, as demonstrated in Figure 19a) by the significant increase in material absorbance for wavelengths above 330 nm, particularly in the range of wavelengths exceeding 400 nm. In fact, pure TiO_2 shows nearly negligible absorbance in this region, while the Ru-based materials can reach absorbance values close to 1. This observation highlights the antenna effect characteristic of plasmonic materials, enabling radiation absorption in the visible and near-infrared regions and enhancing photonic efficiency. This phenomenon is further supported by the determination of the E_g for each material, which are 3.29 eV for TiO_2, 3.12 eV for 5 wt% Ru/TiO_2, 2.64 eV for 7.5 wt% Ru/TiO_2, 2.82 eV for 10 wt% Ru/TiO_2, 2.65 eV for 12.5 wt% Ru/TiO_2, and 2.67 eV for 20 wt% Ru/TiO_2. The Ru incorporation reduces the catalyst bandgap energy, enabling it to absorb more photons that can be part of the photocatalytic effect. However, it can be concluded that while 5 wt% does not appear sufficient to fully exploit the potential of Ru impregnation on TiO_2, surpassing

7.5 wt% does not seem to widen the bandgap further. This finding aligns with the CO_2 conversion results presented in Figure 17.

The activity of the catalyst is notably influenced by the ruthenium content, either due to variations in the availability of ruthenium for the reaction or alterations in the morphology, size, and dispersion of ruthenium on the titanium dioxide. Nevertheless, the experimental data demonstrates that the catalyst's performance reaches a plateau regarding CO_2 conversion after attaining a mass fraction of 7.5 wt% ruthenium. Beyond this threshold, further increments in the ruthenium content do not yield any additional enhancement in CO_2 conversion. Considering the considerably higher cost of ruthenium compared to titanium dioxide, minimizing its usage is imperative. Therefore, a 7.5 wt% Ru/TiO_2 prepared via the solvothermal method employing PC500 titanium dioxide was identified as the best catalyst and subsequently selected for subsequent investigations.

However, it is crucial to conduct additional analysis to accurately determine the amount of impregnated ruthenium. This is supported by the XPS analysis, which revealed that the catalyst labeled as 10 wt% Ru/TiO_2, prepared via solvothermal impregnation, exhibited a measured superficial mass fraction of only 6.22 %, and the one prepared by reflux impregnation only possessed a superficial mass fraction of 8.45 %.

4.2 Influence of the operating conditions

4.2.1 Solar irradiation

Atlas Suntest XLS^+ solar simulator typically possesses a blue-coated IR radiation (cut-off at 800 nm) filter that blocks almost all IR radiation emitted by the Xe lamp (280-3000 nm). To evaluate the impact of the radiation type reaching the reactor, the filter was intentionally removed, and a comparative analysis was conducted between the CO_2 conversion achieved under UV-Vis (with IR filter) and UV-Vis-NIR (without IR filter). The results of this investigation are presented in Figure 20.

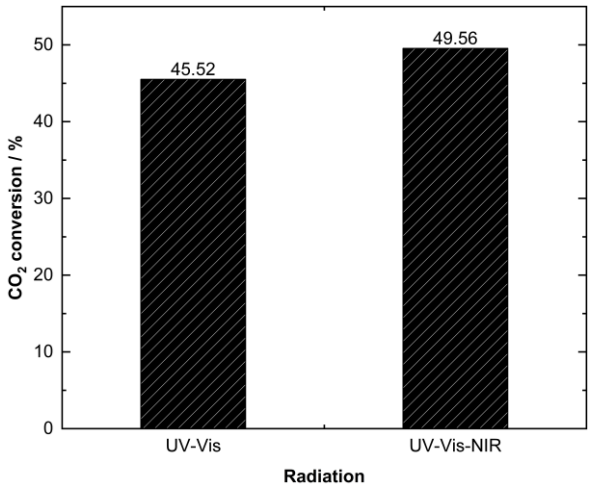

Figure 20: CO_2 conversions achieved after 1 hour of UV-Vis and UV-Vis-IR solar irradiation at 130 ºC, using the 7.5 wt% Ru/TiO_2-PC500 catalyst prepared via solvothermal synthesis.

Consistent with expectations, removing the filter resulted in a slight increase in CO_2 conversion of about 4 %. This phenomenon can be attributed to the introduction of additional NIR photons into the reactional medium that can be absorbed by the Ru/TiO_2 catalyst, owing to the Ru presence, and that are now available to participate in the photo and photo-thermal catalytic processes, as they are no longer impeded by the filter's obstruction. This is substantiated by the observed absorption of radiation in the visible and near-infrared regions, as depicted in the UV-Vis plots analysed previously. These plots clearly demonstrate the absorption of this radiation following the impregnation of ruthenium. The 7.5 wt% Ru/TiO_2 catalyst has a bandgap energy of 2.64 eV, resulting in electron excitation for radiation with wavelengths lower than 464 nm, which falls within the blue light range of the visible spectrum. Although the added NIR photons lack sufficient energy to excite electrons to the valence band and participate directly in the photocatalytic mechanism, the verified increase in CO_2 conversion with the introduction of these photons can be explained by their ability to enhance the photo-induced thermal effect within the active sites, contributing to improved catalytic activity.

With this knowledge, subsequent tests were conducted without the use of the filter.

4.2.2 Reaction temperature and the synergistic effect of photo and thermal catalysis

The thermal effect plays a crucial role in photo-thermal catalysis. In this context, experiments were conducted to assess the temperature-dependence dynamics. Moreover, the examination of the synergistic effect arising from the combination of photo and thermal catalysis was achieved by conducting tests under various conditions, including the presence or absence of simulated sunlight or external heating.

In this way, the performance of 7.5 wt% Ru/TiO_2-PC500 prepared via solvothermal impregnation was assessed at 100, 130, and 160 ºC with (photo-thermal catalysis with assisted heating) and

without (thermal catalysis) solar radiation. Furthermore, a methanation reaction under simulated sunlight with no external heating (photothermal catalysis with self-heating) was carried out. Figure 21 compiles the main results. Due to experimental limitations, the reactions conducted at a temperature of 160 ºC were terminated prematurely at 15 minutes, in contrast to the remaining reactions that were allowed to proceed for 60 minutes.

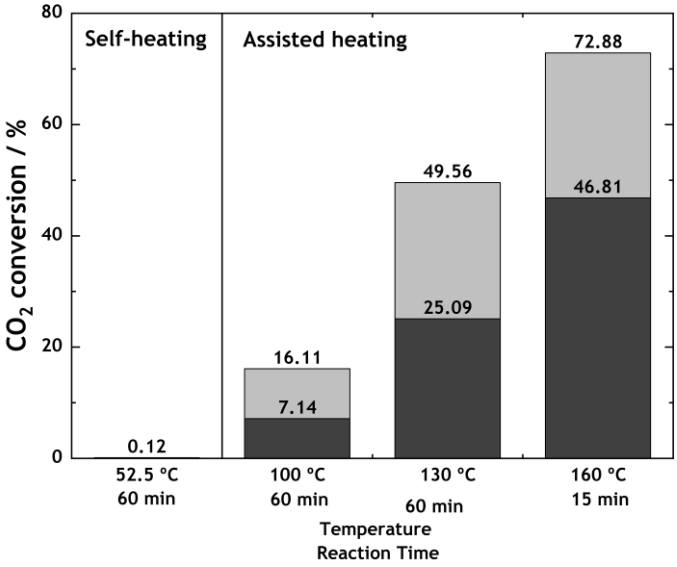

Figure 21: CO_2 conversion as a function of temperature using the 7.5 wt% Ru/TiO_2-PC500 catalyst, (i) (■, photothermal catalysis with self-heating up to 52.5 ºC) - without external heating under solar irradiation, (ii) (■, photo-thermal catalysis with assisted-heating) - with external heating under solar irradiation, and (iii) (■, thermal catalysis) - with external heating under dark conditions.

The catalyst's activity improvement becomes evident when temperature increases, even when analysing pure thermal systems. For the assisted-heated photo-thermal system, a temperature increase of 30 ºC, from 100 to 130 ºC, results in a threefold increase in CO_2 conversion. Moreover, a further increment in the temperature by an additional 30 ºC, from 130 to 160 ºC, led to a CO_2 conversion enhancement by a factor of 1.9 in only a quarter of the time.

The performance of the photothermocatalytic system, operating without external heating, exhibited significantly inferior results compared to the systems incorporating external heating. Nevertheless, it is worth noting that while the average temperature within the reactor reached 52.5 ºC, the catalyst surface reached a higher temperature of 73 ºC, indicating the presence of the plasmonic effect. However, this temperature alone proved insufficient to activate the catalyst and facilitate a substantial CO_2 conversion. This observation is supported by the relatively low conversion achieved at a temperature of 100 ºC with external heating, which shows that temperature plays a crucial role in photo-thermal catalysis.

Despite the underwhelming performance of the photothermocatalytic system in the absence of external heating, its impact becomes remarkable when combined with thermal catalysis. By employing external heating and simulated sunlight, the results attained considerably surpass those obtained solely through thermal catalysis. Consequently, it becomes possible to significantly lower the temperature required for the methanation reaction while maintaining the catalyst's performance. These outcomes can be attributed to the well-established synergistic effect arising from the combination of photo and thermal catalysis, resulting in enhanced photo-thermal catalysis.

Due to the outstanding result achieved at 160 ºC and since this value coincides with the temperature of the first peak of H_2 consumption at the H_2-TPR test, as shown in Figure 18, further photo-thermal CO_2 reduction reactions were performed at this temperature.

4.2.3 Reaction time and catalyst reuse

To deepen the knowledge of the photo-thermal methanation kinetic behaviour and catalyst reusability, the CO_2 conversion was measured at 160 ºC after 3,6,9,12 and 15 minutes in sequential cycles (following a time ascending order) using the same 7.5 % Ru/TiO_2-PC500 catalyst (100 mg) prepared via solvothermal synthesis, as presented in Figure 22a). It should be noted that before this set of tests, an initial 15-minute reaction was conducted and compared with the last 15-minute cycle to assess if the catalyst had lost its activity. No significant reduction in conversion was observed, with only a slight variation in CO_2 conversion from 78.9 % to 76.7 %, indicating that this material remained stable after the performed tests.

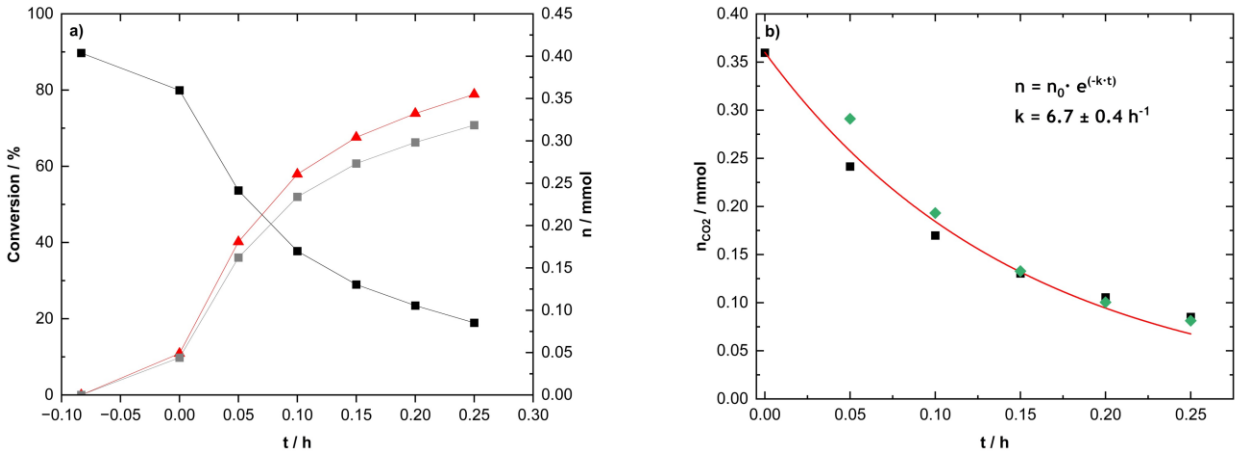

Figure 22: a) Evolution of the CO_2 conversion (▲) and moles number of CO_2 (■) and CH_4 (■)as a function of reaction time at 160 ºC under solar irradiation, using 100 mg of 7.5 wt% Ru/TiO_2-PC500 catalyst and b) adjustment (red line) of the experimental data (■) to a pseudo-first-order reaction model with adjusted n_{CO2} to the model (◆).

In the present system, negative time denotes the period during which the temperature was being stabilised, and no radiation was employed. Time *t* = 0 represents the moment when the

lamp was activated. By fitting a non-linear model to the number of moles of CO_2 over time data for $t \geq 0$, it is possible to establish a pseudo-first-order reaction's kinetic constant of 6.7 h^{-1}, as illustrated in Figure 22b), which presents the variation of the number of moles of CO_2, the non-linear adjusted model and the predicted number of moles of CO_2 over time using the predicted kinetic constant.

Nonetheless, the reaction's kinetic constant is not a regularly determined parameter in the literature. The most common parameter to compare results is the maximum $Y_{r,CH4}$. Employing Equation 4 at discrete time intervals, which quantifies the change in the quantity of CO_2 or CH_4 moles per time step (t_i) from the reaction's initiation (t_0) and dividing it by the catalyst's mass (m_{cat}), diverse values for this parameter can be ascertained, considering the reaction's absolute selectivity toward CH_4, which is 100 %. Figure 23 presents the obtained values using 100 mg of the best catalyst at 160 ºC for each evaluated time.

$$Y_{r,CH4} = -1 \times \frac{n_{CO2_i} - n_{CO2_{t=0}}}{(t_i - t_0) \cdot m_{cat}} = \frac{n_{CH4_i} - n_{CH4_{t=0}}}{(t_i - t_0) \cdot m_{cat}} \quad \text{(Eq.4)}$$

As a result, a notable maximum $Y_{r,CH4}$ of 23.44 mmol·g^{-1}·h^{-1} is attained after 3 minutes at this temperature. This outcome surpasses the values reported in the literature for similar temperatures when considering simple plasmonic/semiconductor structures. However, performing comprehensive comparisons is challenging due to the absence of standardisation regarding the light irradiation source and the distance from the light source, among other factors.

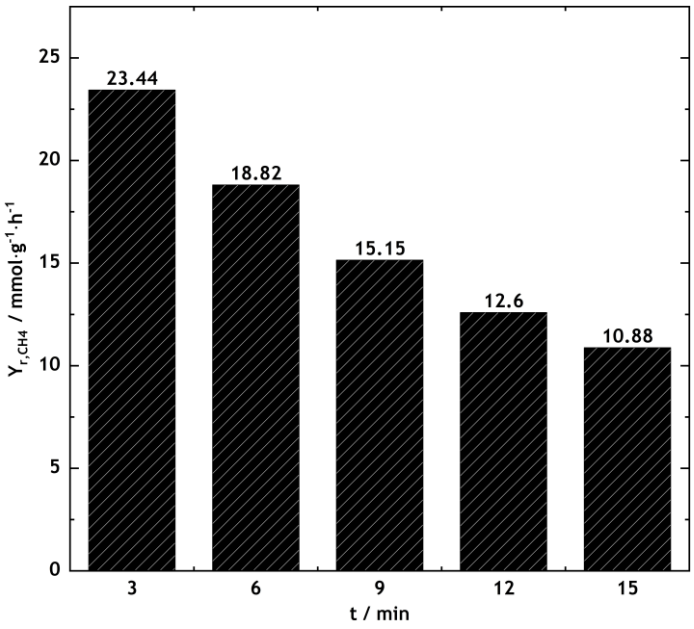

Figure 23: Yield rate for CH_4 generation along a 15-minute reaction employing 100 mg of 7.5 wt% Ru/TiO_2–PC500 at 160 ºC under solar irradiation.

Table 1 provides a compilation of relevant studies from the literature, showcasing key experimental conditions, catalysts employed, and the maximum $Y_{r,CH4}$. Remarkably, this work achieves a similar result as the 2.5 wt% Ru/TiO_2 catalyst but at a significantly lower temperature, reducing it from 325 ºC to 160 ºC. In comparison to results obtained with similar materials, this study exhibited the second-highest result among the selected literature. However, it is important to note that the highest result reported in the selected literature was achieved under high irradiation (14.5 suns) and high temperatures (300 ºC). In contrast, when the same material was evaluated under conditions similar to those used in this project, the maximum $Y_{r,CH4}$ was found to be 13.6 times lower.

The approach developed in the current work offers promising potential as a catalyst for effectively reducing the energy requirements for the CO_2 hydrogenation reaction, thereby reducing the reliance on high temperatures by leveraging the considerable synergistic effect of photo and thermal catalysis.

5 Conclusion

Climate change is a pressing global issue caused by human-induced greenhouse gas emissions. As the world's energy needs continue to rise, it is crucial to explore strategies for reducing, capturing, and utilising CO_2 emissions. CO_2 hydrogenation has emerged as a promising approach to mitigate emissions and produce valuable energy carriers such as methane. However, conventional CO_2 hydrogenation requires high temperatures. To address this issue, photo-thermal catalysis has emerged as a promising alternative, harnessing the synergistic effects of photo and thermal catalysis to lower the required temperature. This research project aimed to develop a highly active catalyst for photo-thermal CO_2 methanation. Several key parameters were investigated, including the use of nickel (Ni) as an alternative to the commonly used ruthenium (Ru), the exploration of different forms of TiO_2 as the supporting semiconductor, the determination of the optimal mass fraction of plasmonic material in the catalyst and the development of a suitable impregnation method.

The investigation revealed that Ni-based catalysts exhibited low CO_2 conversion into methane, primarily attributed to the catalyst preparation method, which requires further optimisation. As a result, Ru was selected as the preferred plasmonic material for developing a highly active catalyst. Among different TiO_2 forms, PC500 TiO_2 demonstrated superior activity, attributed to its exceptional surface area compared to anatase or black P25 forms. Furthermore, the Ru mass fraction on TiO_2 significantly impacted catalyst performance, with increasing Ru content leading to enhanced CO_2 conversion. However, beyond a certain threshold, excessive ruthenium loading hindered the photo-thermocatalytic activity and diminished catalyst performance.

Consequently, a 7.5 wt% Ru/TiO_2 catalyst prepared with PC500 TiO_2 via solvothermal synthesis exhibited an outstanding performance for CO_2 photo-thermal hydrogenation achieving a notable maximum $Y_{r,CH4}$ of 23.44 $mmol \cdot g^{-1} \cdot h^{-1}$ at 160 °C under solar irradiation. The catalyst demonstrated a strong synergistic effect between photo and thermal catalysis. Even for higher temperatures, the CO_2 conversion remained significantly higher than the cumulative conversion achieved through separate thermal and photocatalysis. This finding emphasises the potential for temperature reduction while maintaining catalytic activity. Besides, the photo-thermocatalytic activity remained high after six successive utilisation cycles.

In summary, this research successfully developed a highly active catalyst for CO_2 photo-thermal methanation. By optimising key parameters and employing solvothermal synthesis with PC500 TiO_2, the catalyst demonstrated exceptional performance in terms of CO_2 conversion to methane at relatively low temperatures.

6 Assessment of the work done

6.1 Objectives Achieved

The main objective of this project was to synthesise, test and characterise a highly active photo-thermal catalyst for CO_2 hydrogenation. All these objectives were fulfilled. A 7.5 wt% Ru/TiO_2 prepared via solvothermal synthesis with PC500 TiO_2 was developed, achieving an outstanding maximum $Y_{r,CH4}$ of 23.44 $mmol \cdot g^{-1} \cdot h^{-1}$. To achieve this result, different preparation methods were studied (incipient wetness impregnation, wet impregnation, reflux impregnation, and solvothermal synthesis). Beyond that, the use of different plasmonic materials (ruthenium and nickel) was studied, along with the impact of the use of PC500, anatase, or black TiO_2 and the importance of the composition of the catalyst. The impact of these parameters was confirmed by the characterisation of some catalysts by H_2-Temperature programmed reduction, N_2 adsorption at -196 ºC, X-ray photoelectron spectroscopy, and UV-Vis spectroscopy. All the developed catalysts were tested in batch experiments to assess their performance on CO_2 hydrogenation.

6.2 Other Work Carried Out

The author was responsible for the adjustment of an existing experimental setup to perform the reaction tests, the development and calibration of a gas-chromatography method to measure the gas composition inside the reactor, programming a LabView program to collect and record data on the reaction medium's temperature and prepare and select the necessary equipment for future experiments in a continuous-flow reactor and improvements to the batch experiments setup.

Lastly, to determine the accurate mass fraction of ruthenium using the different preparation methods and after impregnating different amounts of ruthenium, an inductively coupled plasma optical emission spectroscopy (ICP-OES) analysis was performed. However, due to the lack of microwave equipment to extract the ruthenium from the catalyst samples, the samples were digested according to the following experimental procedure: for sample preparation, 20 mg of each material was digested in a 12 mL solution of HCl and HNO_3 (3:1 volume ratio) for 3 h at 150 ºC. The resulting solution was transferred to a 50 mL volumetric flask and topped up with distilled water. After filtration to remove any remaining solids, 1 mL of the solution was extracted and diluted 100 times to a final volume of 100 mL using a volumetric flask and distilled water. However, after ICP analysis, it was concluded that this method was not suitable for efficiently extract all the ruthenium present in the catalyst particles.

6.3 Suggestions for future work

In terms of catalyst performance testing, the current experimental setup presents limitations for the analysis of low-pressure conditions (≤ 1.2 bar) that typically happen due to the significant formation of condensed water for high CO_2 conversions and low temperatures, leading to a rapid decrease in pressure. This impedes the study of the catalyst for extended reaction times/higher conversions. To address this issue, adding an inert gas such as N_2, He, or Ar is proposed as a viable solution to maintain a relatively constant pressure within the system. Since the inert gas is not involved in the conversion reaction and remains unchanged, it can be used to increase the pressure in the reactor permanently. This approach has been widely adopted by researchers in the field.

In terms of catalyst development, the best method is well-identified. However, an ICP analysis is crucial to correctly evaluate the amount of ruthenium that is effectively impregnated to evaluate the need to improve, or not, the impregnation efficiency. That information would also help to understand the results in chapter 3.1.4 better. A TEM and H_2 chemisorption analysis would also be important to properly evaluate the particle size and metallic dispersion. The solvothermal methods, although producing notable results, can be optimised. Varying the time of the solution on the autoclave, the use of a single step on the sonicator, increasing or decreasing the temperature, and time on the calcination step, among others, are just some of the parameters that can be changed and studied to develop a better and more efficient process. Beyond that, the catalyst can still be further developed by adding other materials like carbon materials, zeolites, MOFs, LDHs, and perovskites, among others.

Lastly, a detailed kinetic study of the catalyst's performance under these and other temperatures and evaluating the impact of the irradiation intensity (that can be changed on the Suntest equipment) is essential for a better understanding of the catalyst performance.

6.4 Final Assessment

This work presented itself as a difficult task due to its exploratory nature. Developing a suitable method for preparing a highly active photo-thermal catalyst was challenging. Moreover, it required learning and understanding new concepts related to photocatalysts, as these topics were not covered in the previous years of education, which required extensive self-learning. However, despite all the difficulties, I achieved a good result by participating in this project. On a final note, I enjoyed working on this topic because it allowed me to develop solutions in such an important and relevant field as decarbonisation and synthetic fuel production. Furthermore, I learned a lot from this project, both in completely new fields and in gaining a better understanding of the ones I already knew.

7 References

(1) Huaman, R.; Xiu Jun, T. Energy related CO_2 emissions and the progress on CCS projects: A review. Renewable and Sustainable Energy Reviews **2014**, 31, 368-385. DOI: https://doi.org/10.1016/j.rser.2013.12.002.

(2) Salvi, D. B. L.; Jindal, S. Recent developments and challenges ahead in carbon capture and sequestration technologies. SN Applied Sciences **2019**, 1. DOI: 10.1007/s42452-019-0909-2.

(3) UnitedNations. Global Issues: Climate Change. United Nations, 2022. United Nations (accessed 2023 09/02/2023).

(4) Gulev,S.; Ahn, J.; Dentener, F.; Domingues, C.; Gerland, S.; Gong, D.; Kaufman, D.; Nnamchi, D.; Quaas, J.; Rivera, J.; Sathyendranath, S.; Smith, S.; Trewin, B.; Schuckmann, K.; Vose, R. Climate Change 2021: The Physical Science Basis. Contribution of Working Group I to the Sixth Assessment Report of the Intergovernmental Panel on Climate Change; Cambridge University Press, 2021.

(5) Oemar, U.; Hidajat, K.; Kawi, S. High catalytic stability of Pd-Ni/Y_2O_3 formed by interfacial Cl for oxy-CO_2 reforming of CH_4. Catalysis Today **2017**, 281, 276-294. DOI: https://doi.org/10.1016/j.cattod.2016.07.019.

(6) Kathiraser, Y.; Wang, Z.; Ang, M. L.; Mo, L.; Li, Z.; Oemar, U.; Kawi, S. Highly active and coke resistant Ni/SiO2 catalysts for oxidative reforming of model biogas: Effect of low ceria loading. Journal of CO_2 Utilization **2017**, 19, 284-295. DOI: https://doi.org/10.1016/j.jcou.2017.03.018.

(7) Das, S.; Jangam, A.; Du, Y.; Hidajat, K.; Kawi, S. Highly dispersed nickel catalysts via a facile pyrolysis generated protective carbon layer. Chemical Communications **2019**, 55 (43), 6074-6077, 10.1039/C9CC00783K. DOI: 10.1039/C9CC00783K.

(8) Saeidi, S.; Amin, N. A. S.; Rahimpour, M. R. Hydrogenation of CO_2 to value-added products—A review and potential future developments. Journal of CO_2 Utilization **2014**, 5, 66-81. DOI: https://doi.org/10.1016/j.jcou.2013.12.005.

(9) Saeidi, S.; Najari, S.; Fazlollahi, F.; Nikoo, M. K.; Sefidkon, F.; Klemeš, J. J.; Baxter, L. L. Mechanisms and kinetics of CO_2 hydrogenation to value-added products: A detailed review on current status and future trends. Renewable and Sustainable Energy Reviews **2017**, 80, 1292-1311. DOI: https://doi.org/10.1016/j.rser.2017.05.204.

(10) Li, X.; Yu, J.; Jaroniec, M.; Chen, X. Cocatalysts for Selective Photoreduction of CO_2 into Solar Fuels. Chemical Reviews **2019**, 119 (6), 3962-4179. DOI: 10.1021/acs.chemrev.8b00400.

(11) Tu, W.; Zhou, Y.; Zou, Z. Photocatalytic Conversion of CO_2 into Renewable Hydrocarbon Fuels: State-of-the-Art Accomplishment, Challenges, and Prospects. Advanced Materials **2014**, 26 (27), 4607-4626. DOI: https://doi.org/10.1002/adma.201400087.

(12) Yuan, L.; Hung, S.-F.; Tang, Z.-R.; Chen, H. M.; Xiong, Y.; Xu, Y.-J. Dynamic Evolution of Atomically Dispersed Cu Species for CO_2 Photoreduction to Solar Fuels. ACS Catalysis **2019**, 9 (6), 4824-4833. DOI: 10.1021/acscatal.9b00862.

(13) Chen, S.; Takata, T.; Domen, K. Particulate photocatalysts for overall water splitting. Nature Reviews Materials **2017**, 2 (10), 17050. DOI: 10.1038/natrevmats.2017.50.

(14) Schlögl, R. The Role of Chemistry in the Energy Challenge. ChemSusChem **2010**, 3 (2), 209-222. DOI: https://doi.org/10.1002/cssc.200900183.

(15) Zhao, Y.; Gao, W.; Li, S.; Williams, G. R.; Mahadi, A. H.; Ma, D. Solar- versus Thermal-Driven Catalysis for Energy Conversion. Joule **2019**, 3 (4), 920-937. DOI: https://doi.org/10.1016/j.joule.2019.03.003.

(16) Li, S.; Liu, J.; Yin, Z.; Ren, P.; Lin, L.; Gong, Y.; Yang, C.; Zheng, X.; Cao, R.; Yao, S.; et al. Impact of the Coordination Environment on Atomically Dispersed Pt Catalysts for Oxygen Reduction Reaction. ACS Catalysis **2020**, 10 (1), 907-913. DOI: 10.1021/acscatal.9b04558.

(17) Wu, C.; Lin, L.; Liu, J.; Zhang, J.; Zhang, F.; Zhou, T.; Rui, N.; Yao, S.; Deng, Y.; Yang, F.; et al. Inverse ZrO_2/Cu as a highly efficient methanol synthesis catalyst from CO_2 hydrogenation. Nature Communications **2020**, 11 (1), 5767. DOI: 10.1038/s41467-020-19634-8.

(18) Hashimoto, K.; Irie, H.; Fujishima, A. TiO_2 Photocatalysis: A Historical Overview and Future Prospects. Japanese Journal of Applied Physics **2005**, 44 (12R), 8269. DOI: 10.1143/JJAP.44.8269.

(19) Kumar, S. G.; Devi, L. G. Review on Modified TiO_2 Photocatalysis under UV/Visible Light: Selected Results and Related Mechanisms on Interfacial Charge Carrier Transfer Dynamics. The Journal of Physical Chemistry A **2011**, 115 (46), 13211-13241. DOI: 10.1021/jp204364a.

(20) Keller, N.; Ivanez, J.; Highfield, J.; Ruppert, A. M. Photo-/thermal synergies in heterogeneous catalysis: Towards low-temperature (solar-driven) processing for sustainable energy and chemicals. Applied Catalysis B: Environmental **2021**, 296, 120320. DOI: https://doi.org/10.1016/j.apcatb.2021.120320.

(21) Li, J.; Wu, N. Semiconductor-based photocatalysts and photoelectrochemical cells for solar fuel generation: a review. Catalysis Science & Technology **2015**, 5 (3), 1360-1384, 10.1039/C4CY00974F. DOI: 10.1039/C4CY00974F.

(22) Wang, F.; Huang, Y.; Chai, Z.; Zeng, M.; Li, Q.; Wang, Y.; Xu, D. Photothermal-enhanced catalysis in core–shell plasmonic hierarchical Cu_7S_4 microsphere@zeolitic imidazole framework-8. Chemical Science **2016**, 7 (12), 6887-6893, 10.1039/C6SC03239G. DOI: 10.1039/C6SC03239G.

(23) Zhang, W.; Wang, L.; Wang, K.; Khan, M. U.; Wang, M.; Li, H.; Zeng, J. Integration of Photothermal Effect and Heat Insulation to Efficiently Reduce Reaction Temperature of CO_2 Hydrogenation. Small **2017**, 13 (7), 1602583. DOI: https://doi.org/10.1002/smll.201602583.

(24) Ameta, R.; Solanki, M. S.; Benjamin, S.; Ameta, S. C. Chapter 6 - Photocatalysis. In Advanced Oxidation Processes for Waste Water Treatment, Ameta, S. C., Ameta, R. Eds.; Academic Press, 2018; pp 135-175.

(25) Wu, N. Plasmonic metal–semiconductor photocatalysts and photoelectrochemical cells: a review. Nanoscale **2018**, 10 (6), 2679-2696, 10.1039/C7NR08487K. DOI: 10.1039/C7NR08487K.

(26) Fujishima, A.; Honda, K. Electrochemical Photolysis of Water at a Semiconductor Electrode. Nature **1972**, 238 (5358), 37-38. DOI: 10.1038/238037a0.

(27) Paik, T.; Cargnello, M.; Gordon, T. R.; Zhang, S.; Yun, H.; Lee, J. D.; Woo, H. Y.; Oh, S. J.; Kagan, C. R.; Fornasiero, P.; et al. Photocatalytic Hydrogen Evolution from Substoichiometric Colloidal WO_{3-x} Nanowires. ACS Energy Letters **2018**, 3 (8), 1904-1910. DOI: 10.1021/acsenergylett.8b00925.

(28) Xiao, C.; Wang, H.; Zhang, L.; Sun, S.; Wang, W. Enhanced Photocatalytic Nitrogen Fixation on MoO_2/BiOCl Composite. ChemCatChem **2019**, 11 (24), 6467-6472. DOI: https://doi.org/10.1002/cctc.201901635.

(29) Mateo, D.; Cerrillo, J. L.; Durini, S.; Gascon, J. Fundamentals and applications of photo-thermal catalysis. Chemical Society Reviews **2021**, 50 (3), 2173-2210, 10.1039/D0CS00357C. DOI: 10.1039/D0CS00357C.

(30) Brongersma, M. L.; Halas, N. J.; Nordlander, P. Plasmon-induced hot carrier science and technology. Nature Nanotechnology **2015**, 10 (1), 25-34. DOI: 10.1038/nnano.2014.311.

(31) Song, C.; Wang, Z.; Yin, Z.; Xiao, D.; Ma, D. Principles and applications of photothermal catalysis. Chem Catalysis **2022**, 2 (1), 52-83. DOI: https://doi.org/10.1016/j.checat.2021.10.005.

(32) Richardson, H. H.; Carlson, M. T.; Tandler, P. J.; Hernandez, P.; Govorov, A. O. Experimental and theoretical studies of light-to-heat conversion and collective heating effects in metal nanoparticle solutions. Nano Lett **2009**, 9 (3), 1139-1146. DOI: 10.1021/nl8036905 From NLM.

(33) Baffou, G.; Quidant, R. Thermo-plasmonics: using metallic nanostructures as nano-sources of heat. Laser & Photonics Reviews **2013**, 7 (2), 171-187. DOI: https://doi.org/10.1002/lpor.201200003.

(34) Manjavacas, A.; Liu, J. G.; Kulkarni, V.; Nordlander, P. Plasmon-Induced Hot Carriers in Metallic Nanoparticles. ACS Nano **2014**, 8 (8), 7630-7638. DOI: 10.1021/nn502445f.

(35) Zheng, B. Y.; Zhao, H.; Manjavacas, A.; McClain, M.; Nordlander, P.; Halas, N. J. Distinguishing between plasmon-induced and photoexcited carriers in a device geometry. Nature Communications **2015**, 6 (1), 7797. DOI: 10.1038/ncomms8797.

(36) Richardson, H. H.; Hickman, Z. N.; Govorov, A. O.; Thomas, A. C.; Zhang, W.; Kordesch, M. E. Thermooptical properties of gold nanoparticles embedded in ice: characterization of heat generation and melting. Nano Lett **2006**, 6 (4), 783-788. DOI: 10.1021/nl060105l From NLM.

(37) Meng, X.; Liu, L.; Ouyang, S.; Xu, H.; Wang, D.; Zhao, N.; Ye, J. Nanometals for Solar-to-Chemical Energy Conversion: From Semiconductor-Based Photocatalysis to Plasmon-Mediated Photocatalysis and Photo-Thermocatalysis. Advanced Materials **2016**, 28 (32), 6781-6803. DOI: https://doi.org/10.1002/adma.201600305.

(38) Mittal, D.; Ahlawat, M.; Govind Rao, V. Recent Progress and Challenges in Plasmon-Mediated Reduction of CO2 to Chemicals and Fuels. Advanced Materials Interfaces **2022**, 9 (12), 2102383. DOI: https://doi.org/10.1002/admi.202102383.

(39) Kale, M. J.; Avanesian, T.; Christopher, P. Direct Photocatalysis by Plasmonic Nanostructures. ACS Catalysis **2014**, 4 (1), 116-128. DOI: 10.1021/cs400993w.

(40) Christopher, P.; Xin, H.; Linic, S. Visible-light-enhanced catalytic oxidation reactions on plasmonic silver nanostructures. Nature Chemistry **2011**, 3 (6), 467-472. DOI: 10.1038/nchem.1032.

(41) Zhang, Y.; He, S.; Guo, W.; Hu, Y.; Huang, J.; Mulcahy, J. R.; Wei, W. D. Surface-Plasmon-Driven Hot Electron Photochemistry. Chemical Reviews **2018**, 118 (6), 2927-2954. DOI: 10.1021/acs.chemrev.7b00430.

(42) Hartland, G. V.; Besteiro, L. V.; Johns, P.; Govorov, A. O. What's so Hot about Electrons in Metal Nanoparticles? ACS Energy Letters **2017**, 2 (7), 1641-1653. DOI: 10.1021/acsenergylett.7b00333.

(43) Zhang, Y.; He, S.; Guo, W.; Hu, Y.; Huang, J.; Mulcahy, J.; Wei, W. Surface-Plasmon-Driven Hot Electron Photochemistry. Chemical Reviews **2017**, 118. DOI: 10.1021/acs.chemrev.7b00430.

(44) Christopher, P.; Moskovits, M. Hot Charge Carrier Transmission from Plasmonic Nanostructures. Annual Review of Physical Chemistry **2017**, 68 (1), 379-398. DOI: 10.1146/annurev-physchem-052516-044948.

(45) Boerigter, C.; Campana, R.; Morabito, M.; Linic, S. Evidence and implications of direct charge excitation as the dominant mechanism in plasmon-mediated photocatalysis. Nature Communications **2016**, 7 (1), 10545. DOI: 10.1038/ncomms10545.

(46) Mukherjee, S.; Libisch, F.; Large, N.; Neumann, O.; Brown, L. V.; Cheng, J.; Lassiter, J. B.; Carter, E. A.; Nordlander, P.; Halas, N. J. Hot Electrons Do the Impossible: Plasmon-Induced Dissociation of H2 on Au. Nano Letters **2013**, 13 (1), 240-247. DOI: 10.1021/nl303940z.

(47) Mukherjee, S.; Zhou, L.; Goodman, A. M.; Large, N.; Ayala-Orozco, C.; Zhang, Y.; Nordlander, P.; Halas, N. J. Hot-Electron-Induced Dissociation of H_2 on Gold Nanoparticles

Supported on SiO_2. Journal of the American Chemical Society **2014**, 136 (1), 64-67. DOI: 10.1021/ja411017b.

(48) Bauer, C.; Abid, J.-P.; Fermin, D.; Girault, H. H. Ultrafast chemical interface scattering as an additional decay channel for nascent nonthermal electrons in small metal nanoparticles. The Journal of Chemical Physics **2004**, 120 (19), 9302-9315. DOI: 10.1063/1.1710856.

(49) Boerigter, C.; Aslam, U.; Linic, S. Mechanism of Charge Transfer from Plasmonic Nanostructures to Chemically Attached Materials. ACS Nano **2016**, 10 (6), 6108-6115. DOI: 10.1021/acsnano.6b01846.

(50) Gellé, A.; Jin, T.; de la Garza, L.; Price, G. D.; Besteiro, L. V.; Moores, A. Applications of Plasmon-Enhanced Nanocatalysis to Organic Transformations. Chemical Reviews **2020**, 120 (2), 986-1041. DOI: 10.1021/acs.chemrev.9b00187.

(51) Foerster, B.; Joplin, A.; Kaefer, K.; Celiksoy, S.; Link, S.; Sönnichsen, C. Chemical Interface Damping Depends on Electrons Reaching the Surface. ACS Nano **2017**, 11 (3), 2886-2893. DOI: 10.1021/acsnano.6b08010.

(52) Wang, M.; Ye, M.; Iocozzia, J.; Lin, C.; Lin, Z. Plasmon-Mediated Solar Energy Conversion via Photocatalysis in Noble Metal/Semiconductor Composites. Advanced Science **2016**, 3 (6), 1600024. DOI: https://doi.org/10.1002/advs.201600024.

(53) Baldoví, H. G.; Neaţu, Ş.; Khan, A.; Asiri, A. M.; Kosa, S. A.; Garcia, H. Understanding the Origin of the Photocatalytic CO_2 Reduction by Au- and Cu-Loaded TiO_2: A Microsecond Transient Absorption Spectroscopy Study. The Journal of Physical Chemistry C **2015**, 119 (12), 6819-6827. DOI: 10.1021/jp5106136.

(54) DuChene, J. S.; Sweeny, B. C.; Johnston-Peck, A. C.; Su, D.; Stach, E. A.; Wei, W. D. Prolonged Hot Electron Dynamics in Plasmonic-Metal/Semiconductor Heterostructures with Implications for Solar Photocatalysis. Angewandte Chemie International Edition **2014**, 53 (30), 7887-7891. DOI: https://doi.org/10.1002/anie.201404259.

(55) Khan, M. R.; Chuan, T. W.; Yousuf, A.; Chowdhury, M. N. K.; Cheng, C. K. Schottky barrier and surface plasmonic resonance phenomena towards the photocatalytic reaction: study of their mechanisms to enhance photocatalytic activity. Catalysis Science & Technology **2015**, 5 (5), 2522-2531, 10.1039/C4CY01545B. DOI: 10.1039/C4CY01545B.

(56) Marchuk, K.; Willets, K. A. Localized surface plasmons and hot electrons. Chemical Physics **2014**, 445, 95-104. DOI: https://doi.org/10.1016/j.chemphys.2014.10.016.

(57) Furube, A.; Du, L.; Hara, K.; Katoh, R.; Tachiya, M. Ultrafast Plasmon-Induced Electron Transfer from Gold Nanodots into TiO_2 Nanoparticles. Journal of the American Chemical Society **2007**, 129 (48), 14852-14853. DOI: 10.1021/ja076134v.

(58) White, T. P.; Catchpole, K. R. Plasmon-enhanced internal photoemission for photovoltaics: Theoretical efficiency limits. Applied Physics Letters **2012**, 101 (7), 073905. DOI: 10.1063/1.4746425.

(59) Bigot, J. Y.; Halté, V.; Merle, J. C.; Daunois, A. Electron dynamics in metallic nanoparticles. Chemical Physics **2000**, 251 (1), 181-203. DOI: https://doi.org/10.1016/S0301-0104(99)00298-0.

(60) Wu, K.; Chen, J.; McBride, J. R.; Lian, T. CHARGE TRANSFER. Efficient hot-electron transfer by a plasmon-induced interfacial charge-transfer transition. Science **2015**, 349 (6248), 632-635. DOI: 10.1126/science.aac5443 From NLM.

(61) Watanabe, K.; Menzel, D.; Nilius, N.; Freund, H.-J. Photochemistry on Metal Nanoparticles. Chemical Reviews **2006**, 106 (10), 4301-4320. DOI: 10.1021/cr050167g.

(62) Yu, S.; Wilson, A. J.; Kumari, G.; Zhang, X.; Jain, P. K. Opportunities and Challenges of Solar-Energy-Driven Carbon Dioxide to Fuel Conversion with Plasmonic Catalysts. ACS Energy Letters **2017**, 2 (9), 2058-2070. DOI: 10.1021/acsenergylett.7b00640.

(63) Govorov, A. O.; Richardson, H. H. Generating heat with metal nanoparticles. Nano Today **2007**, 2 (1), 30-38. DOI: https://doi.org/10.1016/S1748-0132(07)70017-8.

(64) Govorov, A. O.; Zhang, W.; Skeini, T.; Richardson, H.; Lee, J.; Kotov, N. A. Gold nanoparticle ensembles as heaters and actuators: melting and collective plasmon resonances. Nanoscale Research Letters **2006**, 1 (1), 84. DOI: 10.1007/s11671-006-9015-7.

(65) Baffou, G.; Berto, P.; Bermúdez Ureña, E.; Quidant, R.; Monneret, S.; Polleux, J.; Rigneault, H. Photoinduced Heating of Nanoparticle Arrays. ACS Nano **2013**, 7 (8), 6478-6488. DOI: 10.1021/nn401924n.

(66) Adleman, J. R.; Boyd, D. A.; Goodwin, D. G.; Psaltis, D. Heterogenous Catalysis Mediated by Plasmon Heating. Nano Letters **2009**, 9 (12), 4417-4423. DOI: 10.1021/nl902711n.

(67) Yang, Q.; Xu, Q.; Yu, S.-H.; Jiang, H.-L. Pd Nanocubes@ZIF-8: Integration of Plasmon-Driven Photothermal Conversion with a Metal–Organic Framework for Efficient and Selective Catalysis. Angewandte Chemie International Edition **2016**, 55 (11), 3685-3689. DOI: https://doi.org/10.1002/anie.201510655.

(68) Zhang, F.; Li, Y.-H.; Qi, M.-Y.; Yamada, Y. M. A.; Anpo, M.; Tang, Z.-R.; Xu, Y.-J. Photothermal catalytic CO_2 reduction over nanomaterials. Chem Catalysis **2021**, 1 (2), 272-297. DOI: https://doi.org/10.1016/j.checat.2021.01.003.

(69) Barrio, J.; Mateo, D.; Albero, J.; García, H.; Shalom, M. A Heterogeneous Carbon Nitride–Nickel Photocatalyst for Efficient Low-Temperature CO_2 Methanation. Advanced Energy Materials **2019**, 9 (44), 1902738. DOI: https://doi.org/10.1002/aenm.201902738.

(70) Nguyen, V.-H.; Nguyen, B.-S.; Jin, Z.; Shokouhimehr, M.; Jang, H. W.; Hu, C.; Singh, P.; Raizada, P.; Peng, W.; Shiung Lam, S.; et al. Towards artificial photosynthesis: Sustainable hydrogen utilization for photocatalytic reduction of CO_2 to high-value renewable fuels. Chemical Engineering Journal **2020**, 402, 126184. DOI: https://doi.org/10.1016/j.cej.2020.126184.

(71) Ashok, J.; Pati, S.; Hongmanorom, P.; Tianxi, Z.; Junmei, C.; Kawi, S. A review of recent catalyst advances in CO_2 methanation processes. Catalysis Today **2020**, 356, 471-489. DOI: https://doi.org/10.1016/j.cattod.2020.07.023.

(72) He, Y.; Liu, S.; Fu, W.; Wang, C.; Mebrahtu, C.; Sun, R.; Zeng, F. Thermodynamic Analysis of CO_2 Hydrogenation to Higher Alcohols ($C_{2-4}OH$): Effects of Isomers and Methane. ACS Omega **2022**, 7 (19), 16502-16514. DOI: 10.1021/acsomega.2c00502.

(73) Meng, X.; Wang, T.; Liu, L.; Ouyang, S.; Li, P.; Hu, H.; Kako, T.; Iwai, H.; Tanaka, A.; Ye, J. Photothermal conversion of CO_2 into CH_4 with H_2 over Group VIII nanocatalysts: an alternative approach for solar fuel production. Angew Chem Int Ed Engl **2014**, 53 (43), 11478-11482. DOI: 10.1002/anie.201404953 From NLM.

(74) Chai, S.; Men, Y.; Wang, J.; Liu, S.; Song, Q.; An, W.; Kolb, G. Boosting CO_2 methanation activity on Ru/TiO_2 catalysts by exposing (001) facets of anatase TiO_2. Journal of CO_2 Utilization **2019**, 33, 242-252. DOI: https://doi.org/10.1016/j.jcou.2019.05.031.

(75) Zhang, J.; Liu, H.; Wang, Z.; Ming, N. Shape-Selective Synthesis of Gold Nanoparticles with Controlled Sizes, Shapes, and Plasmon Resonances. Advanced Functional Materials **2007**, 17 (16), 3295-3303. DOI: https://doi.org/10.1002/adfm.200700497.

(76) Mock, J. J.; Barbic, M.; Smith, D. R.; Schultz, D. A.; Schultz, S. Shape effects in plasmon resonance of individual colloidal silver nanoparticles. The Journal of Chemical Physics **2002**, 116 (15), 6755-6759. DOI: 10.1063/1.1462610.

(77) Douglas-Gallardo, O. A.; Berdakin, M.; Sánchez, C. G. Atomistic Insights into Chemical Interface Damping of Surface Plasmon Excitations in Silver Nanoclusters. The Journal of Physical Chemistry C **2016**, 120 (42), 24389-24399. DOI: 10.1021/acs.jpcc.6b08519.

(78) Rycenga, M.; Cobley, C. M.; Zeng, J.; Li, W.; Moran, C. H.; Zhang, Q.; Qin, D.; Xia, Y. Controlling the synthesis and assembly of silver nanostructures for plasmonic applications. Chem Rev **2011**, 111 (6), 3669-3712. DOI: 10.1021/cr100275d From NLM.

(79) Link, S.; El-Sayed, M. A. Size and Temperature Dependence of the Plasmon Absorption of Colloidal Gold Nanoparticles. The Journal of Physical Chemistry B **1999**, 103 (21), 4212-4217. DOI: 10.1021/jp984796o.

(80) Zhang, Q.; Li, W.; Moran, C.; Zeng, J.; Chen, J.; Wen, L.-P.; Xia, Y. Seed-Mediated Synthesis of Ag Nanocubes with Controllable Edge Lengths in the Range of 30−200 nm and Comparison of Their Optical Properties. Journal of the American Chemical Society **2010**, 132 (32), 11372-11378. DOI: 10.1021/ja104931h.

(81) Mateo, D.; Albero, J.; García, H. Titanium-Perovskite-Supported RuO_2 Nanoparticles for Photocatalytic CO_2 Methanation. Joule **2019**, 3 (8), 1949-1962. DOI: https://doi.org/10.1016/j.joule.2019.06.001.

(82) O'Brien, P. G.; Sandhel, A.; Wood, T. E.; Jelle, A. A.; Hoch, L. B.; Perovic, D. D.; Mims, C. A.; Ozin, G. A. Photomethanation of Gaseous CO_2 over Ru/Silicon Nanowire Catalysts with Visible and Near-Infrared Photons. Advanced Science **2014**, 1 (1), 1400001. DOI: https://doi.org/10.1002/advs.201400001.

(83) Wang, C.; Fang, S.; Xie, S.; Zheng, Y.; Hu, Y. H. Thermo-photo catalytic CO_2 hydrogenation over Ru/TiO_2. Journal of Materials Chemistry A **2020**, 8 (15), 7390-7394, 10.1039/C9TA13275A. DOI: 10.1039/C9TA13275A.

(84) Ge, H.; Kuwahara, Y.; Kusu, K.; Bian, Z.; Yamashita, H. $Ru/HxMoO_{3-y}$ with plasmonic effect for boosting photothermal catalytic CO_2 methanation. Applied Catalysis B: Environmental **2022**, 317, 121734. DOI: https://doi.org/10.1016/j.apcatb.2022.121734.

(85) L. Paulista, A. F., B. Castanheira, Đ. Maja, R. Martins, R. Boaventura, V. Vilar, T. Silva,. Thermo-photocatalytic CO_2 methanation at low temperature using RuO_2-doped TiO_2 incorporated in SBA-15. In V CIPOA - 5th Iberoamerican conference on advanced oxidation technologies, Cusco, Peru, 2022.

(86) Jin, B.; Ye, X.; Zhong, H.; Jin, F.; Hu, Y. H. Enhanced photocatalytic CO_2 hydrogenation with wide-spectrum utilization over black TiO_2 supported catalyst. Chinese Chemical Letters **2022**, 33 (2), 812-816. DOI: https://doi.org/10.1016/j.cclet.2021.07.046.

(87) Tan, H.; Zhao, Z.; Niu, M.; Mao, C.; Cao, D.; Cheng, D.; Feng, P.; Sun, Z. A facile and versatile method for preparation of colored TiO2 with enhanced solar-driven photocatalytic activity. Nanoscale **2014**, 6 (17), 10216-10223, 10.1039/C4NR02677B. DOI: 10.1039/C4NR02677B.

(88) Li, Q.; Gao, Y.; Zhang, M.; Gao, H.; Chen, J.; Jia, H. Efficient infrared-light-driven photothermal CO_2 reduction over MOF-derived defective Ni/TiO_2. Applied Catalysis B: Environmental **2022**, 303, 120905. DOI: https://doi.org/10.1016/j.apcatb.2021.120905.

(89) Monteiro, R. A. R.; Miranda, S. M.; Rodrigues-Silva, C.; Faria, J. L.; Silva, A. M. T.; Boaventura, R. A. R.; Vilar, V. J. P. Gas phase oxidation of n-decane and PCE by photocatalysis using an annular photoreactor packed with a monolithic catalytic bed coated with P25 and PC500. Applied Catalysis B: Environmental **2015**, 165, 306-315. DOI: https://doi.org/10.1016/j.apcatb.2014.10.026.

(90) Modwi, A.; Ghanem, M. A.; Al-Mayouf, A. M.; Houas, A. Lowering energy band gap and enhancing photocatalytic properties of Cu/ZnO composite decorated by transition metals. Journal of Molecular Structure **2018**, 1173, 1-6. DOI: https://doi.org/10.1016/j.molstruc.2018.06.082.

Appendix A. Mass-weighted for catalysts synthesis

Tables A.1 to A.8 display the mass-weighted for each synthesized catalyst, accompanied by their respective overall synthesis yields.

Black TiO_2 preparation:

Table A.1: Mass-weighted values for synthesising black TiO_2.

TiO_2	Mass of TiO_2 (g)	Mass of $NaBH_4$ (g)	Mass of Black TiO_2 produced (g)	Yield (%)
P25	1.0039	0.3774	1.1766	85.18
PC500	1.0023	0.3818	Did not produce black TiO_2	---

Incipient wetness impregnation:

Table A.2: Mass-weighted values for synthesising Ru/TiO_2 catalysts using incipient wetness impregnation.

Theoretical mass ratio (wt%)	Used TiO_2	Mass of TiO_2 (g)	Mass of $RuCl_3$ (g)	Mass of produced Ru/TiO_2 (g)	Yield (%)
10	Anatase	0.5008	0.1139	0.5219	84.90
7.5	Anatase	0.4997	0.0833	0.5129	87.98
5	Anatase	0.5003	0.0542	0.5068	91.40
10	PC500	0.5023	0.1137	0.4764	77.34

Table A.3: Mass-weighted values for synthesising Ni/TiO_2 catalysts using incipient wetness impregnation.

Theoretical mass ratio (wt%)	Used TiO_2	Mass of TiO_2 (g)	Mass of $Ni(NO_3)_2$ (g)	Mass of produced Ni/TiO_2 (g)	Yield (%)
10	Anatase	0.5005	0.2745	0.5438	70.17
7.5	Anatase	0.5000	0.2015	0.5301	75.57
5	Anatase	0.5005	0.1296	0.4956	78.65
10	PC500	0.5003	0.2778	0.4597	59.08
10	Black TiO_2	0.3911	0.2155	0.3896	64.23

Reflux impregnation:

Table A.4: Mass-weighted values for synthesising Ru/TiO_2 catalysts using the reflux method.

Theoretical mass ratio (wt%)	Mass of TiO_2 (g)	Mass of $RuCl_3$ (g)	Mass of produced Ru/TiO_2 (g)	Yield (%)
10	0.4999	0.1129	0.4764	77.74

Table A.5. Mass-weighted values for synthesising Ni/TiO_2 catalysts using the reflux method.

Theoretical mass ratio (wt%)	Mass of TiO_2 (g)	Mass of $Ni(NO_3)_2$ (g)	Mass of produced Ni/TiO_2 (g)	Yield (%)
10	0.5021	0.2756	0.6452	82.96

Wet impregnation:

Table A.6: Mass-weighted values for synthesising Ni/TiO_2 catalysts using the wet impregnation method.

Theoretical mass ratio (wt%)	Intermediate mixing step	Mass of TiO_2 (g)	Mass of $Ni(NO_3)_2$ (g)	Mass of produced Ni/TiO_2 (g)	Yield (%)
10	Yes	0.5041	0.2616	0.3592	62.45
10	No	0.5024	0.2780	0.3235	58.43

Solvothermal synthesis:

Table A.7: Mass-weighted values for synthesising Ru/TiO_2 catalysts using solvothermal synthesis.

Theoretical mass ratio (wt%)	Mass of TiO_2 (g)	Mass of $RuCl_3$ (g)	Mass of produced Ru/TiO_2 (g)	Yield (%)
5	0.5082	0.054	0.3768	67.02
7.5	0.5079	0.0819	0.39996	67.81
10	0.5005	0.116	0.436	70.72
20	0.5006	0.2483	0.4115	54.95

Table A.8: Mass-weighted values for synthesising Ni/TiO_2 catalysts using solvothermal synthesis.

Theoretical mass ratio (wt%)	Mass of TiO_2 (g)	Mass of $Ni(NO_3)_2$ (g)	Mass of produced Ni/TiO_2 (g)	Yield (%)
10	0.5008	0.277	0.5601	72.08

Appendix B. Performed experiments, conditions and respective results

Table B.1: Experimental conditions and obtained results for all the CO_2 hydrogenation reaction tests.

Experiment	Plasmonic Material	Mass fraction (wt%)	TiO_2	Preparation method	Irradiance ($W \cdot m^{-2}$)	IR filter	External heating	Average Temperature(ºC)	Reaction time (min)	Mass of catalyst (g)	CO_2 Conversion (%)	CH_4 Selectivity (%)
1	Ni	5	Anatase	Incipient Impregnation	500	✓	✓	130	120	103.4	1.42	100
2	Ni	7.5	Anatase	Incipient Impregnation	500	✓	✓	130	120	108.7	1.40	100
3	Ni	10	Anatase	Incipient Impregnation	500	✓	✓	130	120	112.5	2.48	100
4	Ru	5	Anatase	Incipient Impregnation	500	✓	✓	130	120	112.4	0.00	N.A.
5	Ru	7.5	Anatase	Incipient Impregnation	500	✓	✓	130	120	107.2	0.00	N.A.
6	Ru	10	Anatase	Incipient Impregnation	500	✓	✓	130	120	106.4	0.09	100
7	Ni	10	Black P25	Incipient Impregnation	500	✓	✓	130	120	103.0	0.45	100
8	Ni	10	PC500	Incipient Impregnation	500	✓	✓	130	120	96.4	2.13	100
9	Ru	10	PC500	Incipient Impregnation	500	✓	✓	130	120	102.0	1.22	100
10	Ni	10	PC500	Wet Impregnation (no mixing)	500	✓	✓	130	120	105.2	0.18	100
11	Ni	10	PC500	Wet Impregnation (mixing)	500	✓	✓	130	120	108.7	0.13	100
12	Ni	10	PC500	Reflux	500	✓	✓	130	120	100.6	1.98	100
13	Ru	10	PC500	Reflux	500	✓	✓	130	120	102.1	18.27	100
14	Ni	10	PC500	Solvothermal	500	✓	✓	130	120	101.1	1.39	100
15	Ru	10	PC500	Solvothermal	500	✓	✓	130	60	99.8	46.95	100
16	Ru	5	PC500	Solvothermal	500	✓	✓	130	60	99.4	13.49	100
17	Ru	7.5	PC500	Solvothermal	500	✓	✓	130	60	102.3	46.14	100
18	Ru	12.5	PC500	Solvothermal	500	✓	✓	130	60	99.7	45.88	100

Experiment	Plasmonic Material	Mass fraction (wt%)	TiO_2	Preparation method	Irradiance ($W \cdot m^{-2}$)	IR filter	External heating	Average Temperature(°C)	Reaction time (min)	Mass of catalyst (g)	CO_2 Conversion (%)	CH_4 Selectivity (%)
19	Ru	20	PC500	Solvothermal	500	✓	✓	130	60	96.5	39.21	100
20	Ru	10	PC500	Solvothermal	500	✓	✓	130	60	99.8	43.99	100
21	Ru	10	PC500	Solvothermal	500	✓	✓	130	60	99.6	45.39	100
22	Ru	12.5	PC500	Solvothermal	500	✓	✓	130	60	102.4	42.21	100
23	Ru	7.5	PC500	Solvothermal	500	✓	✓	130	60	101.0	44.90	100
24	Ru	7.5	PC500	Solvothermal	500	×	✓	130	60	101.1	49.56	100
25	Ru	7.5	PC500	Solvothermal	500	×	×	52.5	60	99.9	0.12	100
26	Ru	7.5	PC500	Solvothermal	0	×	✓	130	60	101.7	25.09	100
27	Ru	7.5	PC500	Solvothermal	500	×	✓	100	60	99.1	16.11	100
28	Ru	7.5	PC500	Solvothermal	0	N.A.	✓	100	60	100.2	7.14	100
29	Ru	7.5	PC500	Solvothermal	500	×	✓	160	15	101.0	72.88	100
30	Ru	7.5	PC500	Solvothermal	0	×	✓	160	15	101.0	46.81	100
31	Ru	7.5	PC500	Solvothermal	0	×	✓	160	5	100.9	10.90	100
32	Ru	7.5	PC500	Solvothermal	500	×	✓	160	3	100.9	40.19	100
33	Ru	7.5	PC500	Solvothermal	500	×	✓	160	6	100.9	57.93	100
34	Ru	7.5	PC500	Solvothermal	500	×	✓	160	9	100.9	67.70	100
35	Ru	7.5	PC500	Solvothermal	500	×	✓	160	12	100.9	73.86	100
36	Ru	7.5	PC500	Solvothermal	500	×	✓	160	15	100.9	78.90	100

Appendix C. N_2 adsorption-desorption isotherms

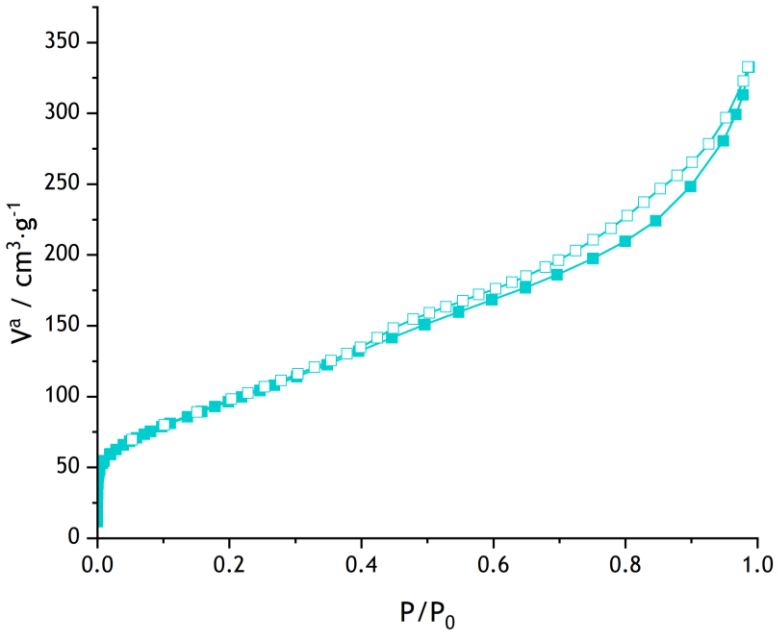

Figure C.1: N_2 adsorption-desorption isotherm for PC500 TiO_2. S_{BET} = 316.2 $m^2 \cdot g^{-1}$.

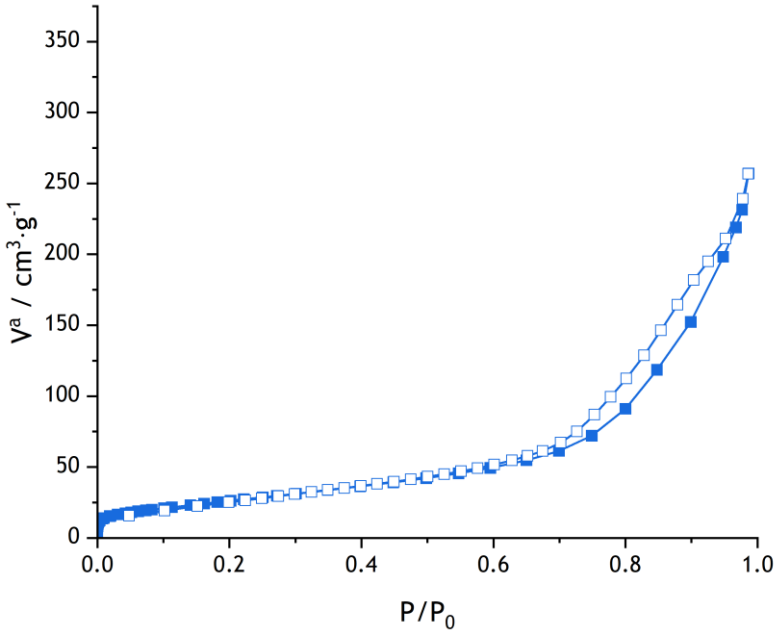

Figure C.2: N_2 adsorption-desorption isotherm for the 10 wt% Ru/TiO_2-PC500 prepared via reflux impregnation. S_{BET} = 84.3 $m^2 \cdot g^{-1}$.

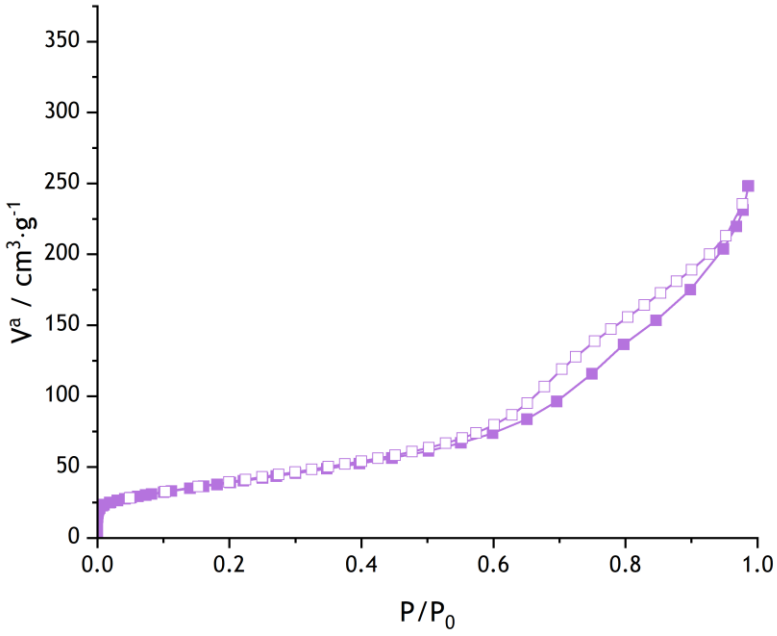

Figure C.3: N_2 adsorption-desorption isotherm for the 10 wt% Ru/TiO_2-PC500 prepared via solvothermal impregnation. S_{BET} = 129.1 $m^2 \cdot g^{-1}$.

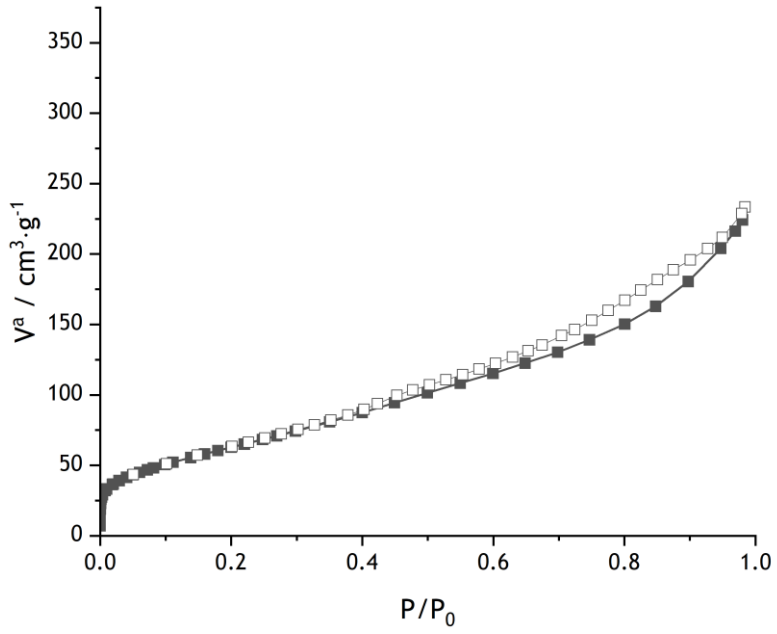

Figure C.4: N_2 adsorption-desorption isotherm for the 10 wt% Ru/TiO_2-PC500 prepared via incipient wetness impregnation. S_{BET} = 205.5 $m^2 \cdot g^{-1}$.

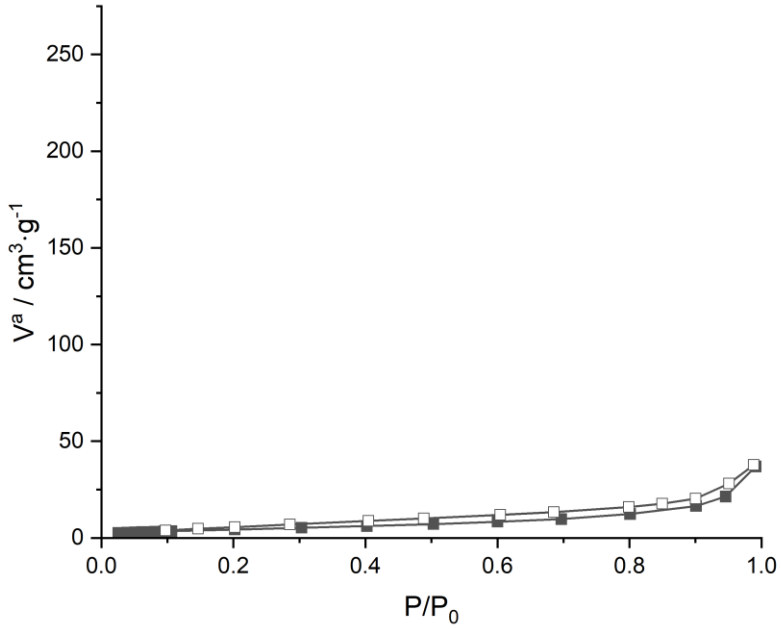

Figure C.5: N_2 adsorption-desorption isotherm for the 10 wt% Ru/TiO_2-Anat prepared via incipient wetness impregnation. S_{BET} = 15.3 $m^2 \cdot g^{-1}$.

Appendix D. H_2-TPR graphic representation

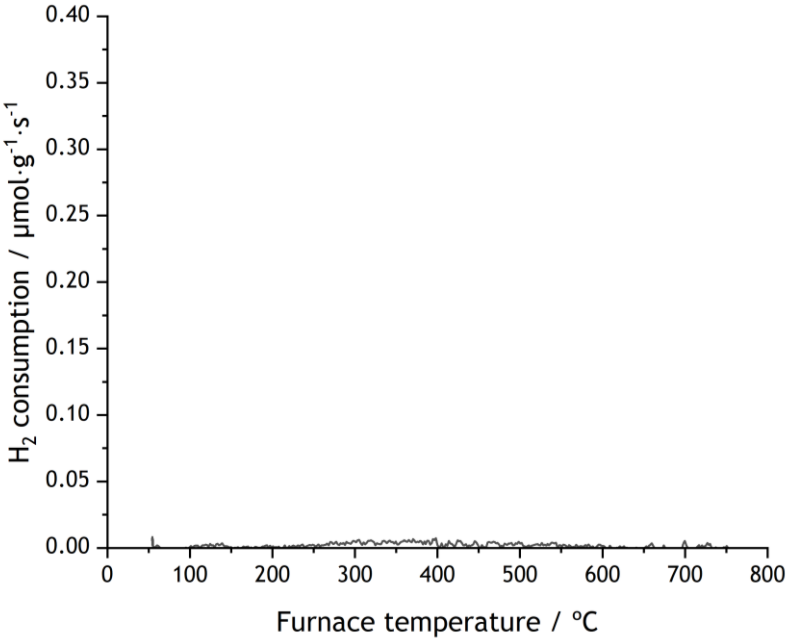

Figure D.1: H_2-TPR for the 10 wt% Ru/TiO_2-Anat prepared via incipient wetness impregnation. Consumed H_2 = 7.9 µmol·g^{-1}.

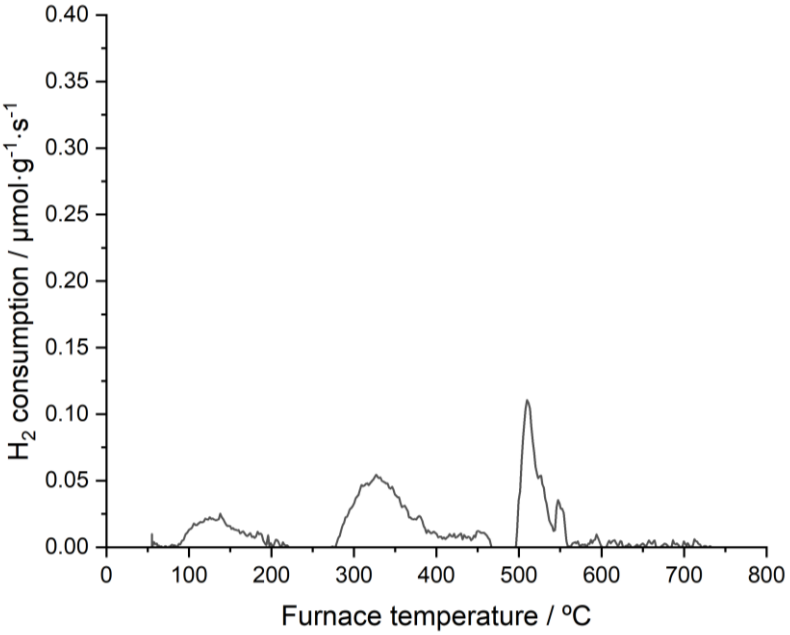

Figure D.2: H_2-TPR for the 10 wt% Ru/TiO_2-PC500 prepared via incipient wetness impregnation. Consumed H_2 = 56.0 µmol·g^{-1}.

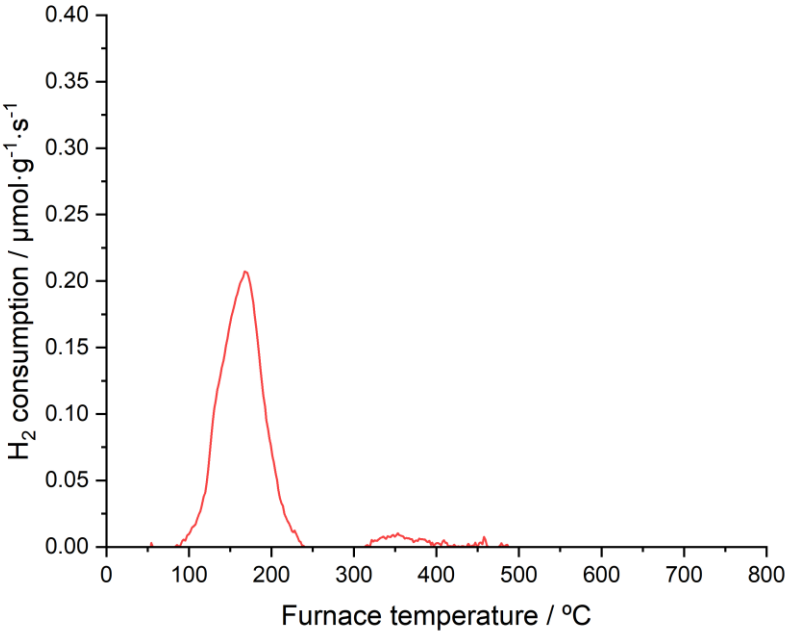

Figure D.3: H_2-TPR for the 10 wt% Ru/TiO_2-PC500 prepared via reflux impregnation. Consumed H_2 = 82.7 µmol·g^{-1}.

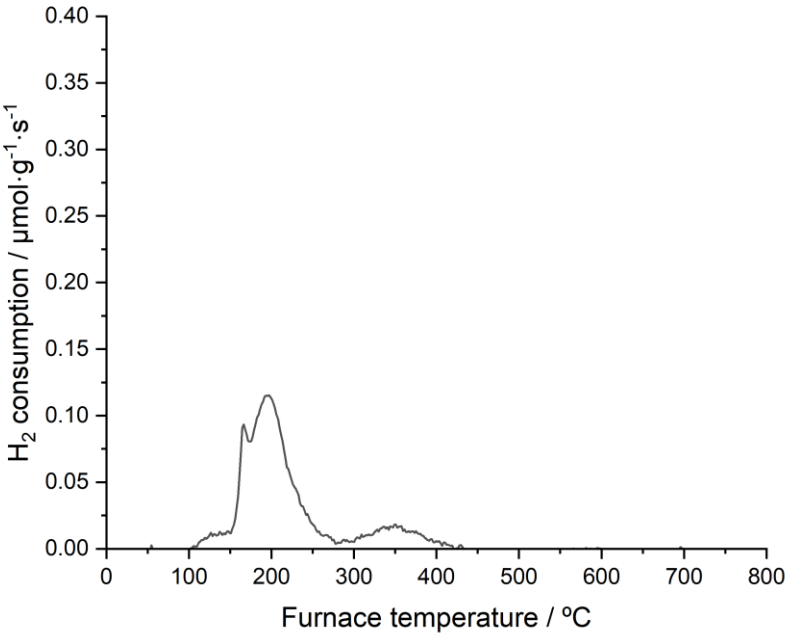

Figure D.4: H_2-TPR for the 5 wt% Ru/TiO_2-PC500 prepared via solvothermal impregnation. Consumed H_2 = 54.0 µmol·g^{-1}.

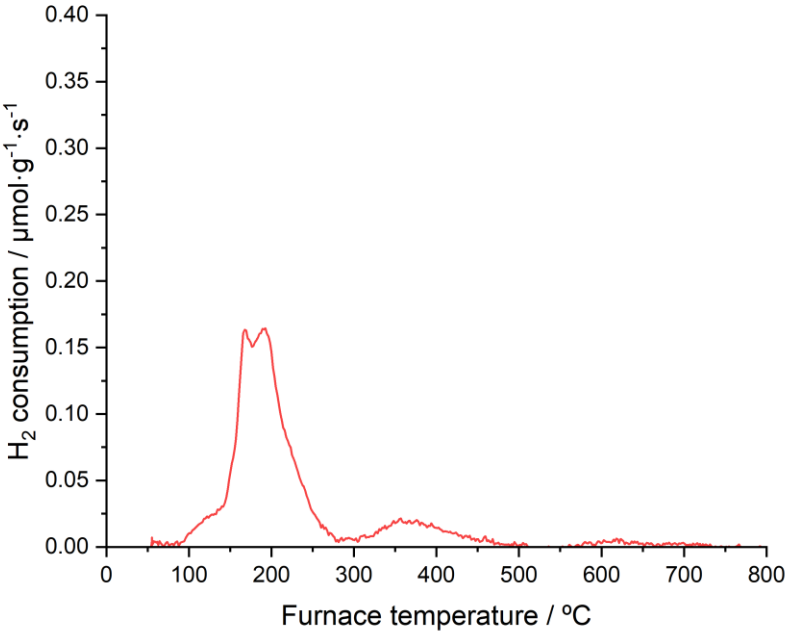

Figure D.5: H_2-TPR for the 7.5 wt% Ru/TiO_2-PC500 prepared via solvothermal impregnation. Consumed H_2 = 90.4 µmol·g^{-1}.

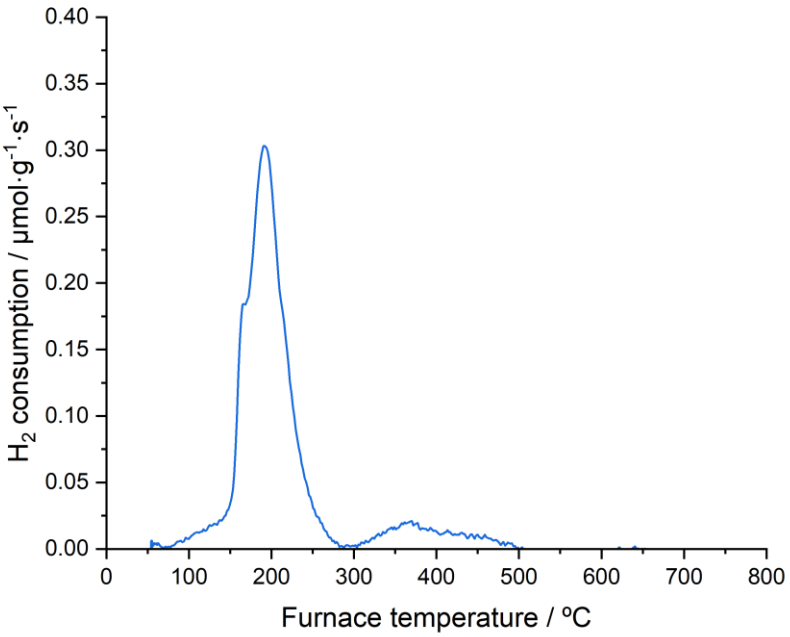

Figure D.6: H_2-TPR for the 10 wt% Ru/TiO_2-PC500 prepared via solvothermal impregnation. Consumed H_2 = 121.3 µmol·g^{-1}.

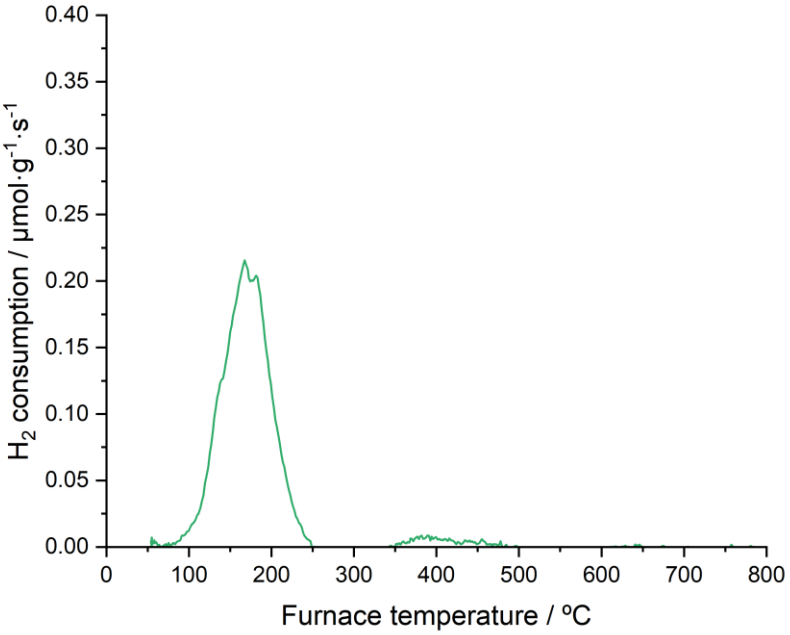

Figure D.7: H_2-TPR for the 12.5 wt% Ru/TiO_2-PC500 prepared via solvothermal impregnation. Consumed H_2 = 95.2 µmol·g^{-1}.

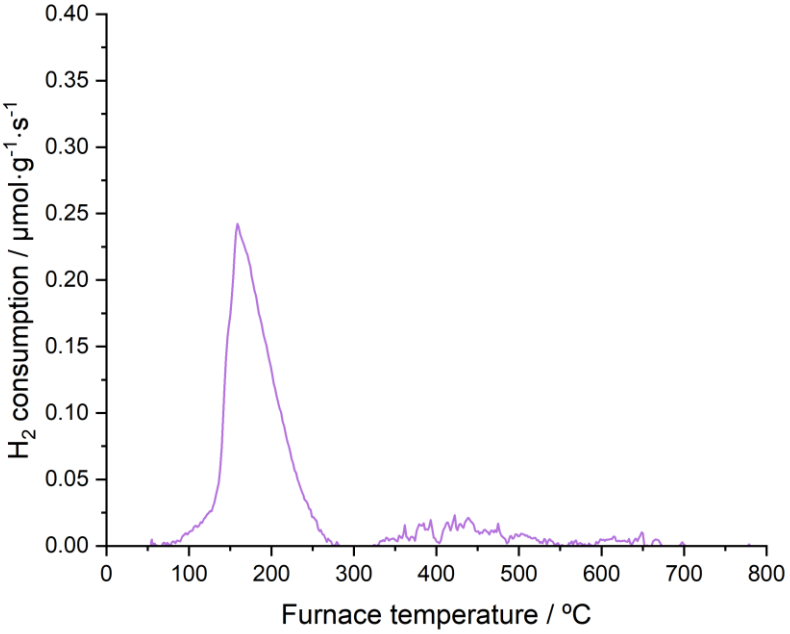

Figure D.8: H_2-TPR for the 20 wt% Ru/TiO_2-PC500 prepared via solvothermal impregnation. Consumed H_2 = 109.8 µmol·g^{-1}.

Appendix E. UV-Vis and Tauc plots

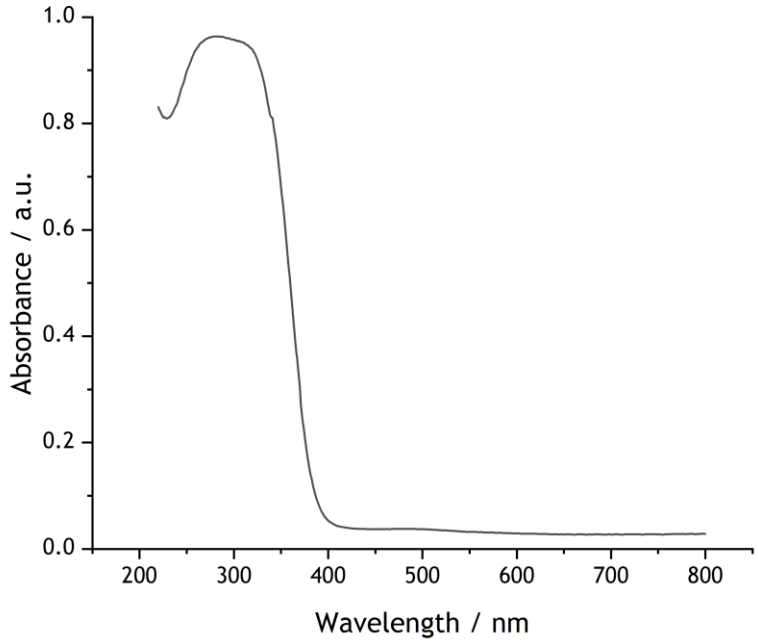

Figure E.1: UV-Vis spectroscopy plot for PC500 TiO_2.

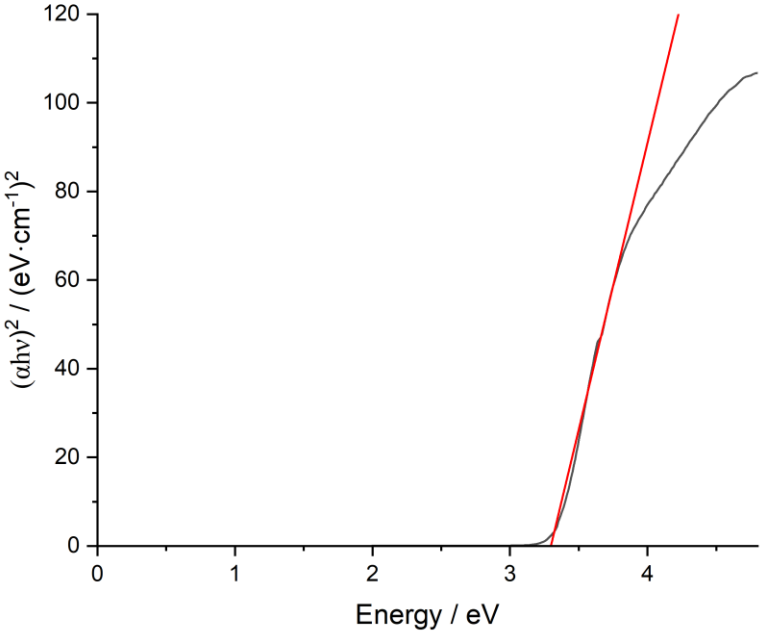

Figure E.2: Tauc plot for PC500 TiO_2. E_g = 3.29 eV.

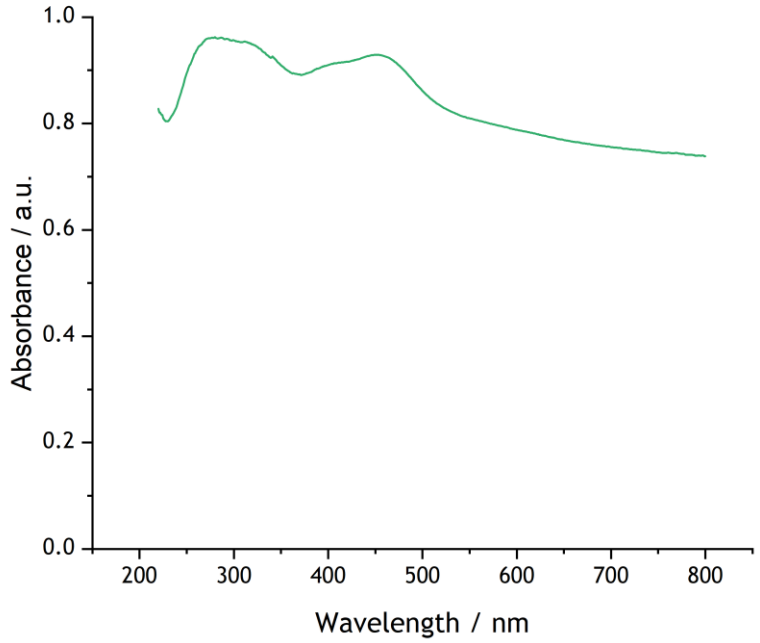

Figure E.3: UV-Vis spectroscopy plot for the 10 wt% Ru/TiO_2-PC500 prepared via incipient wetness impregnation.

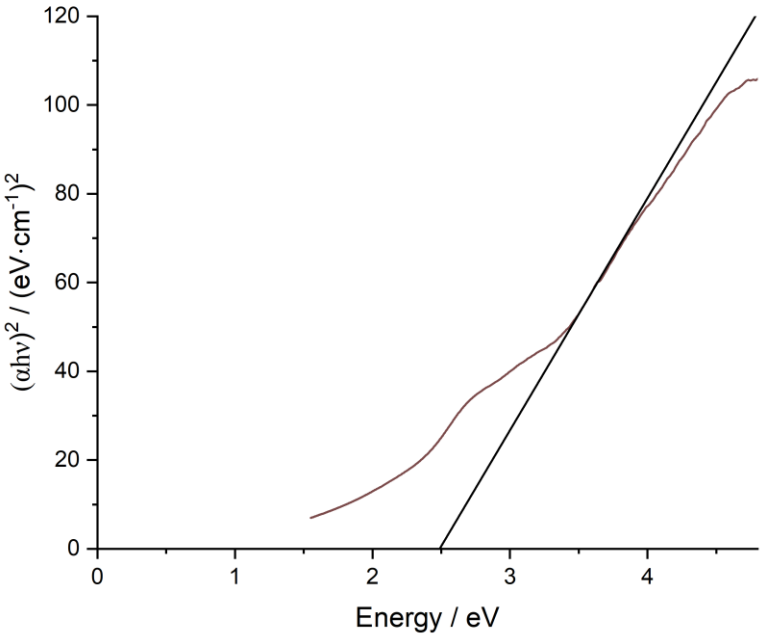

Figure E.4: Tauc plot for 10 wt% Ru/TiO_2-PC500 prepared via incipient wetness impregnation. E_g = 2.43 eV.

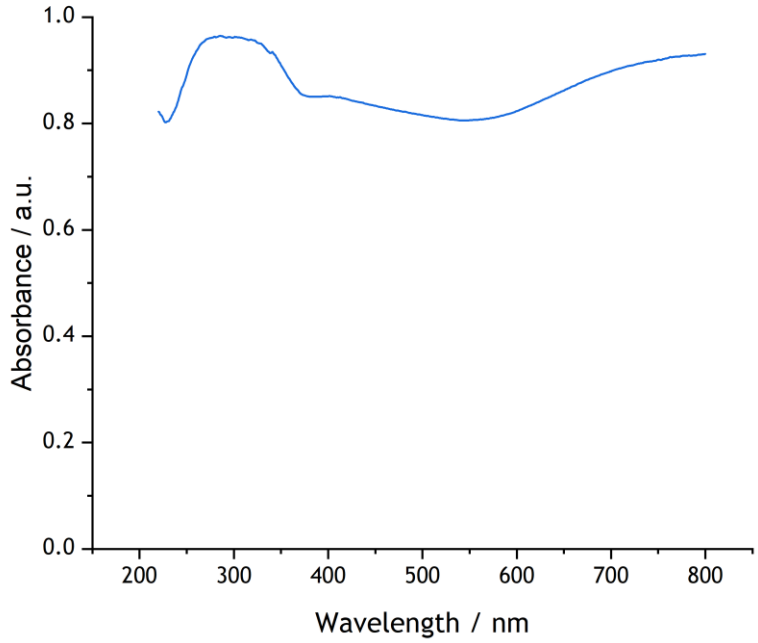

Figure E.5: UV-Vis spectroscopy plot for the 10 wt% Ru/TiO_2-PC500 prepared via reflux impregnation.

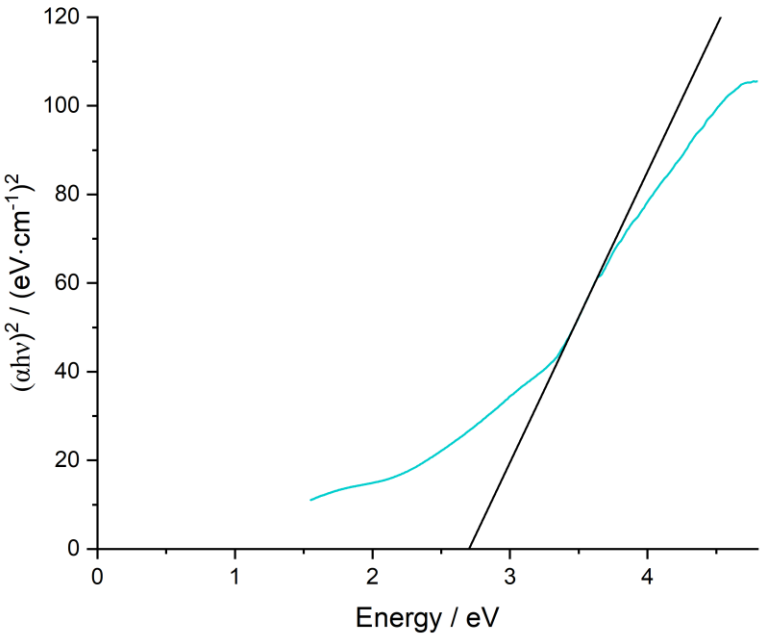

Figure E.6: Tauc plot for 10 wt% Ru/TiO_2 prepared via reflux impregnation with PC500 TiO_2. E_g = 2.66 eV.

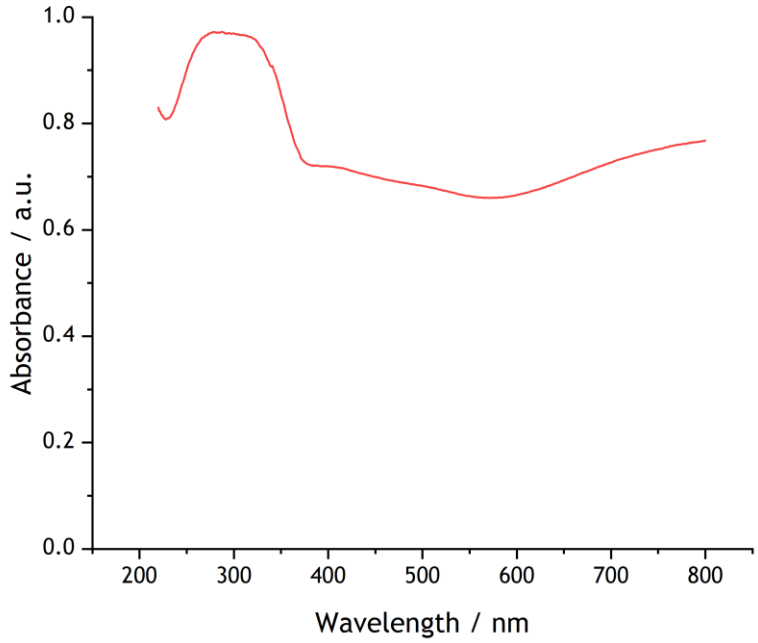

Figure E.7: UV-Vis spectroscopy plot for the 5 wt% Ru/TiO_2-PC500 prepared via solvothermal impregnation.

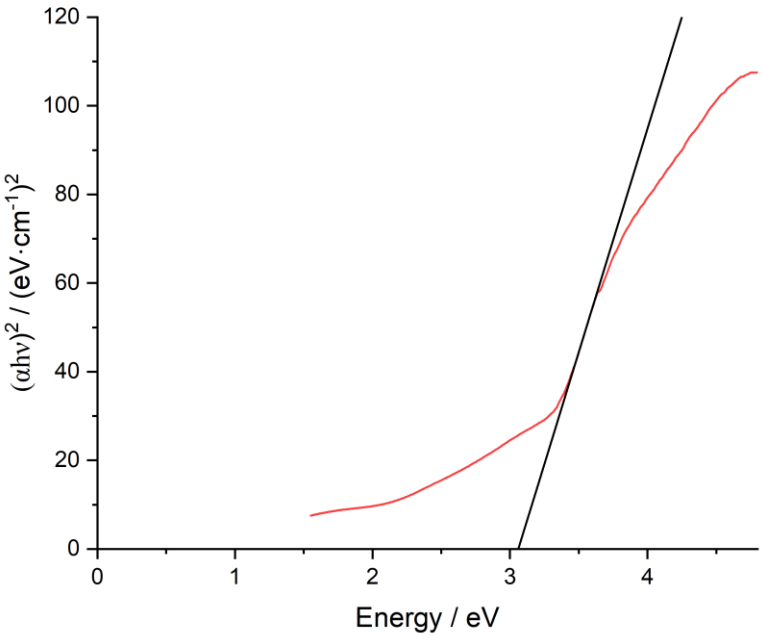

Figure E.8: Tauc plot for 5 wt% Ru/TiO_2-PC500 prepared via solvothermal impregnation. E_g = 3.12 eV.

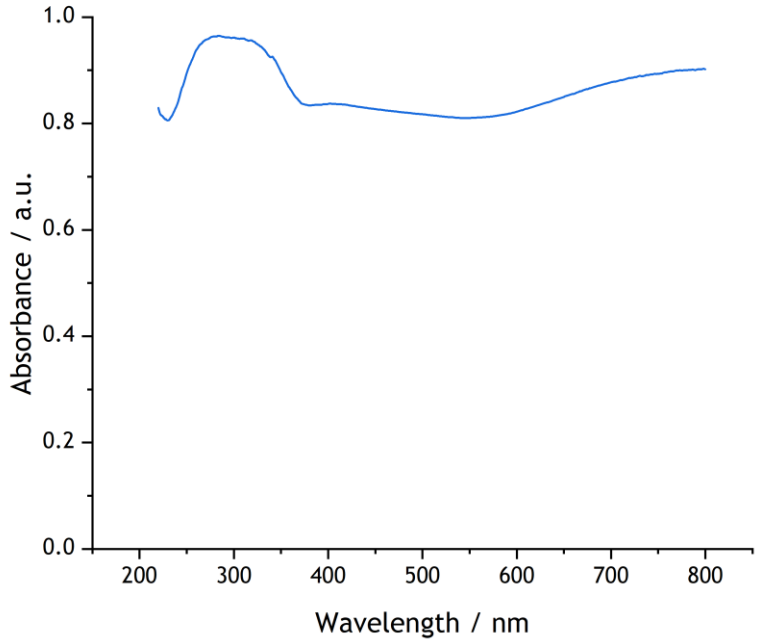

Figure E.9: UV-Vis spectroscopy plot for the 7.5 wt% Ru/TiO_2-PC500 prepared via solvothermal impregnation.

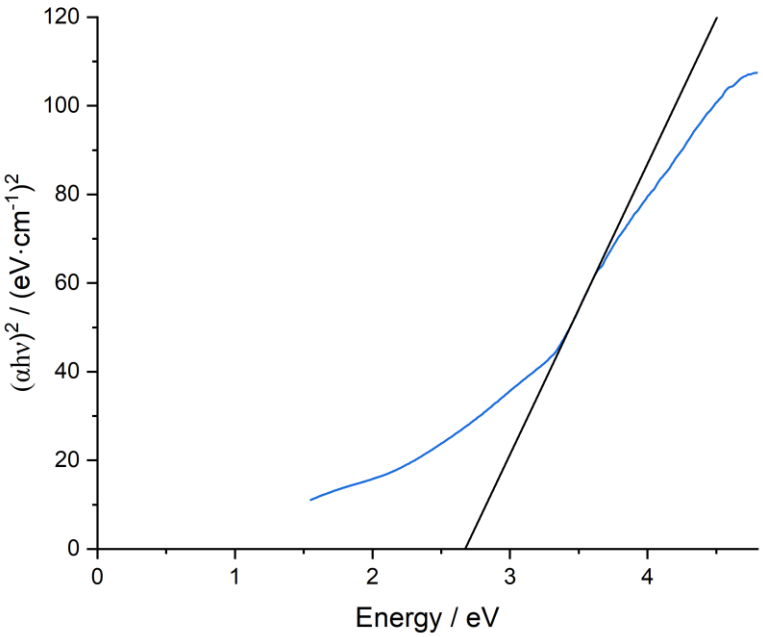

Figure E.10: Tauc plot for 7.5 wt% Ru/TiO_2-PC500 prepared via solvothermal impregnation. E_g = 2.64 eV.

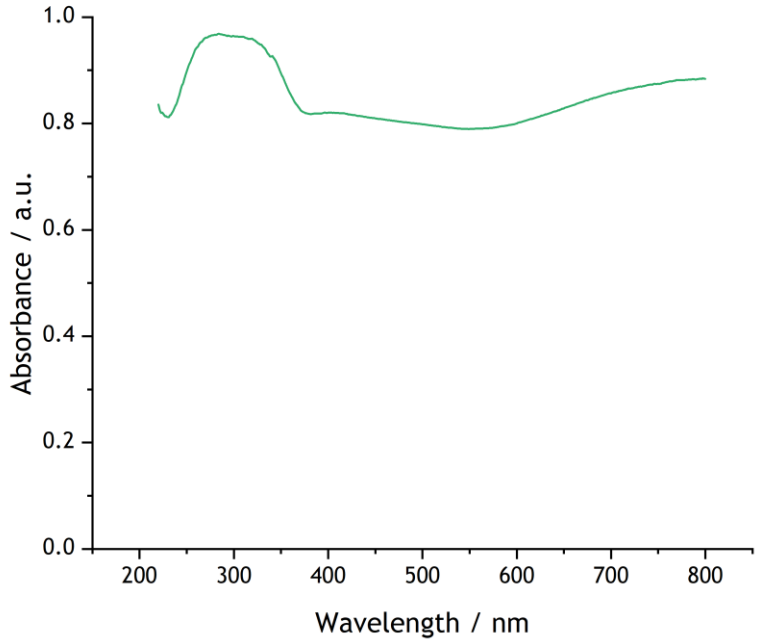

Figure E.11: UV-Vis spectroscopy plot for the 10 wt% Ru/TiO_2-PC500 prepared via solvothermal impregnation.

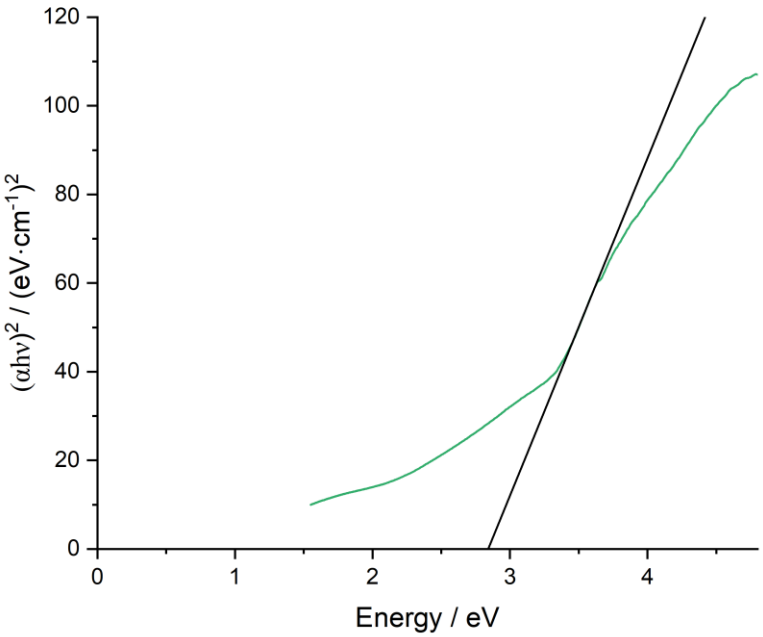

Figure E.12: Tauc plot for 10 wt% Ru/TiO_2-PC500 prepared via solvothermal impregnation. E_g = 2.82 eV.

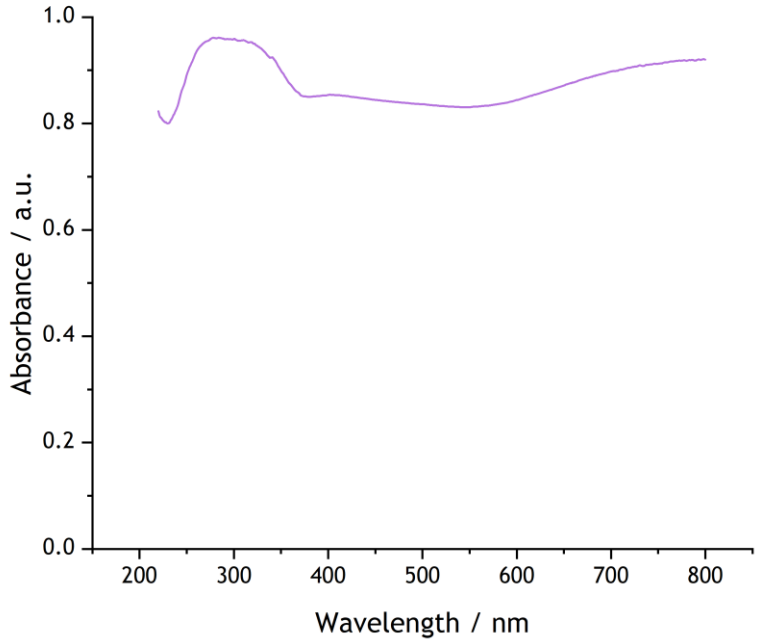

Figure E.13: UV-Vis spectroscopy plot for the 12.5 wt% Ru/TiO_2-PC500 prepared via solvothermal impregnation.

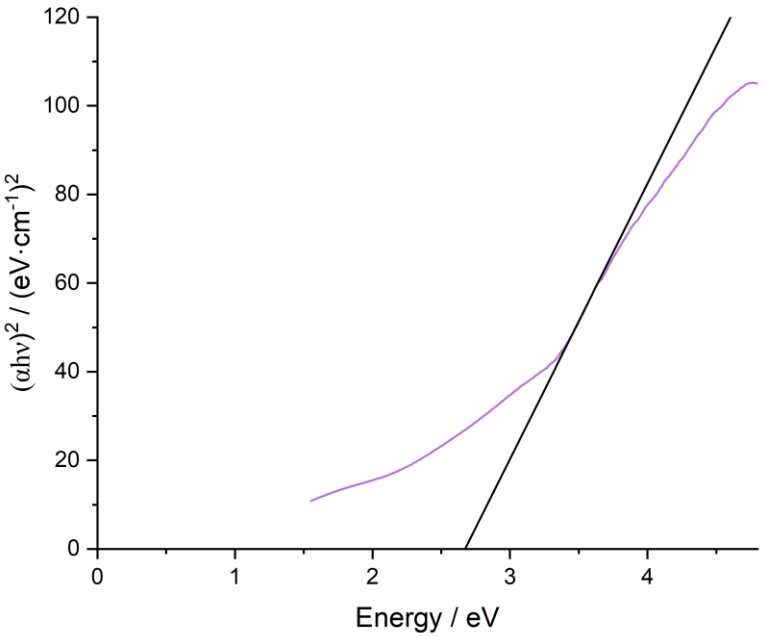

Figure E.14: Tauc plot for 12.5 wt% Ru/TiO_2-PC500 prepared via solvothermal impregnation. E_g = 2.65 eV.

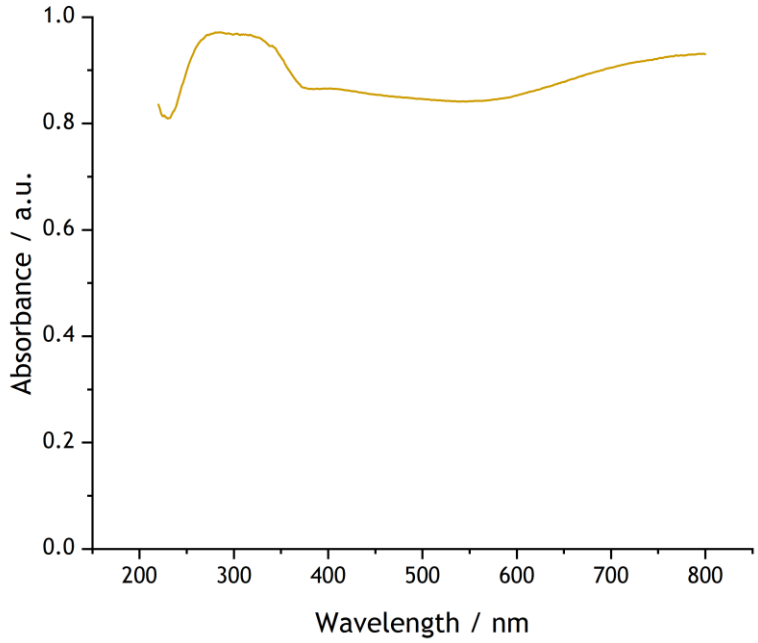

Figure E.15: UV-Vis spectroscopy plot for the 20 wt% Ru/TiO_2-PC500 prepared via solvothermal impregnation.

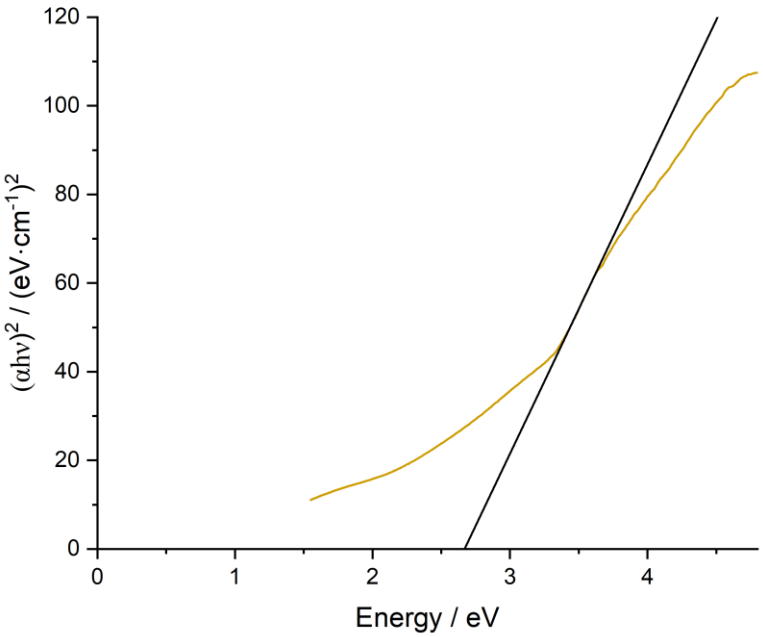

Figure E.16: Tauc plot for 20 wt% Ru/TiO_2-PC500 prepared via solvothermal impregnation. E_g = 2.67 eV.